Cranfield UNIVERSITY

College of Defence Technology
Department of Aerospace, Power & Sensors

PhD Thesis
2005

Robin David Knowles

Monoposto Racecar Wheel Aerodynamics: Investigation of Near-Wake Structure & Support-Sting Interference

---

Supervisors: Dr. K. Knowles
Dr. A. J. Saddington

Presented on 17th February 2005

Abstract

Monoposto racecar development is routinely carried out using wheels supported not by the car suspension but by individual, externally-mounted stings. The interference effect of these stings was acknowledged but unquantified in the existing literature. Appraisal of the literature has found that the structure of a wheel wake was not understood, rendering it difficult to assess the support sting interference. These two issues were thus jointly addressed using experimental and computational methods.

The two phases of this project each tested a different industrially-representative racecar wheel model. Phase One investigated a single wheel and sting combination, whilst Phase Two extended the work to include two further stings and a model racecar. Non-intrusive velocity measurements were made in the near wakes of the various combinations to extract vertical planes, perpendicular to the tunnel freestream.

The measurements made behind the isolated wheels were used to investigate the main flow features of the wake. The flow surrounding an unsupported wheel was established computationally and used to evaluate the interference effects of the support sting. Different wheel support methods (three stings and the car suspension) were used to provide further insight into the sting interference effects and also the impact of sting design on those effects. Testing with and without the model racecar allowed evaluation of its effect on the wheel wake and sting interference.

The main characteristics of the near-wake of an isolated wheel rotating in ground contact are proposed from analysis of the data generated in this study. A simplified model of the trailing-vortex system induced in the wake of such a wheel is proposed to clarify contradictory literature.

The specific interference effects of a wheel support sting are proposed with reference to the main characteristics of the wake. The mechanisms behind these effects are, where possible, identified and presented. The main impact of the support sting, and thus the root of several of the observed effects, is the modification of the axial flow through the wheel.

The main effects of the presence of the car on the near-wake are proposed alongside the observation that the wake structure is not fundamentally different to that of an isolated wheel. The proposed sting interference effects are also observed in the presence of the car, albeit at a reduced level.

Acknowledgements

To those who know they helped with this research

Thank You - I couldn’t have done it without you

To those who aren’t sure if they helped

Thank You - You did

To those who didn’t help

Maybe next time?

Contents

Notation

θ	Circumferential Wheel Angle in degrees (See Fig. 2.1 on page 10)
A	Wheel Frontal Area (as projected onto Y–Z plane)
C_D	Wheel Drag Coefficient (based on A)
C_L	Wheel Lift Coefficient (based on A)
C_p	Pressure Coefficient
D	Wheel Diameter
∇p	Jacobian of two-dimensional velocity field at point p
q	Negative trace of ∇p
r	Determinant of ∇p
Re	Reynolds Number (based on D)
Ti_u	Component of Tubulence Intensity aligned with X-Axis
u	Component of Velocity aligned with X-Axis
v	Component of Velocity aligned with Y-Axis
w	Component of Velocity aligned with Z-Axis
X	Horizontal Axis aligned with Wind Tunnel Freestream (See App. A)
Y	Transverse Horizontal Axis (See App. A)
Z	Vertical Axis (See App. A)
CFD	Computational Fluid Dynamics
F1	Formula One
HWA	Hot Wire Anemometer / Anemometry
LDA	Laser Doppler Anemometer / Anemometry
LIC	Line Integral Convolution

PIV	Particle Image Velocimetry
SAE	Society of Automotive Engineers
RMCS	Royal Military College of Science, Shrivenham

1 Introduction

Aerodynamics is one of the areas in which automotive science has most advanced over recent years. A multitude of development goals have arisen to accompany the primary aim of improved fuel efficiency through drag reduction. Newer goals include lift control and cross-wind response to improve high-speed stability and flow control to reduce spray and soiling in adverse weather conditions.

Nowhere are the goals clearer than in the world of motorsport where maximising lift-to-drag ratio is of primary concern. The multi-million dollar aerodynamic development budgets in the upper-echelons of the sport reflect the huge performance increases that can be realised through aerodynamic optimisation. As time pressures are high in all industrial aerodynamic development, there exists an opportunity for parallel academic research into the more fundamental aspects of automotive aerodynamics.

This chapter will introduce the current state of aerodynamic development within the motorsport industry and highlight, with particular reference to road wheels, two issues present in current testing methods. Such issues cannot be cost-effectively addressed by the industry and as such have formed the basis of this parallel academic–industrial research. Chapter 2 will summarise the published research into the aerodynamics of road wheels and establish the current level of knowledge in this area. From this, the aims and objectives of this study will be presented in the context of extending the available knowledge base to address the issue of support sting interference and clarify the structure of the wheel wake.

1.1 Motorsport Aerodynamic Development

As the demand for wind-tunnel time, and the scale and complexity of testing has increased, the motorsport industry has been forced to move from the rental of aerospace wind-tunnels to the construction of multi-million dollar facilities which better serve the needs of automotive aerodynamics. Chief among these needs is the suppression or removal of the boundary layer from the wind tunnel floor in the vicinity of the model. This is accomplished in many motorsport wind tunnels by a combination of mass-transfer and a continuous-belt rolling road, spanning the tunnel working section. The boundary layer is scooped or sucked away before the model and the remaining freestream flow is directed onto the road which, as it is moving at the freestream speed, does not cause a new ground boundary layer to develop. Whilst other methods are equally effective at boundary layer control, the rolling-road has the added bonus of being able to provide wheel rotation, another of the needs of automotive aerodynamics.

The model is commonly suspended above the ground using an overhead support strut as the rolling road precludes supporting the model from below. The aerodynamic forces acting on the model are measured using a balance contained either within the car or the support. The models are generally also instrumented to record the pressure distribution in key areas such as the wings, floor and radiators. Many of the model components are powered, allowing the configuration of the car to be changed without stopping the tunnel. Such changes include ride height, chassis rake and front-wing flap angle. Other detailed components to be found on many racecar models include ventilated brake discs, blown exhausts and engine-air induction.

Constant improvements in aerodynamic performance are often attributable to slight improvements in a multitude of components rather than a massive change in a few. As the testing methods strive to resolve smaller and smaller differences the fidelity of those methods becomes of paramount importance. The following sections outline two such issues that have arisen regarding wheel simulation methods.

The exposed wheels of monoposto (single-seat) racecars, such as Formula One cars, are tightly regulated to ensure that the formulae retain their distinctive appearance. Figure 1.1 illustrates the force contributions of the major components of a modern Formula One car. It clearly shows that, at around 10 % of the total vehicle drag each, the exposed wheels have a considerable impact on the overall aerodynamic performance of the car. Whilst maintaining the appearance of the car the regulations also effectively remove the opportunity to reduce this value significantly.

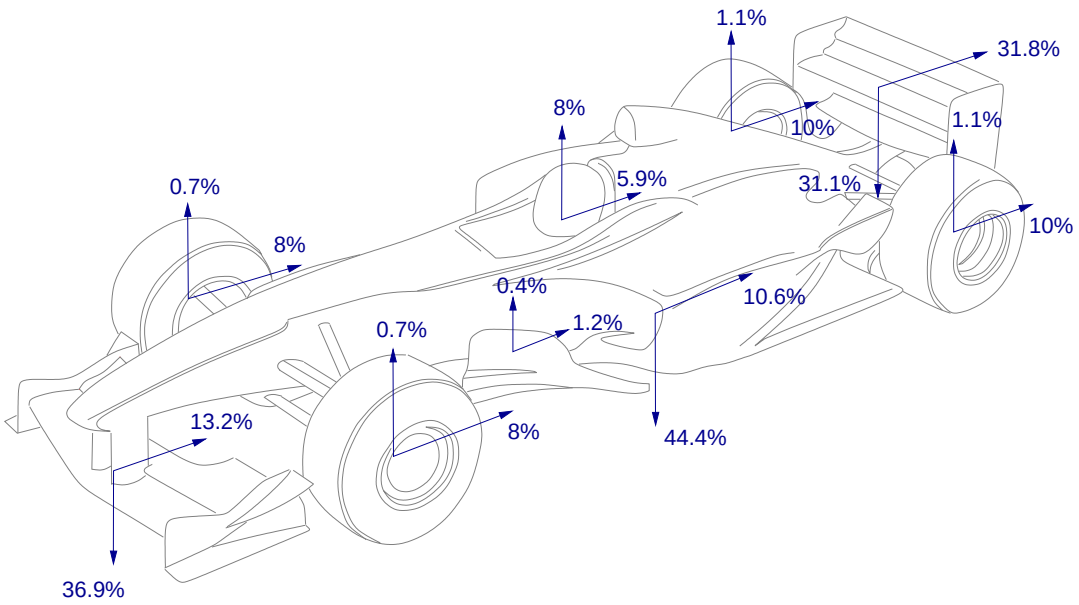

Figure 1.1: Aerodynamic Force Breakdown of a Formula One Car – after Wright [1]

1.2 Non-Deformable Wheels

The majority of wind tunnel rolling roads do not allow the testing of a pneumatic tyre deformed by the application of a vertical load. The contact force required to deform the tyre results in excessive belt wear, whilst failure of either tyre or belt would result in significant tunnel and model damage. Deformable tyres are unlikely to prevail until steel belt, or multi-belt rolling road systems become more prevalent. Non-deformable tyres are, therefore, essential but whilst solving the problem of excessive belt and tyre wear, they present other more subtle issues.

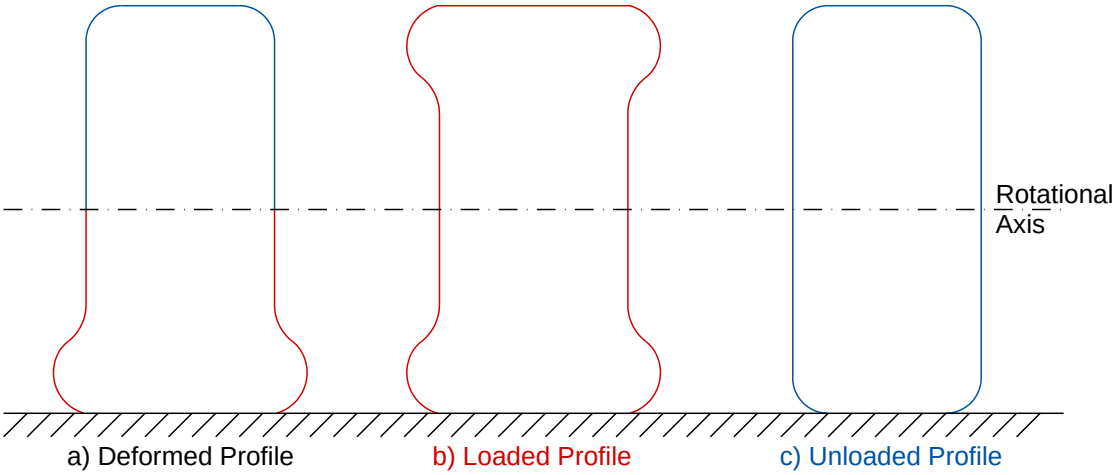

Figure 1.2: Non-Deformable Tyre Profiles

The profile of a loaded pneumatic tyre is deformed only below its rotational axis, illustrated, albeit exaggerated for clarity, in Figure 1.2(a). Once loaded the tyre is no longer rotationally symmetrical, a prerequisite for a non-deformable tyre. Either the upper or lower cross-section revolved about the rotational axis to generate the profile for a non-deformable tyre will be inaccurate over some of its circumference, as shown in Figures 1.2(b) and (c). It is therefore necessary to accept one of the latter two profiles or attempt to blend them into a third hybrid profile as is often used in racecar testing. The use of a non-deformable wheel with an approximate tyre profile and a reduced contact patch is clearly not an ideal representation of the real situation but is unavoidable with current testing techniques.

The wake structure of a wheel is not sufficiently understood to determine whether the use of non-deformable tyres is an acceptable compromise or whether the cost of a steel or multi-belt rolling road is justified.

1.3 “Wheels-Off” Testing

A test configuration was described earlier in which the model car is suspended from an overhead support sting, above a rolling road on which the wheels rest and rotate. If the model or support strut contained a force balance then it would measure both the aerodynamic forces of interest

and the forces due to the wheels rotating in ground contact. Figure 1.1 has already shown that the aerodynamic forces acting on the wheels are considerable, and effectively fixed because of regulation. As such it would be desirable to isolate these from the main forces of interest, those acting on the car.

One of the most common ways of overcoming this issue is to test the model in what is known as a “wheels-off” configuration. Here the wheels are not supported by the suspension of the model car, but by individual, externally-mounted stings. This arrangement mechanically decouples the car body from the ground whilst still allowing the wheels to be rotated by direct contact with the rolling-road belt. Measurements of the aerodynamic forces exerted on the car model no longer require correction to account for this mechanical contact. Figure 1.3, shows a Champ Car in “wheels-off” configuration with the four wheel support stings clearly visible.

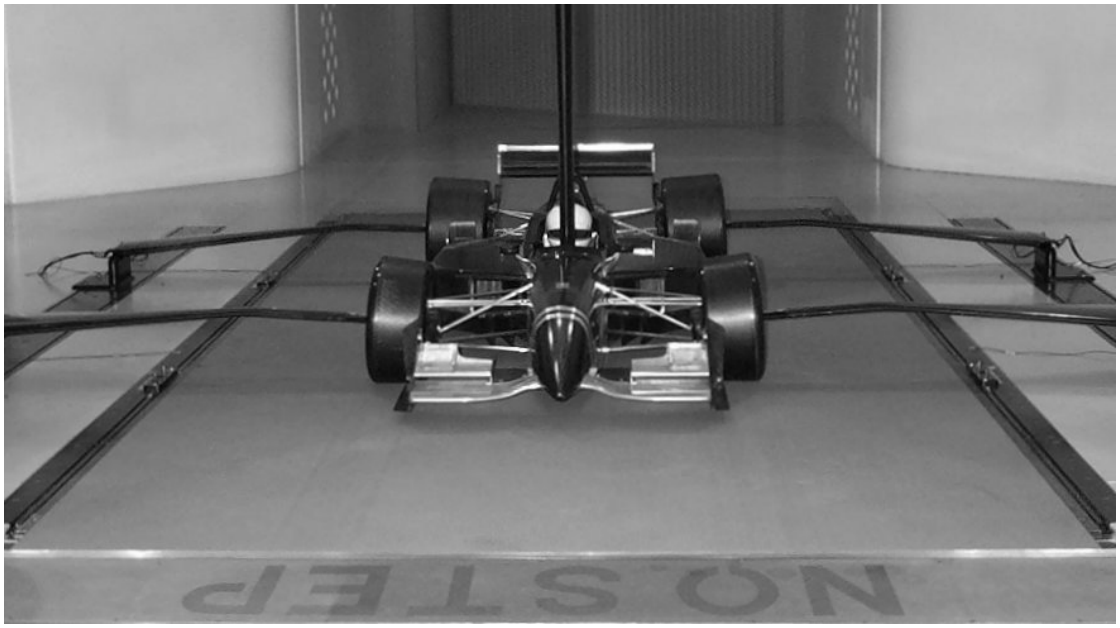

Figure 1.3: Champ Car in “Wheels-Off” Test Configuration

In general the wheels are not vertically restrained by the support stings and the only force applied to the belt is that due to the weight of the wheels and stings. This reduces wear and prolongs the lives of the belt and tyres. It does, however, mean that only drag can be resolved by the inclusion of a balance in the wheel support sting. As with the non-deformable tyre, this method of testing solves an immediate problem but introduces another. Do the wheel support stings affect the flow around, and hence the forces acting on, the model? Unpublished wind-tunnel test results from Champ Car manufacturer Reynard Motorsport concluded that the effect was significant enough to warrant the further investigation carried out in the present work.

The Reynard tests were carried out in an attempt to improve correlation between development carried out at the Royal Military College of Science (RMCS) and at their own facility in Indianapolis. A model was tested in a “wheels-on” configuration both with and without support stings. As the wheels were mounted on the model their forces could not be separated from those

acting on the body and therefore only global forces were reported. The wheel stings were not connected to the car and as such their drag was not measured, only their interference. During testing it was observed that the presence of the support stings increased the total model drag by 1–3 % depending on the sting used. To put this apparently small change into context there are components on the car which increase total down-force by 14 % at the cost of only a 1.1 % increase in drag. Interference of this level from a wind tunnel component is undesirable and a hindrance to effective racecar development.

2 Literature Review

> "Wheel aerodynamics is a topic which is little understood even by experts"
> A. Cogotti

This chapter starts with a brief discussion of relevant fundamental fluid mechanics. A detailed summary is then presented of the existing wheel aerodynamics research. The niche which the present work occupies is established and the aims of the project are set out with regard to the literature.

2.1 Fundamental Fluid Mechanics Elements

A combination of several physical attributes makes wheel flows unique and therefore direct comparison with more fundamental flows is difficult. Wheel flows imply the flow induced by the rotation of a low aspect-ratio circular cylinder in contact with the ground. These factors combine to produce a complex flow field which will be fully discussed in Section 2.2. Consideration of the individual flow elements can provide qualitative information as to the expected behaviour of the complete flow.

Rotation

The generation of a force perpendicular to the freestream by the axial rotation of a cylinder in a cross-flow is better known as the Magnus Effect. In the case of wheel flows, however, the main effect of rotation would appear to be the promotion of separation on the upstream-moving face [2] and the suppression of regular or periodic vortex shedding [3]. The same data also suggest that a cylinder rotating with peripheral speed equal to that of the freestream flow may be less sensitive to the effects of Reynolds number than when stationary.

Aspect-Ratio

End-effects are a major feature of the three-dimensional flow surrounding finite circular cylinders [4]. These end-effects also generate secondary flows such as axial transport of fluid in the immediate wake of the body. As aspect ratio decreases the interaction between the free ends increases, with the associated complication of the wake. At wheel-like aspect ratios, $(\mathrm{W}/\mathrm{D} \approx 0.5)$, a complex wake dominated by the effects of the free-ends can be expected. It is possible that the interactions between the ends could replace all regions of locally two-dimensional flow.

Circular Cylinder

The problems caused by the aspect-ratio make meaningful comparison with two-dimensional circular cylinder flows difficult. It is perhaps more informative to consider the cylinder as merely a bluff-body. This suggests that the upstream face of the body will be dominated by stagnated flow which will be accompanied by large regions of recirculating fluid in the wake.

Ground Contact

A non-rotating circular cylinder in free-air will generate no lift force, as the cylinder is brought into ground effect a net force towards the ground will act on the cylinder due to the constriction of the flow between the cylinder and the ground. This force will increase as the ground clearance reduces until either choked by the ground boundary layer or the components meet. When in contact the direction of the force is reversed with all flow accelerating over the cylinder and generating a lift force. In two-dimensional flow, contact with the ground was found to suppress regular vortex shedding [5].

All of the above factors conspire to produce a flow more akin to that surrounding a surface-mounted cube, or vertical cylinder, than any other. Such flows are no better represented than by Legendre and Werlé whose application of critical point theory (see Perry and Chong [6]) and striking flow visualisation are summarised in a paper by Délery [7].

2.2 Wheel Studies

Automotive aerodynamics evolved during the latter part of the 20^{th} century to become one of the most important areas of vehicle science. The initial objective was to increase fuel efficiency by reducing vehicle drag without resorting to radical styling. The automotive industry began using wind-tunnels built primarily for aerospace research, which included, or were retro-fitted with, fixed ground planes. In time the fixed ground planes were improved with the addition of boundary layer control methods such as fences, distributed suction, tangential blowing or elevated ground boards. Whilst this partially addressed the problem of the ground boundary layer, it did not provide wheel rotation. The adoption of a moving ground plane such as a rolling road would control boundary layer development and provide wheel rotation, but complicate the measurement of model forces using conventional balances. Component drag could easily be resolved, but measurement of lift through the continuous belt of a rolling road proved experimentally challenging. Three of the first four major investigations of wheel aerodynamics attempted to show that wheel rotation and a fixed floor could be combined and therefore conventional force balances could be retained.

Morelli [8] was the first to publish his investigation of the aerodynamic characteristics of an isolated wheel. A full-scale wheel was suspended from a conventional six-component balance above an elevated ground-board. In an attempt to simulate deformation, the tyre protruded

0.024D into a recess in the ground-board with an unsealed, 0.016D gap between the components. Morelli suggested a correction for the suction due to the presence of the gap and that its effect would be minimal. Extensive tests were performed over a range of wind speeds and yaw angles both with and without wheel fairings. Amongst his conclusions, Morelli proposed that an isolated wheel rotating in ground contact would produce a net down-force ($C_L \approx -0.075$).

Researchers at the Motor Industry Research Association (MIRA) were also investigating wheel flows at this time using a different approach. The work of Stapleford and Carr [9] used an idealised Formula One car model and investigated several parameters such as wheel ground clearance, wheel width-to-diameter ratio and the effect of a moving ground. The model was suspended above the ground plane and the wheels were rotated by motors housed within the model. It was not possible to rotate the wheels when in ground contact, therefore in the configuration representing zero ground clearance a paper seal was mounted on the ground to close the necessary gap. The decoupling of the model and ground meant that total forces could be measured with a conventional balance. Wheel forces were determined by subtraction of the forces measured during tare tests with no wheels present. The moving-ground work concluded that at all but the smallest ground clearances the effect of the ground on the model was insignificant. The remainder of the work was carried out over a fixed ground and was the first to measure static pressure distributions near the surface of the tyre using a static-pressure probe. The most significant conclusion was that a wheel rotating in ground contact produced a significant lift-force ($C_L \approx 0.4$), contrary to Morelli [8].

The third of these similarly-focused studies began five years later as Cogotti [10] attempted to clarify the previous disparate conclusions. His 'test bench' comprised two full-scale wheels on the same axle rotated by a faired electric motor also on the axle. The height of the whole unit could be adjusted to simulate different ground clearances. The ground contact case was approached similarly to MIRA [9] with the necessary clearance closed using a foam rubber seal the same size as the contact patch. Force measurements were made using an underfloor balance to which all components were connected. The results of the work agreed qualitatively with that of Stapleford and Carr [9] and confirmed that, despite correction, the conclusion of Morelli [8] was untrue, a wheel rotating in ground contact always produced a lift force.

All of the above work had focused on the development of a method by which the forces acting on rotating wheels could be determined using a conventional balance. The work of Fackrell [11–13], published between that of Stapleford and Carr [9] and Cogotti [10] resolved the net forces by integration of the wheel surface static pressures. A series of static tappings were made through the tyre and hub and connected to an internal pressure transducer. Each tapping was sampled individually over several wheel rotations with the pressure history recorded and averaged. The location of the tapping at each sample time was determined using a trigger signal to indicate the start of a revolution. All signals were recovered using a slip-ring arrangement as the entire pressure measurement system rotated with the wheel. A system of rods, arranged to resemble a racecar suspension was used to support the wheel on a rolling road. All testing was carried out at a constant Reynolds number of 5.3×10^5. In total, six wheels were tested both stationary and

rotating in contact with the rolling road to investigate the effect of rotation, and the relationship between net force and aspect ratio. Amongst more far-reaching conclusions, Fackrell's data were in qualitative agreement with Stapleford and Carr [9] and Cogotti [10] regarding the direction of the lift force, $(C_L > 0)$.

Whilst Stapleford and Carr [9] were the first to present the pressure distribution around stationary and rotating wheels, Fackrell was the first to present non-intrusive measurements. Both of these studies were in qualitative agreement despite the different acquisition methods. Figure 2.1 illustrates that wheel rotation acts to reduce both drag and lift forces, although the effect on the latter is greater. The figure also illustrates the two regions that Fackrell suggests govern the flow-field of a rotating wheel, the contact patch $(\theta = 90^\circ)$ and separation $(\theta \approx 280^\circ)$.

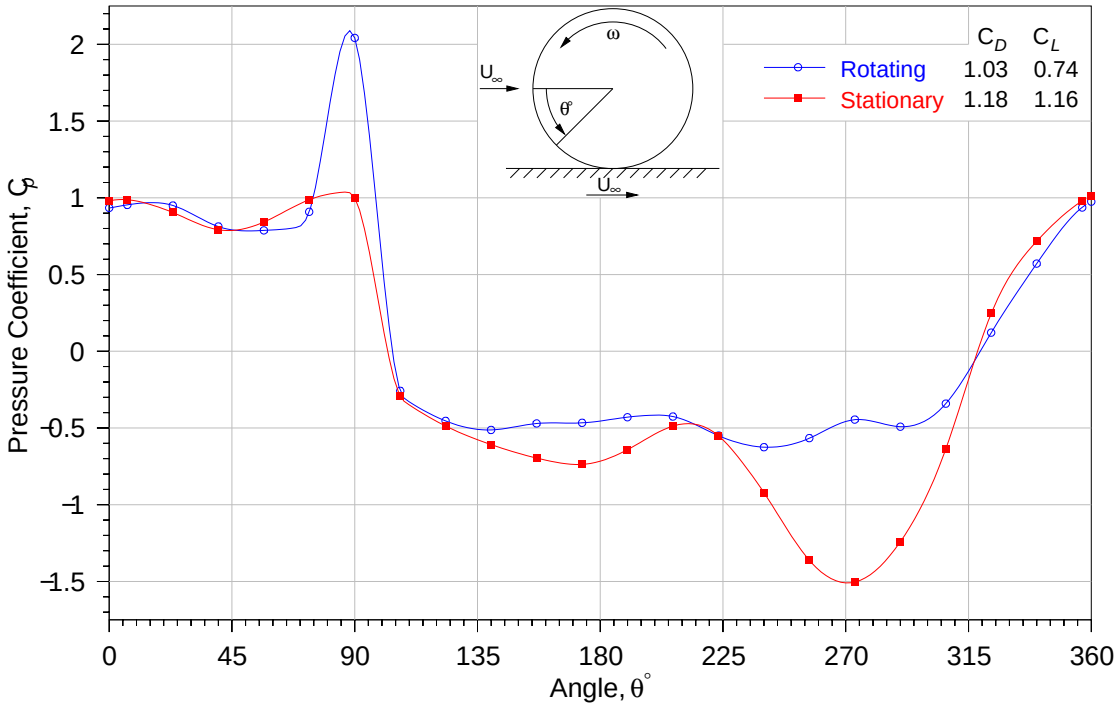

Figure 2.1: Centreline Pressure Distributions for Rotating and Stationary Wheels – Fackrell [12]

Contact Patch Region

Just upstream of the contact patch Fackrell recorded a pressure spike $(C_p > 2)$, indicating that work was being done on the fluid in that region. Fackrell did not investigate this area further experimentally but theorised that the necessary work was being done by the convergence of the moving ground and tyre surfaces. He calculated that the tangential convergence of two moving surfaces would generate an upstream jet of fluid immediately in front of the contact patch and that the jet velocity would be approximately half that of the freestream. He also made the complementary proposition that the diverging surfaces at the rear of the contact patch would generate an inflow to the rear of the same order of magnitude. Fackrell did not measure a suction

peak corresponding to this phenomenon and suggested that this was due to the suction lifting the rolling-road belt and attenuating the effect.

Separation Zone

Fackrell observed that wheel rotation moved the flow separation zone upstream, correlating with the reduction in lift force. In Figure 2.1 the flow separates downstream of the top of the stationary wheel at approximately 210° compared with 280° when rotating. Fackrell investigated this region further using a boundary layer probe and found that the flow did not separate from the surface of the rotating tyre but rather from a layer in the fluid just above the surface. Fackrell found that the motion of the wheel induced the rotation of the thin annulus of air surrounding it. In the region of separation this fluid is moving upstream against the freestream flow. Separation therefore occurs just above the tyre surface, at the point in the fluid at which tangential velocity is zero.

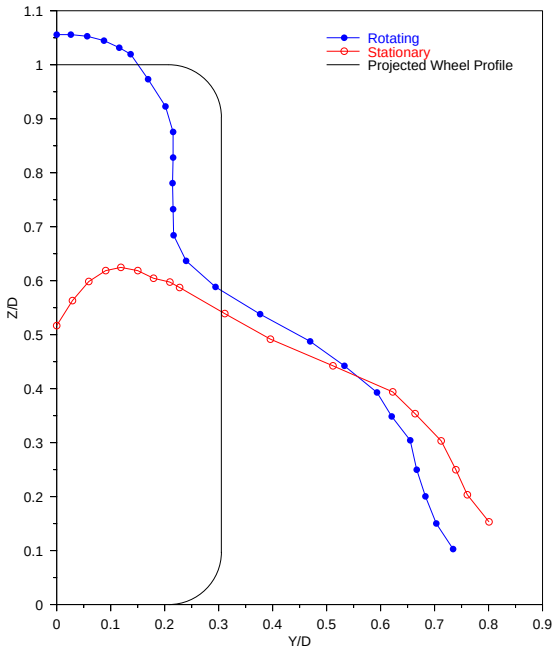

Figure 2.2: Contour of 90% Total Head (0.87D Downstream of Wheel Axis) – Fackrell [12]

In addition to surface pressure measurements, Fackrell also carried out an investigation in the near-wake of one of the wheels. A Kiel tube was used to measure total pressure in planes perpendicular to the freestream flow. A contour of 90% total head was used to delineate the approximate edge of the wake and illustrate its shape. The effect of rotation on the shape of the wake is shown in Figure 2.2. The data collected on the support-strut side of the wheel were omitted by Fackrell from this figure as “their wakes would only confuse the picture.”

Fackrell suggested that the increased height of the wake was due to flow separation before the top of the wheel and that the lobe present near the ground was due to the influence of the contact

patch jet. A similar lobe can be seen in the stationary wheel contour but this was presumed to be a horse-shoe vortex around the wheel which formed following the upstream separation of the ground boundary layer.

Fackrell [11–13] had successfully shown that rotation and ground motion were essential to correctly simulate isolated wheel flows. It remained for several subsequent studies to confirm that a moving floor and/or rotating wheels were essential for correct full-vehicle simulation. These included the work on road cars of Hackett et al. [14] at Ford, Bearman et al. [15] at Imperial College and Merker et al. [16, 17] with General Motors, and on racecars by Wildi [18] and Mueller, Singer and Eckert [19] at Porsche.

Bearman et al. [15] also included the results of further work carried out using Fackrell's wheel. Two planes of measurements were made 2.5D downstream, one with the wheel stationary and one with it rotating on a moving ground. A 9-hole probe was used and the data presented as contours of total pressure and vorticity. The vorticity data revealed that the wake at this downstream location was dominated by a contra-rotating vortex pair near the ground. The vortex pair in the wake of the rotating wheel were found to be centred approximately 0.25D above the ground and be of much lower intensity than those behind the stationary wheel which were centred just above the ground. The sketch shown in Figure 2.3 represents the trailing vortex pair, of which Bearman was the first to measure their rotational sense. This work confirmed, as far as was possible, Fackrell's conclusion [12] that the vortices surrounding the stationary and rotating wheels were generated by different mechanisms.

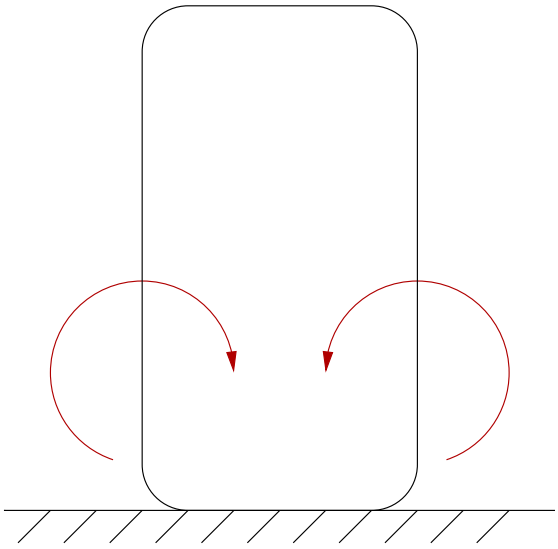

Figure 2.3: Schematic of Vortex Location and Sense 2.5D Downstream of Wheel Axis – After Bearman [15]

There has been increased research in recent years into the aerodynamics of rotating wheels following the adoption of moving ground planes in automotive wind tunnels. A vast amount of this work has been driven by the motorsport industry, in particular by the constructors of monoposto (single-seat) racing cars. In racing such as Formula One and Champ Car the wheels are almost

completely exposed to the airflow and as such research into the aerodynamics of isolated wheels has increased. Meanwhile, the road car industry has rightly pursued the aerodynamics of wheels rotating within wheel housings. The following sections discuss the main areas covered by recent research.

2.2.1 Surface Pressure Measurement

Resolving the lift force acting on a wheel rotating in ground contact remains a difficult task. Whilst the pressure-integration method that Fackrell [12] used was successful, it was not industrially viable because of the time required to collect the data from each tapping sequentially. Two studies have attempted to improve the industrial viability of the method by using multiple, high-frequency, battery-powered transducers and radio transmission of the signal.

The first such work was carried out by Hinson [20] in which she evaluated the performance of a commercially-available rotating, pressure-measurement system. The collected data were compared with Fackrell [12] and found to give good qualitative agreement, capturing the contact patch jet and upstream separation, despite different wheel geometries. The work served to reinforce that of Fackrell rather than extend it.

A second pressure measurement system was created by Mears [21–24] by instrumenting a pneumatic go-kart wheel. The performance of this system, coupled with an improved moving ground simulation, allowed Mears to be the first to resolve repeatably a suction peak immediately downstream of the contact patch. The presence of this peak was proposed by Fackrell [12] but not observed. Further investigation of this result was carried out using two-dimensional particle image velocimetry (PIV) on the wheel centreline aligned with the freestream flow [23]. The PIV data, presented as vectors, showed an increased in-plane velocity immediately after the contact patch in the direction of the moving surfaces. It did not resolve the inflow, towards the contact patch, at half the magnitude of the freestream suggested by Fackrell. This result serves to illustrate the three-dimensionality of the flow in the wake of the wheel and that, even on the wheel centreline, two-dimensional assumptions and measurements may not be valid.

2.2.2 Deformable Tyres

All of the previously-mentioned work has been carried out using non-deformable tyres, even the pneumatic tyre used by Mears was run at sufficiently high pressure as to be essentially solid. This is mainly due to issues with repeatability and longevity of deformable tyres and also the possibility of catastrophic failure, especially with pneumatic tyres. Successfully replicating the deformation of a tyre at model-scale is difficult and requires the application of a large load, relative to the weight of the wheel, onto the moving ground belt, increasing belt wear. The use of non-deformable tyres is at the cost of correct contact patch and tyre shoulder geometries. A solid tyre contact patch is reduced to a line and the upper and lower shoulders are identical due to the requirement for rotational symmetry. This also means that a cambered tyre profile generates

a conical wheel when revolved about its axis of rotation. The effect of camber on the wake of a non-deformable wheel is discussed by the author in [25].

One successful study of the effect of contact patch area on wheel wake was carried out by Purvis [26] using a 50%-scale tyre constructed from polyurethane foam. The low-density foam was easily deformed by the application of minimal vertical load, however it did suffer from degradation which it was thought could have been improved by the application of a more durable coating. Measurements of total pressure were made in planes perpendicular to the freestream flow with varying degrees of tyre deformation. The width of the wake was found to increase as contact patch size (tyre deformation) was increased.

This is an area which may subsequently receive more attention, especially from racing teams, if stainless-steel rolling-road belts become more prevalent. These belts run on an air-bearing and can withstand a deforming load without the frictional heating suffered by a conventional belt.

2.2.3 Housed-Wheel Flows

An area that has received less attention than isolated wheel flows is the study of wheels rotating within a housing or arch. Whereas isolated wheel research has been pursued by racing-car manufacturers, the housed-wheel flows have historically been supported by road-car manufacturers. Merker et al. [16] touched on the effect of the wheel housing on overall car forces in their comprehensive study of a full-scale sports coupé with General Motors. More fundamental work was carried out by Axon [27–29] and Skea [30, 31] the former in association with Rover and the latter with Jaguar. Whilst the effect of wheel housings is not of direct interest in this work it must be noted that both Axon and Skea produced two of the first validated computational fluid dynamics (CFD) simulations of isolated wheels as preparatory work.

2.2.4 Computational Simulation

Basara, Beader and Pzulj [32] joined Axon [28] and Skea [30] in being the first to publish the results of CFD studies of wheel flows, doing so in the late 1990s. Each study used a different commercial, finite-volume code based upon the use of structured grids and Reynolds Averaged Navier-Stokes (RANS) equations. The effect of turbulence model and solver numerics were assessed in each case although no consensus was reached.

Axon [28] used Fackrell's surface pressure and wake data [12] as validation criteria for his isolated wheel simulations. Both of these showed reasonable correlation notwithstanding the fact that Axon greatly simplified the wheel geometry. In particular, Axon's model appeared to capture correctly the upstream contact patch jet. The work of Basara, Beader and Pzulj [32] took a similar approach to Axon, although was more limited in its scope as it was essentially a promotional exercise by the supplier of the CFD code. Skea [30] used a simplified wheel model in both his experimental and computational work, and used surface pressure data from his experimental phase in his computational validation.

Whilst the isolated wheel data produced by these studies did not add to that of Fackrell, it did show that CFD could be used to provide qualitative information about this type of flow-field. One particular cause for concern was the poor prediction of flow separation by all turbulence models and discretisation schemes.

It is unsurprising that some issues remain as the RANS turbulence models currently used are essentially those used by Axon, Skea and Basara, Beader and Pzulj in those first studies. Current studies serve to illustrate the improvement in CFD simulation which has been brought about by increased computational power and enhanced meshing and solution strategies. However, the work of Wäschle et al. [33] showed that improved predictions of both the flow-field and lift-force were possible with a code based not upon RANS, but on the Lattice-Boltzmann method. In this work two commercial codes were compared and the results validated using force, pressure and velocity data collected by the authors.

2.2.5 Velocity Measurement

Bearman [15] was the first to collect velocity data in the wake of a wheel using a multi-hole probe, a technique subsequently employed with success by Mears [21–24]. The results of these investigations further clarified the structure of the wake downstream of an isolated wheel by resolving the ground vortex shown schematically in Figure 2.3.

Cogotti and De Gregorio [34] also applied this technique to full-scale, housed-wheel flows, measuring the ground vortex at the exit of a wheel-arch. A single plane, perpendicular to the freestream, was investigated using particle image velocimetry (PIV) and laser Doppler anemometry (LDA) in addition to a multi-hole probe. Only in-plane (two-dimensional) data were recorded and all three techniques were found to be in good agreement. The work did not aim to investigate the flow, but prove that non-intrusive laser-based flow diagnostics can be applied to full-scale automotive testing. The authors concluded that the application of these techniques, especially PIV, in a large wind tunnel environment was “not easy, often rather difficult.” The problems encountered ranged from reflections and glare to low seeding density and exceptionally low data-rates.

The most complete investigation of the velocities in the wake of an isolated wheel was carried out by Nigbur [35]. Three-dimensional velocities were measured using a hot-wire anemometer (HWA) in 10 planes perpendicular to the wake of a 50%-scale Formula One wheel. The data were presented as time-averaged contours for each velocity component along with contours of the associated root-mean-square (RMS) fluctuations. As the in-plane (V–W) components were not combined into vectors it was impossible to analyse the vortical structures in the wake. However, the streamwise (U) data were more informative, exhibiting the shape measured by Fackrell et al. and showing regions of high turbulence intensity, particularly in the wake of the support strut. Unfortunately, the HWA was insensitive to the direction of the streamwise component and therefore no regions of reversed flow were identified. Also, the moving ground plane was approximately the same size as the wheel and therefore could not suppress fully the

boundary layer growth. It was presumed that this was the cause of the strong asymmetry noted in the wake.

2.2.6 Near-Wake Models

Figure 2.4 presents two independent and contradictory models of the structure of the flow downstream of an isolated wheel rotating in ground contact. Each arrow on the figure represents the projection of a streamwise trailing vortex and illustrates its size and rotational sense. Both models were proposed from consideration of vortex theory and not from measurements of velocity in the near-wake. It was proposed that:

- the upper vortices are conventional trailing vortices as associated with lifting bodies;
- the middle or hub vortices are formed by flow leaving the hub with rotation along the wheel axis and being turned by the main flow to a stream-wise orientation;
- the lower vortices originate from the strong viscous actions in front of the tyre contact patch; these vortices were termed “jetting vortices” by Merker and Berneburg [17].

Notwithstanding the fact that the theoretical model in Figure 2.4(a) is contradicted and pre-dated by the experimental work of Bearman et al. [15] and that there is a lack of velocity data to support Figure 2.4(b), both models have been accepted and re-published in respected reference works. Cogotti appears in Racecar Vehicle Dynamics [36], and Merker and Berneburg in Aerodynamics of Road Vehicles [37]. Further investigation is required to either reinforce or revise these models as appropriate.

2.3 Sting Effects

Automotive aerodynamics has often borrowed aeronautical testing practices including its approach to the interference effects of model support struts. The force acting on the struts is determined by testing them alone and using this as a correction in tests with the model present. More elaborate methods, such as those described by Barlow, Rae and Pope [38], for example the use of image stings placed opposite the supports, are seldom employed. It is difficult to determine the accuracy of these types of force corrections for model-scale testing as data cannot currently be gathered from an unsupported model.

For the same reasons it is also difficult to assess the effect of supports upon the flow-field surrounding a model. Consideration of the flow surrounding an isolated support, however, would suggest that its surrounding flowfield, and hence forces, would differ greatly in the presence of a model. Taylor, Gursul and Greenwell [39, 40] have carried out an excellent investigation of the effect of support stings on wake vortex systems. A delta wing was tested at high angles of attack

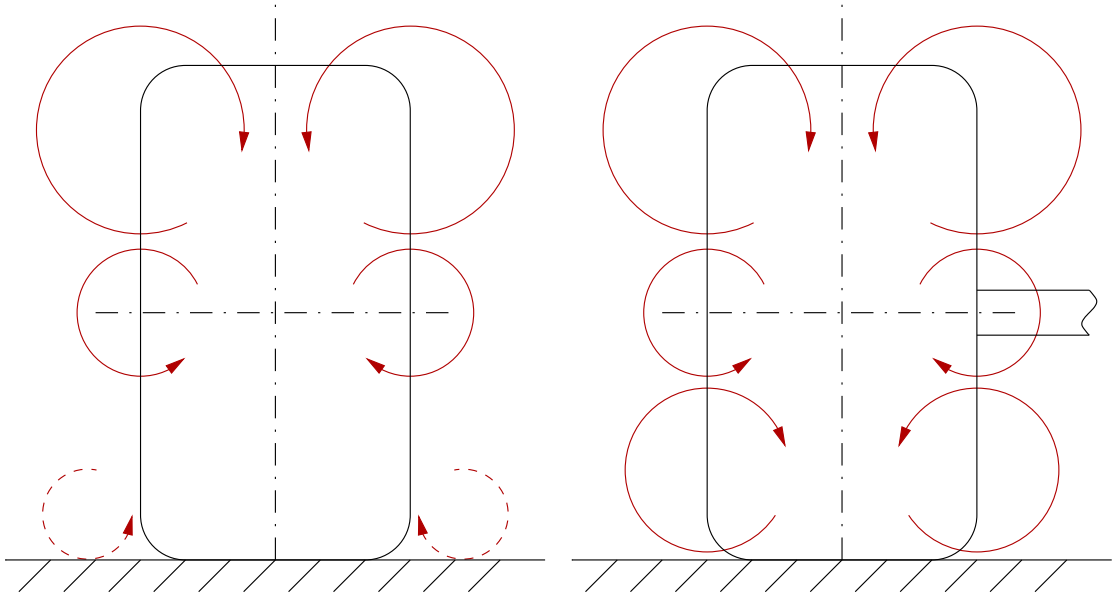

(a) After Cogotti [10]

(b) After Merker and Berneburg [17]

Figure 2.4: Models of the Trailing Vortex System Induced by a Wheel Rotating on the Ground

in a water tunnel with dye injections used to visualise the convection of the leading-edge vortices. They found that the presence of a dummy sting, in addition to the mounting sting, resulted in premature vortex breakdown. The magnitude of the strut interference varied with its position and wing angle of attack but at its most severe the effect could be observed far upstream.

Automotive studies of support interference are further complicated by the widespread use of moving ground planes, reducing the option for support placement. Page et al. [41] recommended supporting wind tunnel models from the rear as the stings would have less impact in a region of disturbed flow. A system such as this can be found in the Deutsch-Niederländischer Windkanal (DNW), as used by Merker et al. [16].

Hetherington and Sims-Williams [42] measured the interference effects of both wheel stings and overhead model mounts. A road-car model was supported above a fixed ground plane by an underfloor balance and forces were recorded with and without dummy stings. Wheel rotation was not included and flow-field measurements were not made. The struts were found to have a measurable effect on the overall model forces. In particular, the addition of front and rear wheel stings increased the vehicle lift by approximately 4 % whilst having minimal impact on drag.

2.4 Summary of Wheel Aerodynamics Literature

Table 2.1 summarises the literature regarding investigations into the aerodynamics of rotating wheels. The motion of the wheel and ground along with the test Reynolds number are indicated

along with the main measurements made and the use of computational methods. The “ground” columns refer to the condition of the ground used in the tests of rotating wheels. The use of a fixed ground for stationary wheel tests is implied with the exception of Merker [16] who used a moving ground at all times. The test Reynolds number, based on wheel diameter, is reported where available and in the case of a range of tests represents the highest value tested. The measurement section refers to the wheel alone and does not include measurements made on wheel housings.

2.5 Aims & Objectives

This literature review has shown that the flowfield surrounding, and therefore the forces acting on, a wheel are not fully understood. This is the case whether the wheel is rotating or stationary, however sufficient work has been done to show that automotive testing should be carried out with wheels rotating in contact with a moving ground plane.

Resolution of wheel forces has been a priority in the literature as force data are often the only output of industrial wind tunnel testing. As these force measurement techniques mature attention must move to the investigation of the flowfield surrounding an isolated wheel. An improved understanding of this area will help to clarify interactions between the wheel and nearby components, creating potential opportunities for design optimisation. This review has also highlighted the interference effect of model support stings and that they have a measurable impact on model forces.

The current project will aim to clarify the disparate literature and identify the prominent features of the wake of an isolated wheel rotating in ground contact. Complementary studies will be performed using computational simulation and full-car testing in an attempt to isolate these features. The main aim will be accompanied by four other novel objectives:

1. to identify the support sting interference effects on an isolated wheel wake;
2. to investigate the qualitative relationship between sting design and interference effect;
3. to evaluate the effect of the presence of a car on the wheel flowfield;
4. to confirm the support sting interference effects in the presence of a car.

The data produced will also be used to revisit the flow models presented in Figure 2.4.

Table 2.1: Summary of Wheel Aerodynamics Literature

Author & Ref.	Type		Wheel		Ground		Re	Measurements
	Exp.	CFD	Stat.	Rot.	Fix.	Mov.		
Morelli [8]	✓			✓	✓		1.25×10^6	6-Comp. Forces
Stapleford & Carr [9]	✓		✓	✓	✓		2.0×10^5	L & D, SurfaceP
Cogotti [10]	✓		✓	✓	✓		1.1×10^6	L & D
Fackrell [11–13]	✓			✓			5.3×10^5	L & D, SurfaceP
Bearman et al. [15]	✓		✓	✓		✓	5.5×10^5	9-Hole
Merker et al. [16, 17]	✓		✓	✓		✓	n/a	L & D, WakeP
Hinson [20]	✓			✓		✓	5.6×10^5	L & D, SurfaceP
Mears [21–24]	✓	✓	✓	✓		✓	2.5×10^5	L & D, SurfaceP, PIV, 5-Hole
Knowles et al. [25]	✓			✓		✓	3.7×10^5	D, 3D-LDA
Purvis [26]	✓			✓		✓	5.5×10^5	WakeP
Axon [27–29]	✓	✓	✓	✓		✓	8.5×10^5	D
Skea [30, 31]	✓	✓	✓	✓		✓	5.5×10^5	D, SurfaceP
Basara [32]		✓					n/a	
Wäschle et al. [33]	✓	✓	✓	✓		✓	5.4×10^5	D, WakeP, 2D-LDA
Cogotti & De Gregorio [34]	✓			✓		✓	n/a	PIV, 2D-LDA, 14-Hole
Nigbur [35]	✓		✓	✓		✓	4.3×10^5	HWA

Measurement Key:
L(Lift), D(Drag), SurfaceP(Tyre Surface Static Pressure), WakeP(Wake Total Pressure), X-Hole(Multi-Hole Probe Velocities)
LDA (Laser Doppler Anemometry), PIV (2D Particle Image Velocimetry) and HWA (Single-Wire Hot Wire Anemometry)

3 Experimental Method

This project featured two distinct experimental phases (Phase One with a 40 %-scale Champ Car wheel, and Phase Two with a 50 %-scale F1 wheel), which presented different problems requiring adaption of the experimental procedure. These adaptations have been viewed as deviations from a generic experimental procedure. It is this generic procedure that is presented in this chapter, leaving the minor deviations to the discussion of each phase. Detailed system settings can be found in the relevant appendices. A schematic of the generic set-up is shown in Figure 3.1 and the major components described in the following sections.

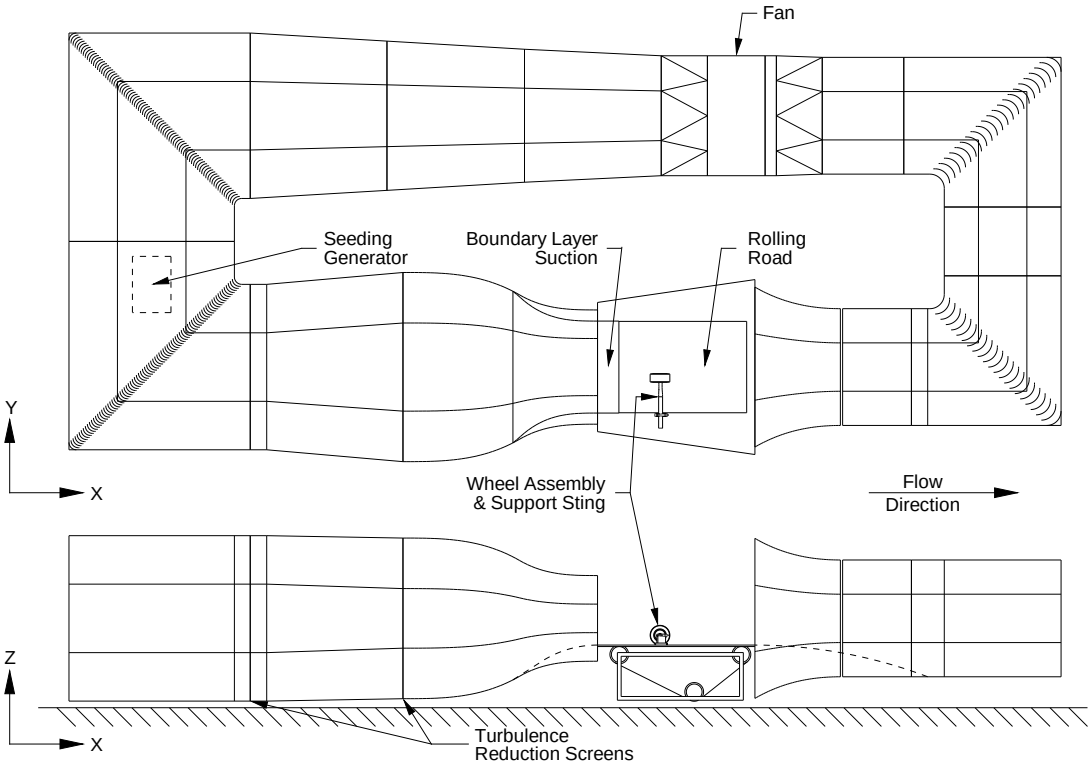

Figure 3.1: Schematic Representation of Experimental Set-up

3.1 Wind Tunnel

A closed-return, three-quarter open-jet wind tunnel, such as that shown in Figure 3.1 was used for all testing. The facility included a continuous-belt rolling road system which was synchro-

nised with the tunnel freestream velocity. This was used as ground simulation and to provide wheel rotation. Suction was applied through the floor immediately after the nozzle exit to remove the tunnel boundary layer. A-priori optimisation of the level and distribution of the suction, coupled with knife-edge transition to the belt, ensured minimal belt boundary layer. Distributed suction was also applied to the underside of the rolling-road belt to eliminate the belt lifting caused by aerodynamic loading and/or belt expansion. Air and road temperatures were held constant $(25 \pm 0.5°\mathrm{C})$ throughout testing by individual chiller units.

3.2 Test Components

Figure 3.2 provides an exploded view of a typical test configuration which comprised a wheel assembly and associated support sting. Each of the major components are indicated in the figure and discussed in this section. All of the components were in active service in racecar aerodynamic development when tested and as such represented the state-of-the-art in wind tunnel equipment.

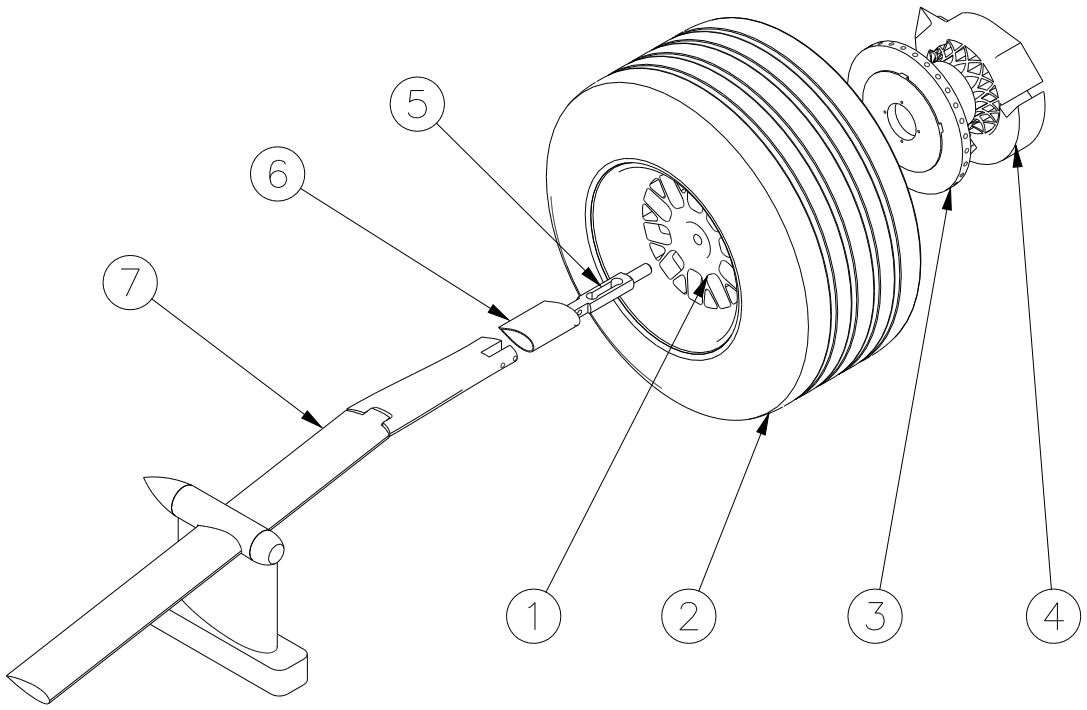

Figure 3.2: Exploded View of Typical Test Components

Key:	4 = Suspension Upright
1 = Wheel Hub	5 = Wheel Drag Loadcell
2 = Non-Deformable Tyre	6 = Loadcell Shroud
3 = Brake Rotor	7 = Support Sting

Wheel Assembly

Parts 1-4 in Figure 3.2 make up the wheel assembly. The model-scale hub (1) was machined from aluminium and featured two ultra-low-friction bearing units upon which it rotated. The hub was a detailed scale replica of the hub used on the actual race car including the intricate spoke pattern. A non-deformable carbon-fibre tyre (2) with a lacquered surface finish was mounted on the hub.

The wheel assembly was completed by a ventilated brake rotor (3) and a suspension upright (4) both equally as detailed as the hub. The brake was mounted directly on the hub and as such rotated with it acting as a centrifugal pump. The upright was held stationary by mounting it on the support strut assembly. Both components provided a blockage to flow through the spokes and also partially filled the deep cavity of the hub making the isolated wheel assembly geometrically similar to the conventional configuration mounted on a racecar.

Support Sting

The wheel assembly was positioned and restrained by the support, comprised of parts 5-7 in Figure 3.2. The wheel was attached directly to a single-component, 50N loadcell (5) oriented to measure drag force. The bluff loadcell was shrouded by a carbon-fibre cover (6) which extended the symmetrical aerofoil section of the support sting (7) to the face of the wheel. The loadcell cabling was routed inside the body of the sting and as such provided no obstruction to the flow. The sting was mounted immediately beside the rolling road in a position similar to that in which it would sit if a full car were tested, see Figure 3.1. The reaction force between the belt and wheel was that due to the weight of the components. The sting applied no additional force to the wheel and routine checks with a stroboscope and optical tachometer showed there were no problems with wheel vibration or slipping during testing.

3.3 Laser Doppler Anemometer

The three-component laser Doppler anemometer used in this study was a Dantec FibreFlow system comprising one single-component probe and one dual-component probe. Both probes operated in back-scatter mode and had a 1m focal length. Each component was measured with a distinct wavelength of laser light originating from a multi-line argon-ion source. The fibre-optic beam delivery system included a Bragg cell, used to frequency shift one of each of the three beam pairs by 40MHz, allowing resolution of flow direction as well as magnitude.

The probes were rigidly mounted to a computer-controlled, three-component traverse and aligned such that their measurement volumes were coincident within a 25μm pinhole. The axes of the traverse were parallel to those of the wind tunnel. The signal from each beam pair was processed by a dedicated Burst Spectrum Analyser (BSA). All equipment was centrally controlled by Dantec BSA Flow software v.1.4.

Whilst the traverse was aligned with the tunnel axes, it did not physically permit alignment of the probes with their respective velocity components. This necessitated off-axis measurement of the horizontal, transverse velocity component, v. Whilst optical access to the road surface demanded that the vertical component, w, was also measured off-axis. Despite being off their respective major axes, both components remained in the plane of interest. The probe set-up was optimised to minimise off-axis measurement errors whilst maximising the measurement area. The transformation of the measured components to v and w is detailed in Appendix D. The u-component (in the freestream direction) was measured directly and required no transformation.

Flow seeding was provided by a JEM Hot2000 fog generator. Originally designed as a theatrical special effects machine, this system was found to be an exceptional flow seeder producing high volume, ambient temperature seeding, with a constant mean particle size of 1.3μm from a fluid which was 85 % water. The generator ran continuously throughout the tests, positioned inside the wind tunnel duct.

A brief investigation was carried out to determine the effect of the seeder wake on the flow in the working section. An uncalibrated hot-wire was used to traverse the working section with and without the seeder in the duct. It was found that with the seeder in the position indicated in Figure 3.1 the presence of a set of cascades and the turbulence-reduction screens effectively redistributed the seeder wake. Seeding density was adequate at all times although it reduced with time due to deposition on the screens which were routinely cleaned to avoid further degradation of seeding density and flow quality.

Flow quality was further preserved by the non-intrusive nature of the LDA technique and the test set-up which allowed the probes to remain outside the wind tunnel jet throughout testing.

3.4 Test Procedure

The main objective of the tests was to extract three-dimensional mean velocity data from the near-wake of the wheel. For the purposes of this study, the term near-wake will refer to the region less than one diameter downstream of the wheel. No data points were sampled from outside this region as it was felt that the flow structures in this area should be resolved before investigation of their diffusion downstream. All tests were carried out at constant velocity with the wheel in motion and as such did not address Reynolds number effects nor the relative effect of rotation due to the lack of a stationary datum case.

The data points were arranged in a regular grid approximately one wheel diameter square and perpendicular to the freestream, effectively extracting a slice of the near-wake. An illustration of the position and type of one of these measurement planes is given in Figure 3.3. The plane, centred about the wheel centreline was replicated at several streamwise locations within the region of interest.

The spatial resolution of the measurement plane was dictated by the length of the measurement volume in the Y-direction, and the resulting positional uncertainty, discussed further in

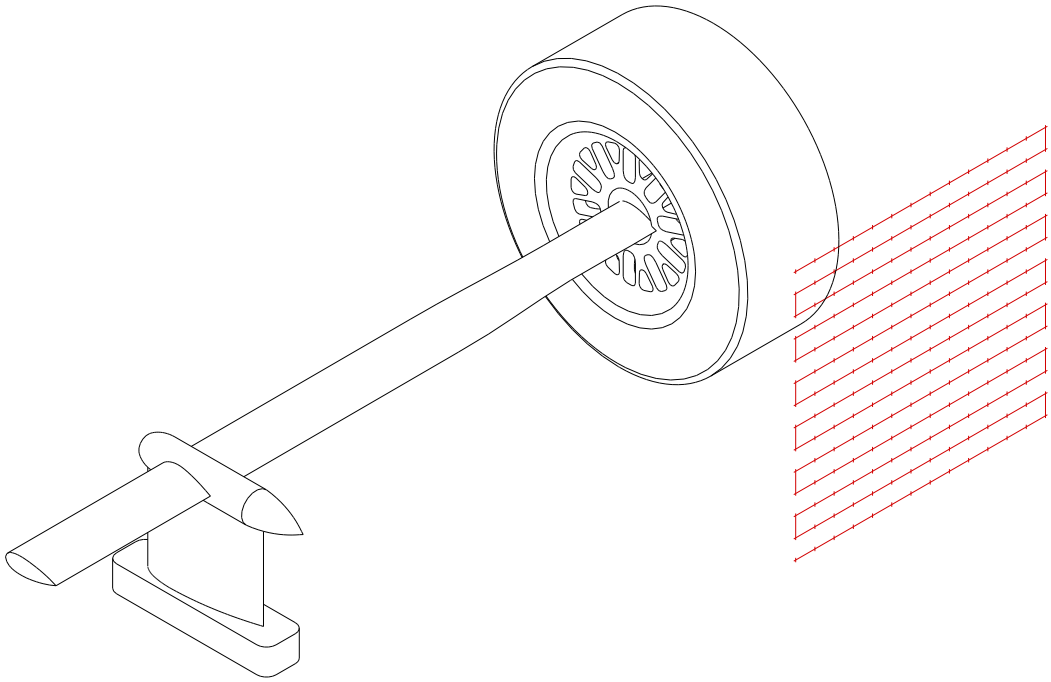

Figure 3.3: Example Measurement Plane

Appendix E. The grid was spaced to ensure the measurement volume at each point was unique, and did not overlap that of other points.

It was not possible to predetermine the time taken to gather a certain number of samples due to the stochastic nature of LDA sampling. In all tests, and for all measurement points, the maximum sampling time and maximum number of samples remained constant, reaching either target would trigger movement to the next point. This was an attempt to maximise the sample population without an excessive acquisition time. A five second pause was inserted after each movement of the traverse in order to allow any induced probe vibration to decay.

Finally the off-axis measurements were transformed into the tunnel frame-of-reference using the method outlined in Appendix D, to yield planes of time-averaged three-dimensional velocity data. On-axis measurement of u-velocity also permitted calculation of it's standard deviation, σ_u.

Wheel drag force data were measured using the loadcell integrated into the test assembly and coupled to the wind tunnel control system. The frictional contact forces were determined by testing the wheel rotating without wind and were used to correct the mean drag force measured under full test conditions.

3.5 Post-Processing

All of the velocity data were non-dimensionalised by the freestream velocity u_∞, and the distances expressed in multiples of the wheel diameter, D. Also the projected profile of the wheel (and sting if present) is included in all plots for reference.

Flooded contours of mean u velocity were generated to illustrate the shape and extent of the near-wake shear layers. The regions of upstream or reversed flow have been delineated by the use of dashed contour lines. The availability of the standard deviation of the u-velocity component was exploited to provide limited information on the turbulence distribution in the wake. The streamwise-component of local turbulence intensity, $Ti_u$was plotted as filled contours. Ti_u is defined as the ratio of the standard deviation of the u component, σ_u, to the local mean velocity magnitude:

$$Ti_u = \frac{\sigma_u}{\sqrt{\left[\overline{u}^2 + \overline{v}^2 + \overline{w}^2\right]}}$$

where the overbar denotes the component mean value. The remaining components of Ti could not be established as the velocity standard deviations were unavailable.

The velocity components in the plane of measurement, v and w, were visualised using two different techniques. Firstly, conventional velocity vectors were used to represent the magnitude and rotational sense of the measured wake structures. However, the sparsity of the vector field did not clearly illustrate the shape, extent and interactions of these structures, which were more easily visualised using a secondary technique, line integral convolution (LIC, section 3.5.2). A vortex identification routine was also developed by the author to automatically extract and classify the critical points present in the in-plane data (Section 3.5.1)

The three components of velocity were not combined as the resultant three-dimensional visualisations did not lend themselves to two-dimensional representation on paper. Similarly the in-plane data were not presented as contours of streamwise vorticity as these did not aid in clarification of the wake. Figure 3.4 shows a typical vorticity plot of Phase One data. This type of plot did not illustrate the size and location of the vortical structures as effectively as LIC.

Line graphs of the individual components of velocity at $Y/D = 0$, the tyre vertical centreline, and $Z/D = 0.5$, the tyre horizontal centreline, were also used to provide further comparison between datasets.

3.5.1 Vortex Identification

A routine was developed which analysed the in-plane velocity components of each measured plane and reduced the data to the critical points in the flow field. Performing this analysis computationally removed the subjectivity associated with visual inspection of vector maps or LIC images.

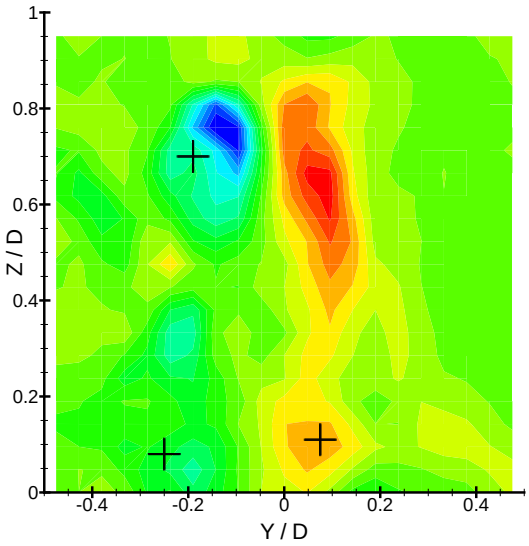

Figure 3.4: Contours of Streamwise Vorticity – Crosses $(+)$ Indicate Vortex Centres

The routine proceeded in two stages, firstly all critical points present in a plane were located. In two-dimensions critical points occur where the zero-contour lines of the velocity components intersect. Figure 3.5 shows a critical point at the intersection of the zero-contour lines of v (solid line) and w (broken line).

The classification of the located critical points was based on the method detailed by Peikert [43] which uses properties of the point's Jacobian, ∇p (matrix of first partial derivatives) where;

$$\nabla p = \begin{bmatrix} p_{x,x} & p_{x,y} \\ p_{y,x} & p_{y,y} \end{bmatrix}$$

The properties of this matrix that are of particular interest are;

$$q = -\text{trace}(\nabla p) = -(p_{x,x} + p_{y,y})$$

$$r = \det(\nabla p) = p_{x,x}p_{y,y} - p_{x,y}p_{y,x}$$

The classification of a critical point using these properties is summarised in Table 3.1 for the two main critical points of interest in this work, foci and saddles.

3.5.2 Line Integral Convolution

Line Integral Convolution (LIC) is a visualisation method which, when applied to fluid-dynamics vector fields, generates images reminiscent of long-exposure surface-tracer photographs of wa-

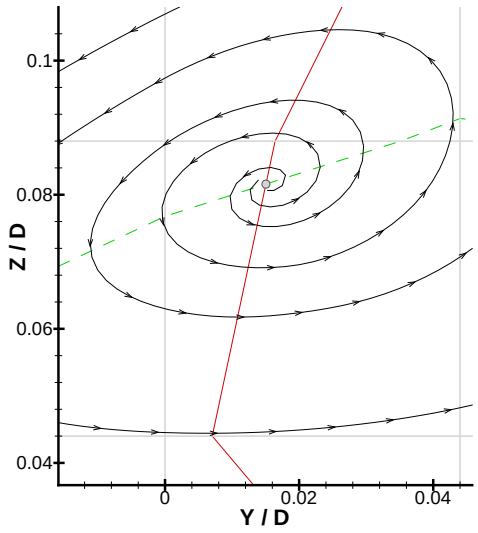

Figure 3.5: Critical Point Identification - Focus Source

Table 3.1: Critical Point Classification

	$r > q^2/4$	$r < 0$
$q < 0$	focus source	saddle source
$q = 0$	centre	divergence free saddle
$q > 0$	focus sink	saddle sink

ter flows. The basic technique was presented by Cabral and Leedom [44] and has not been substantially altered by subsequent investigators. The end result is essentially a high density streamline plot without the issue of missing features caused by the streamline placement.

The process begins by combining a vector field, defined on a rectangular grid (Figure 3.6b), with an input image of the same resolution as the grid (Figure 3.6a). Each pixel is visited sequentially and a streamline of a given length is integrated forwards and backwards from the vector field. The intensity of that pixel is then assigned the mean intensity of the pixels lying under that streamline and the process is repeated at the next pixel. As the calculation progresses, pixels on the same streamline are assigned similar intensities, resulting in the filtering, or smearing, of the input image along the streamlines of the vector field. The technique can be used to deform any input image along any vector field and is therefore a popular tool in computer graphics. A white-noise input image is favoured in fluid dynamics as it results in an output image that is dominated by the vector data. Figure 3.6 illustrates the input and output of the LIC technique as applied to a solid-body-rotation vector field.

The implementation employed in this study used interpolation to allow the resolution of the images to be independent of that of the vector field. An in-depth discussion of the implemen-

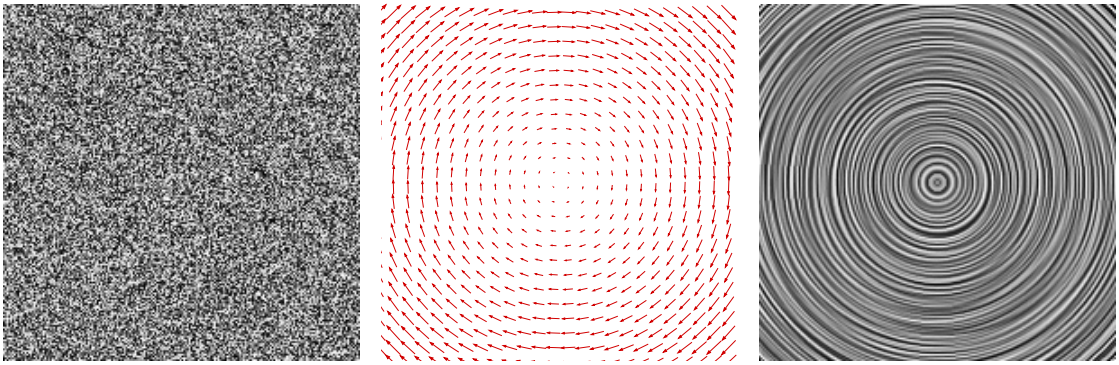

(a) Input Image (b) Vector Field (c) Output Image

Figure 3.6: Line Integral Convolution I/O

tation can be found in [45]. Figure 3.7 shows the results of an investigation into the effect of over-sampling a vector field to produce higher resolution images. The input dataset remained constant whilst the level of oversampling was varied from 2 to 20. Whilst the size of the output image is dependent on the level of oversampling, for clarity all images are shown at the same physical size. Table 3.2 summarises the position of the lower-right vortex as derived from inspection of Figure 3.7 and also includes the position, determined using critical point analysis of the original dataset, for comparison.

Table 3.2: Vortex Position Variation

Over-Sampling	Y/D-Pos.	Z/D-Pos.
0 (Critical Point Analysis)	0.113	0.174
2	0.109	0.162
5	0.114	0.176
10	0.112	0.178
20	0.114	0.176

Both Table 3.2 and Figure 3.7 show that over-sampling the grid up to 20 times has minimal negative effect on the LIC images and serves only to improve their resolution and descriptive quality.

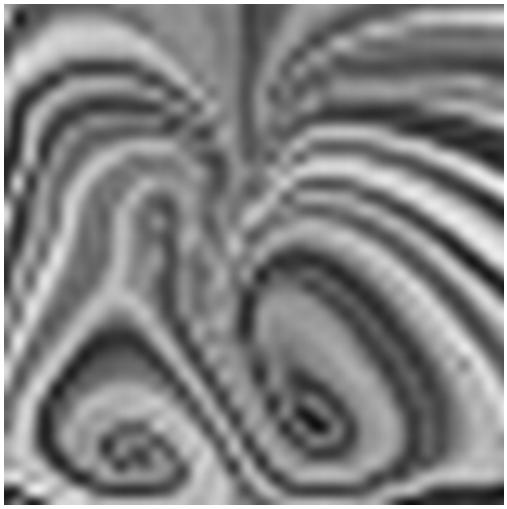

(a) 2× Over-sampled

(b) 5× Over-sampled

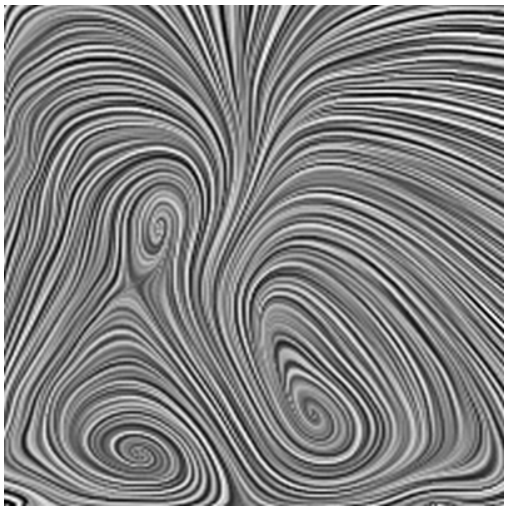

(c) 10× Over-sampled

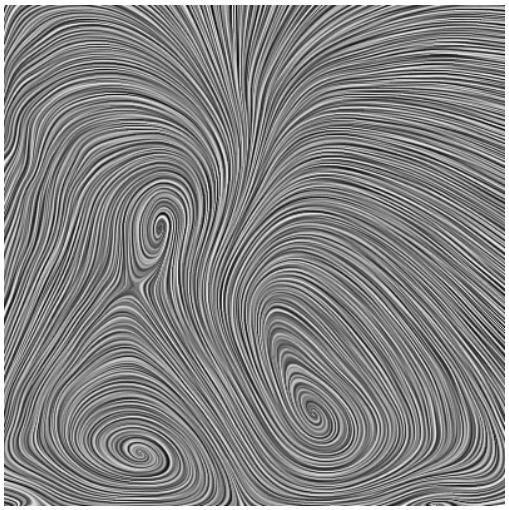

(d) 20× Over-sampled

Figure 3.7: Sensitivity of LIC to Over-Sampled Grids

4 Computational Method

Just as with the experimental work, this research featured two distinct computational studies. In this case, however, the method used in each study was identical, only the geometry was varied. Two complementary simulations were carried out for each experimental test. One simulation was of the wind tunnel, with a wheel and support sting, and one prediction was of the wheel flow without the sting. The detailed flow visualisation possible with a computational model was used to expand on the experimental data and also give an insight into an experimentally-challenging configuration.

The computational work aimed to reflect the state-of-the-art in racecar aerodynamic practice, just as the experimental work had done primarily through its choice of test components. In the computational case it was the prevalent industrial methodology and best practices for fluid flow simulation that were adopted. This dictated the use of several techniques including the finite-volume solution method, unstructured meshes and steady-state Reynolds Averaged Navier-Stokes (RANS) based turbulence modelling. The application of these techniques within this phase will be addressed individually in the following sections.

All computational work was carried out using version 6 of the Fluent CFD software suite. Setup sheets for each model, detailing all solver parameters can be found in Appendix C.

4.1 Mesh Generation

Spatial discretisation (mesh generation) dominates the initial phase of any computational fluid dynamics simulation. The number of cells generated, their concentration and quality determine the computational resources required, the time taken to solution and the accuracy of the result. An upper limit of 1.5×10^6 cells was imposed, partially limited by the available computational resources and partially to reflect the industrial state-of-the-art. At the time that this phase of work was being conducted an industrial model of a complete racecar, utilising a central symmetry plane, used of the order of 6×10^6 cells. Using more than one quarter of this number of cells to model one wheel was not representative of, or acceptable in, industrial practice.

The mesh used in this study was based upon the three-dimensional CAD models used to manufacture the tested components. Apart from the removal of unnecessary features, such as internal details, the geometry remained unmodified. Therefore, all of the computational components were essentially geometrically identical to those tested experimentally. The only significant deviation from the experimental geometry was made at the tyre contact patch. Difficulty was

encountered in maintaining adequate cell quality when modelling the near line-contact between the rolling road and non-deformable tyre. Therefore, the wheel was slightly truncated by raising the ground plane by 0.003D. This increased the size of the contact patch to approximately 13° or 0.11D, and greatly reduced the cell skewness in this area.

It was not possible, however, to model the geometry of the wind tunnel due to the restriction on the total number of cells. The extent of the computational domain, and the position of the wheel therein, is shown in Figure 4.1.

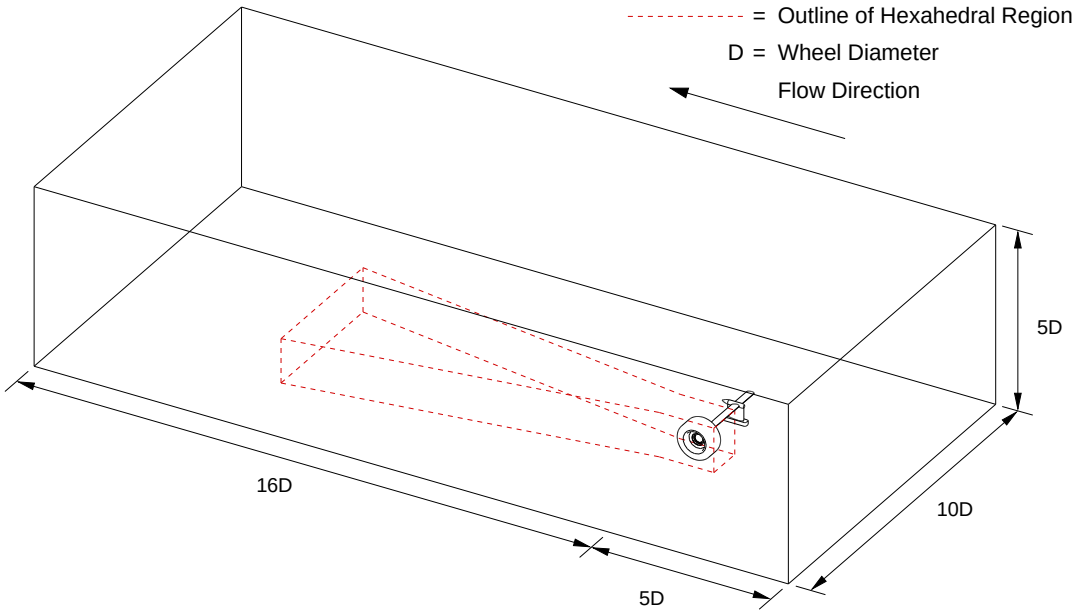

Figure 4.1: Schematic of Computational Domain

The cell number limitation, coupled with the complex geometry led to the adoption of a viscous-hybrid meshing strategy. This strategy resolves viscous dominated regions, such as boundary layers and wakes using regions of hexahedral or prismatic cells. The remainder of the solution domain, including geometrically complex regions, is resolved using tetrahedral cells. The strategy exploits the ability of prismatic and hexahedral cells to resolve flow gradients, such as in boundary layers, better than an equivalent number of tetrahedral cells. In this study, the tyre was embedded in a block of hexahedral cells, which was extended into the wake region and included the area investigated experimentally. The outline of the region of hexahedral cells is shown in Figure 4.1. The boundaries of the domain, and all components except the tyre were covered with a triangular surface mesh and the remaining volume, including the interior of the support sting, filled with tetrahedral cells. Pyramidal cells were not used to couple the tetrahedral and hexahedral zones as in this situation their cell quality was unacceptable. The two zones were coupled using a non-conformal interface, across which flow quantities were interpolated. The surface mesh on the test components is shown in Figure 4.2

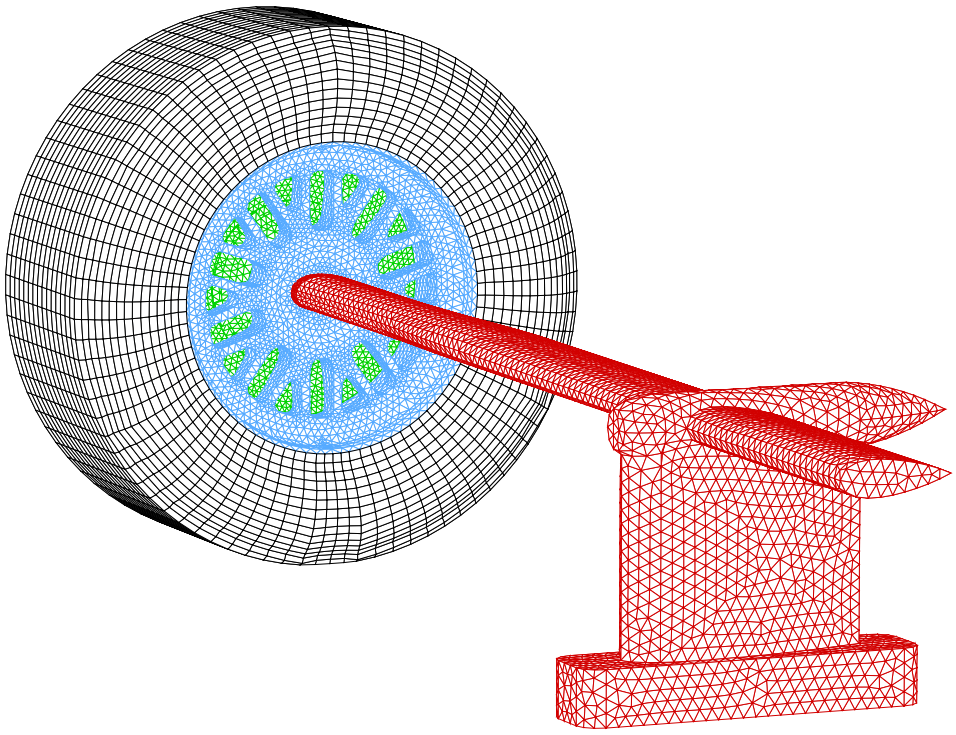

Figure 4.2: Wheel Assembly & Support Sting Surface Mesh

4.2 Boundary Conditions

The following is a summary of the boundary conditions, and required calibrations, used to simulate the experimental tests.

Wheel Assembly

All of the components of the wheel assembly, except the upright, were rotating during a test. However, the computational overhead of a moving or sliding mesh simulation to yield time-averaged results was excessive. Therefore all of the rotating surfaces were modelled using a moving wall boundary condition. This alone was insufficient in two main areas.

Firstly in the region surrounding the spokes and the brake rotor, the moving wall did not impart sufficient momentum to the flow. In resolution, the fluid contained within the hub spokes and the brake disc were separated from the domain, and the resulting zones were given the same angular velocity as the wheel. This approach was reported by Lewis and Postle [46] and recommended by Bienz et al. [47] in their respective simulations of an isolated Formula One wheel and brake cooling.

The second issue concerned the off-surface separation described by Fackrell [12]. Initial tests found that the motion of a smooth wall was insufficient to capture off-surface separation. Con-

sequently flow separation was predicted much further downstream than had been reported in the literature. The thin annulus of fluid that Fackrell found to rotate with the wheel was induced in the computational models by setting the surface roughness parameter of the tyre to be non-zero whilst leaving the motion unchanged. This was found to improve the separation prediction at negligible computational expense.

Support Sting

The interior volume mesh of the support sting allowed the sting to be removed from the solution without the need to generate a separate mesh. When the sting was present its surface was represented by a conventional wall boundary condition. The sting was removed from the domain by switching the surface to an interior condition, allowing the flow to pass through it.

Domain Boundaries

The boundary conditions of the six outer faces of the domain, shown in Figure 4.1, were chosen to approximate the wind tunnel. The ground plane was represented by a smooth wall moving at the freestream velocity. A pressure outlet condition, at atmospheric pressure, was applied to the rearmost face. The flow was introduced to the domain through the remaining four faces using a velocity inlet condition with a uniform velocity and specified turbulence level.

4.3 Solution

All of the RANS turbulence models available in FLUENT were tested in the initial stages of this study, before settling upon the standard $k-\omega$ model for continued use. Non-equilibrium wall functions, sensitised to pressure gradients, were used to resolve the near-wall regions. Appropriate first cell heights were applied in the mesh generation phase to ensure wall y+ values suitable for this approach. Wheel drag and lift coefficients (based on projected frontal area) were monitored throughout the simulations, alongside the mass-flow-rate through the spokes of the hub. These monitors were used as convergence criteria, with the simulation deemed to be converged when all three values were steady to at least three significant figures for a minimum of 100 iterations. Figure 4.3 illustrates a typical convergence history for these monitors showing that over the last 500 iterations of a simulation the normalised lift and drag forces are stable to within ± 0.5 % of their mean values. The mass-flow-rate was less stable but remained within 3.5 % of its mean value over the 500 iteration period.

The convergence histories of the cell residuals, corresponding to the force data in Figure 4.3, are shown in Figure 4.4. In most cases convergence was achieved within three thousand iterations, but when required, convergence was accelerated by solving the initial period of simulation using stable, first-order differencing schemes before moving to second-order accurate schemes, and the pressure interpolation scheme, PRESTO! (PREssure STaggering Option).

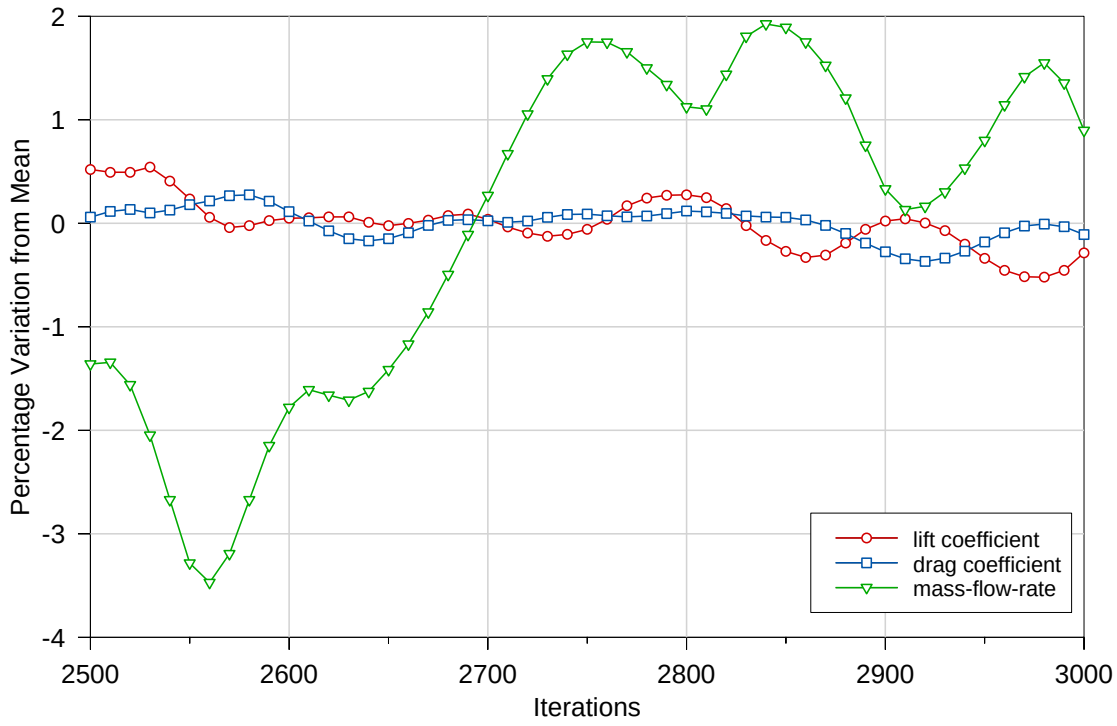

Figure 4.3: Convergence History - Normalised Monitors

The converged solutions with support stings were used as the starting point for the models without stings. One thousand further iterations were necessary to achieve convergence following the boundary condition alterations to remove the sting.

4.4 Post-Processing

In addition to the post processing described in Section 3.5, contour plots were used to illustrate the differences between simulated and observed values. This was acheived by plotting deltas, the experimental data subtracted from the computational data, visualised as contours. In this way a positive contour indicated over-prediction by the simulation and vice-versa.

Experimental and computational data were also extracted from the horizontal and vertical centrelines of the planes of interest, as shown in Figure 4.5, and plotted together as line graphs. These had the dual purpose of illustrating both the profile of the flow and highlighting the areas of difference between the two datasets. The complete set of velocity profiles is included for both phases in Appendix F.

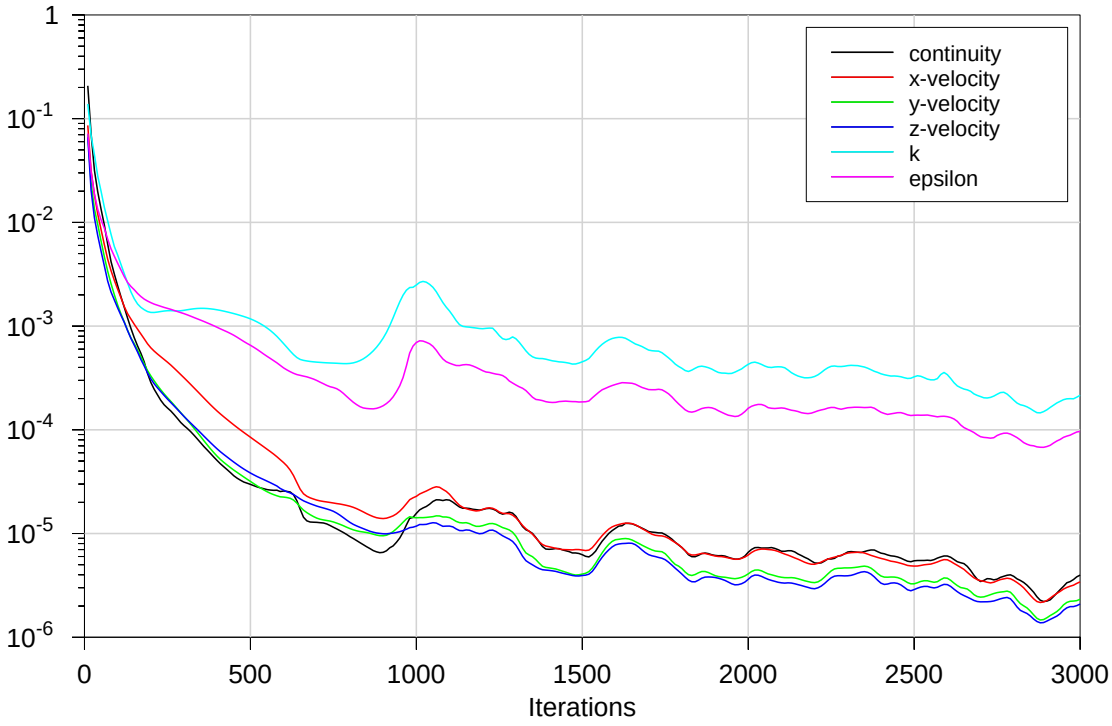

Figure 4.4: Convergence History - Scaled Residuals

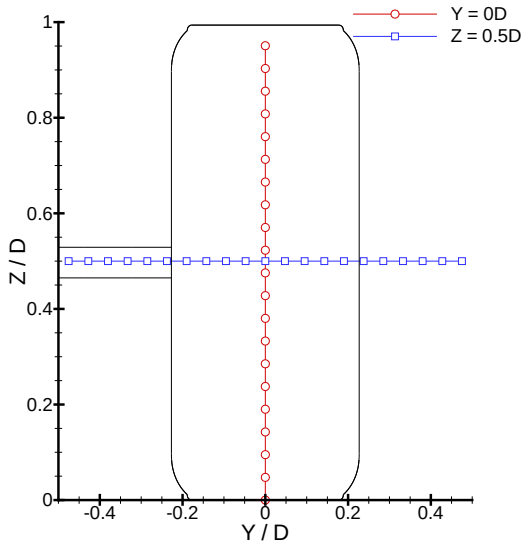

Figure 4.5: Position of Points Extracted for Line Graphs

5 Phase One – Champ Car

5.1 Introduction

This phase was undertaken to determine the efficacy of the experimental and computational methods presented in the previous chapters. A reduced experimental programme, where a single wheel and support sting were tested was completed and is detailed in the following section. The results of this investigation are presented, used as validation for the computational model and compared with previous work by other authors. The effect of the presence of the support sting, as predicted by the computational model, and the impact of this work upon the second phase is also discussed.

5.2 Experimental Details

This section will complete the experimental method outlined in Chapter 3, detailing the test components, wind tunnel and measurement planes used in this phase. A summary of the test settings can be found in Appendix B.

Test Components

The support sting and 40 %-scale wheel used in this initial phase were manufactured by Reynard Motorsport as part of the aerodynamic development of their 2002 Champ Car chassis. The wheel assembly did not, in this case, include an upright, but in other respects was as described in Chapter 3. The profile of the non-deformable, carbon-fibre tyre is shown in the cross-section of the wheel in Figure 5.1. The figure also illustrates the cavity left by the upright and the blockage presented by the brake rotor to the flow through the spokes. The spoke pattern of the hub, a model of a BBS racing hub, is shown in the right-hand sketch of Figure 5.1.

Wind Tunnel

All testing was carried out in the RMCS Open-Jet Wind Tunnel (OJWT) at a constant freestream velocity of 20 ms^{-1}, yielding a test Reynolds number of 3.7×10^5, based on wheel diameter. The 40 %-scale wheel provided a blockage of 2.6 % based on the ratio of the projected frontal areas of the wheel and wind-tunnel nozzle.

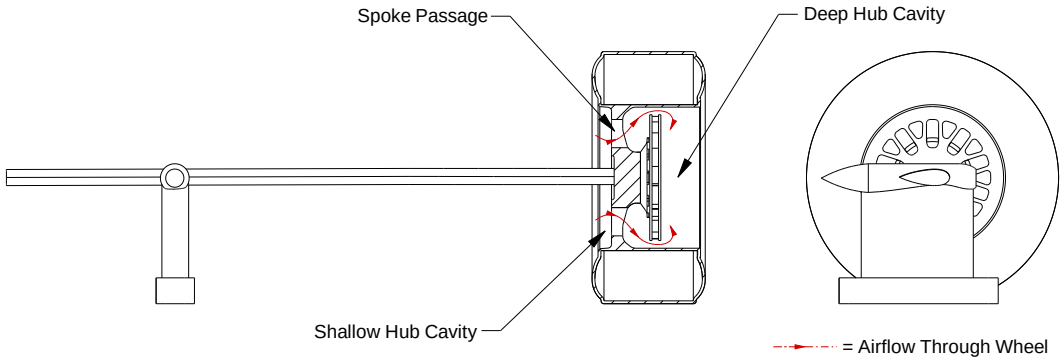

Figure 5.1: Champ Car Wheel Assembly & Support Sting

This tunnel had no cooling provision and as such the air and road temperatures could not be maintained. The air temperature was monitored throughout the tests and found to rise by not more than 5°C per run. This was the second and final deviation from the experimental method of Chapter 3.

Measurement Planes

Four measurement planes, of the type described in Chapter 3 were recorded. The 250 mm $\times$ 250 mm planes were located 0.54, 0.60, 0.69 and 0.88 wheel diameters downstream of the centre of the wheel and contained 441 equi-spaced points. The maximum number of samples per point was 2500 and the maximum sample time was 15 seconds. The measured velocity components were transformed into the tunnel frame-of-reference using the procedure outlined in Appendix D.

5.3 Computational Details

The computational section of this phase proceeded as detailed in Chapter 4. The baseline model comprised 0.9 million cells which were locally solution-adapted in an attempt to improve experimental correlation. An additional 300,000 hexahedral cells were added to the grid specifically in the area of the tyre contact patch (front and rear) and surrounding the volume measured experimentally. The contact patch adaptions were particularly effective at capturing the flow in this region, however the additional cells in the near-wake had much less impact on the solution. It was not possible to adapt the grid further without exceeding the imposed upper cell limit and as such grid convergence could not be determined.

The enlarged grid required 50 CPU hours on 5 nodes of an SGI Origin2000 26-processor machine to yield a converged solution for each of the sting and no-sting cases. The u, v and w velocity components in four planes equivalent to those measured experimentally, were exported

to be used in verification and validation. The surface pressure coefficients on the tyre circumferential centreline and force coefficients were also exported for this purpose. A summary of the model and solver settings are tabulated in Appendix C.

5.4 Results & Analysis

In this section the LDA data will be presented alongside both the computational model of the experiment and the prediction of the flow without a support sting. Comparison of these three datasets will provide an insight into the effect of the support sting whilst the computational models will be used to provide further insight into the notable flow features.

The data were post-processed as described in Chapter 3 to provide the clearest visualisation of the flowfield. In Figure 5.2 the shape and extent of the velocity deficit is presented as contours of mean u velocity. Figure 5.5 reveals the main flow structures using in-plane (v–w) velocity vectors. The line integral convolution (LIC) technique, discussed in Chapter 3, was used to generate the images shown in Figure 5.6. This type of image offers greatly improved visualisation of the layout and extent of any flow structures at the expense of the magnitude and directional information provided by the vectors. Figure 5.7 illustrates the structure and distribution of turbulence in the streamwise direction as visualised by contour plots of Ti_u. In all cases the velocity and distance data were non-dimensionalised by the freestream velocity, u_∞, and wheel diameter D, respectively.

5.4.1 Experimental Data

This subsection focuses on the main features of the experimental data, introducing the main points of interest which will subsequently form the basis of the verification and validation of the computational model. Error analysis of this experimental data can be found in Appendix E.

Mean Velocity Contours

Figure 5.2 shows that the near-wake is made up of a central region with approximately the same extent as the projected wheel profile, accompanied by two large ground lobes and two smaller upper lobes. These features are not symmetric about the $Y/D = 0$ centreline but are present in each measured plane. The wake of the support sting is also visible, although perhaps more clearly in the two plots furthest from the wheel. The shape of the wake is in agreement with the previous experimental work of Fackrell [12], Nigbur [35] and Purvis [26].

The measurement techniques used in those studies did not allow resolution of reversed flow. Therefore the regions of recirculating flow, present in each plane, have not been previously experimentally identified. The existence of these regions was expected, following consideration of the recirculation zones prevalent in bluff-body wakes. However, the extension of this region

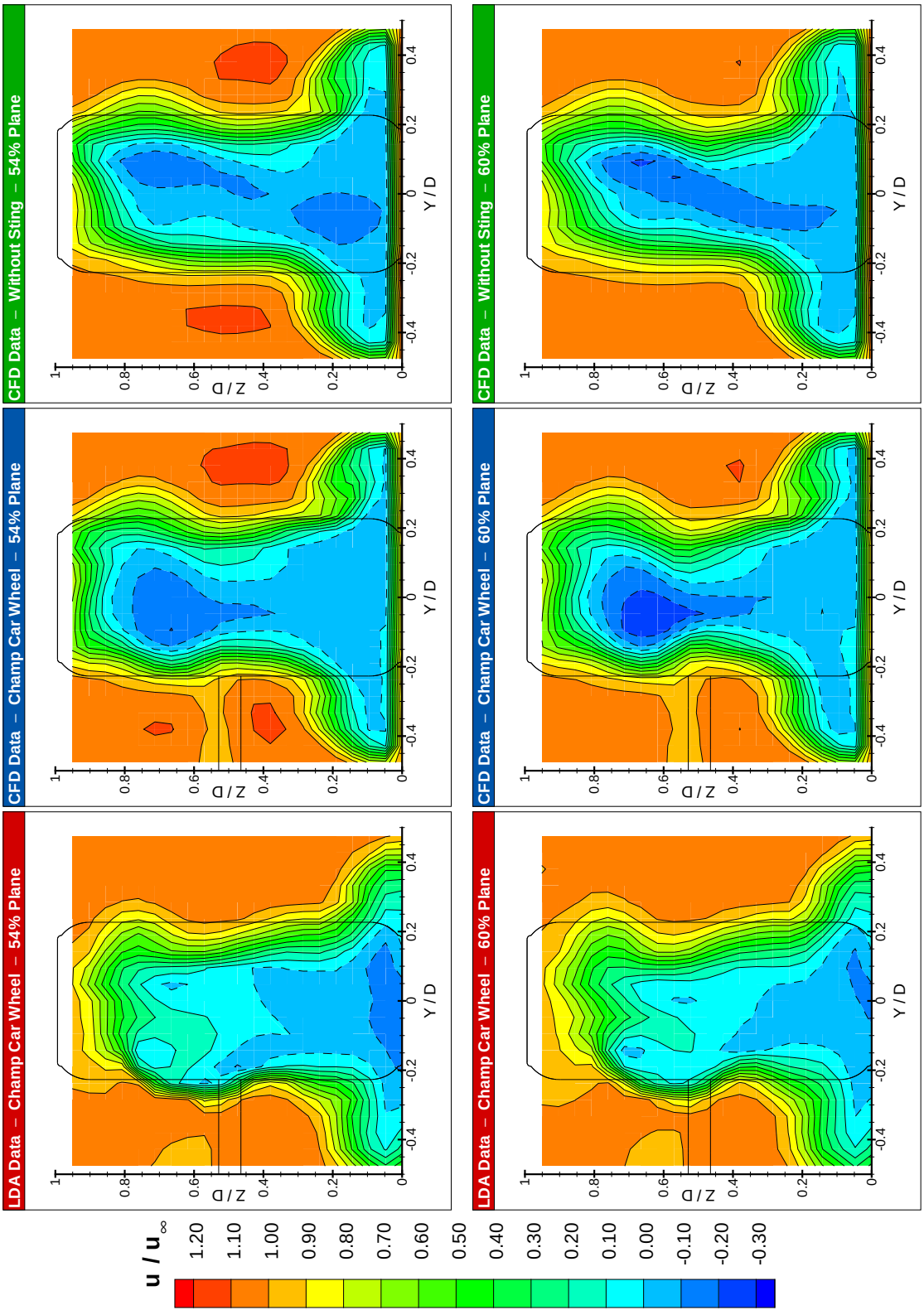

Figure 5.2: Comparison of LDA & CFD Contours of Mean u-Velocity
(negative regions bounded by dashed lines)

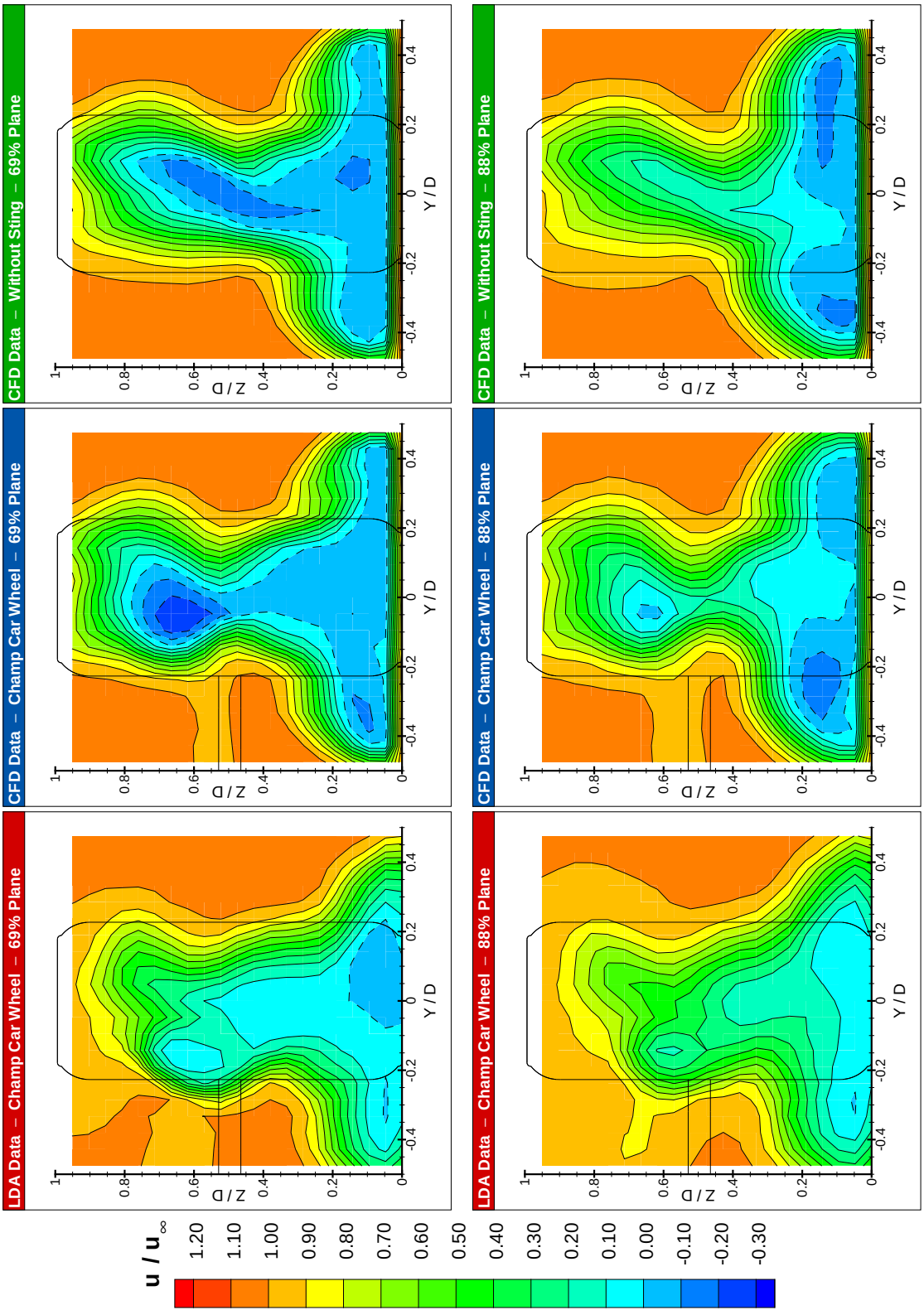

Figure 5.2: (cont.) Comparison of LDA & CFD Contours of Mean u-Velocity (negative regions bounded by dashed lines)

outside the projected profile of the wheel is more unusual. From the experimental data it is not possible to identify the mechanism by which the wake can proceed upstream against the freestream flow out of the lee of the wheel. However, the same behaviour was also observed by the author in a similar investigation using a different wheel geometry [25].

In-Plane Mean Velocity Data

The asymmetry noted in the u contours, Figure 5.2, is also visible in the plots of Figure 5.5, and perhaps more clearly in Figure 5.6. Figure 5.3 simplifies the picture further by presenting only the centres of the trailing vortices, foci in 2D, as identified by critical point analysis. The most obvious asymmetry is the absence of the vortex, expected to be shed from the upper-right quadrant of the wheel. The other main asymmetry is in the location of the foci, the sting side structures are much closer to the projected profile of the wheel than those on the opposite side. However, in all planes the vortex centres remained within, or aligned with, the wheel profile.

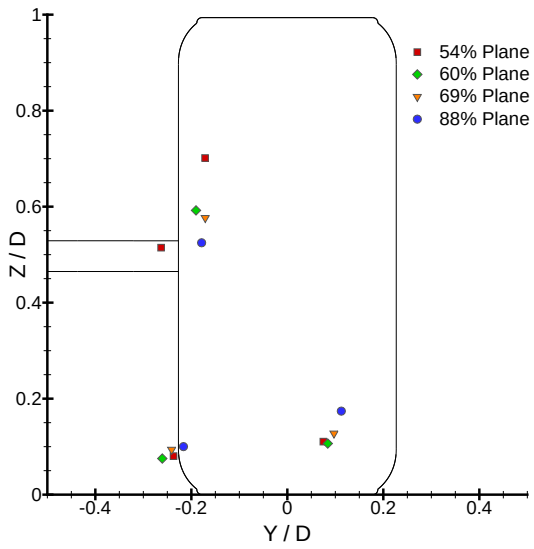

Figure 5.3: Summary of Vortex Centre Positions

From Figure 5.3 it can also be seen that the individual vortex centres do not migrate far. Their axes are oriented along the streamwise axes and do not appear to spread laterally over the near-wake. The height of the upper vortex is plotted against streamwise position in Figure 5.4 to illustrate the inclination of its axis to the horizontal. The downward trend corresponds to the region of down-wash in this area of the wake, but also confirms that this structure has its origins in the upper quadrant of the wheel.

Figure 5.3 also shows that the 54 % plane contained four foci, one of which was behind the projected profile of the support strut. Its location suggests that this small vortex, visible in

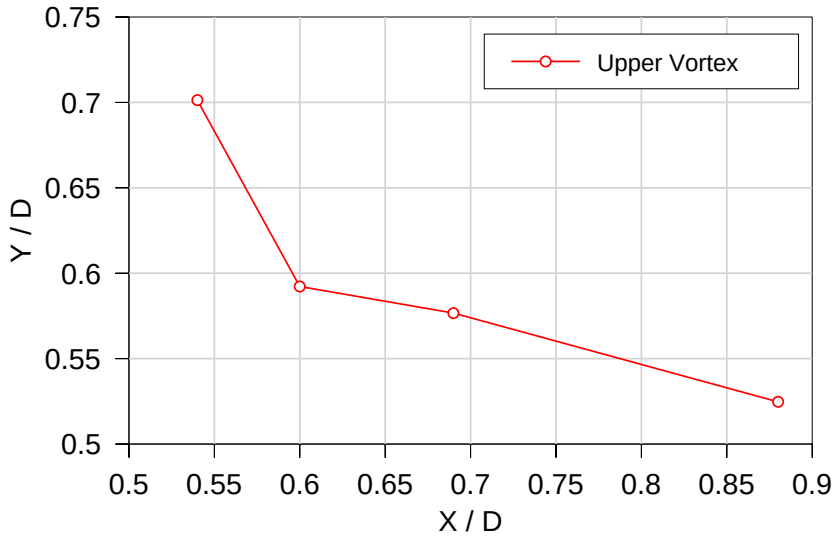

Figure 5.4: Convection of the Upper Vortex

Figure 5.6, could be shed from the junction between the wheel and sting although this cannot be determined from the experimental data.

Inspection of Figures 5.5 and 5.6 also revealed that the down-wash region was asymmetric, shifted away from the wheel centreline towards the sting, and that large regions of up-wash were present either side of the wheel including an almost purely vertical region behind the sting. The latter point explains why the wake of the sting in Figure 5.2 was observed to rise in the two planes furthest downstream.

Streamwise Turbulence

The streamwise component of turbulence, Ti_u, is illustrated in Figure 5.7 using flooded contours. White is used to identify areas where $Ti_u > 0.3$ whilst retaining sufficient contour levels to describe the remainder of the data. In general the shape and extent of the Ti_u distribution corresponds, as expected, to that of the streamwise velocity, Figure 5.2. However, the most notable difference is the bisection of the central region by an area of reduced intensity, particularly visible in the 60 % plane.

The regions of high turbulence intensity $(Ti_u > 0.3)$ are located within the trailing-vortex cores, reversed flow regions or the wake shear layer. As the flow progresses downstream Ti_u increases in the lower vortices and reversed flow regions, whilst the shear layer and upper vortex reduce below 30 %.

The available experimental data cannot fully explain all of the features noted or their underlying mechanisms. It does, however, suggest several areas for investigation using the computational results.

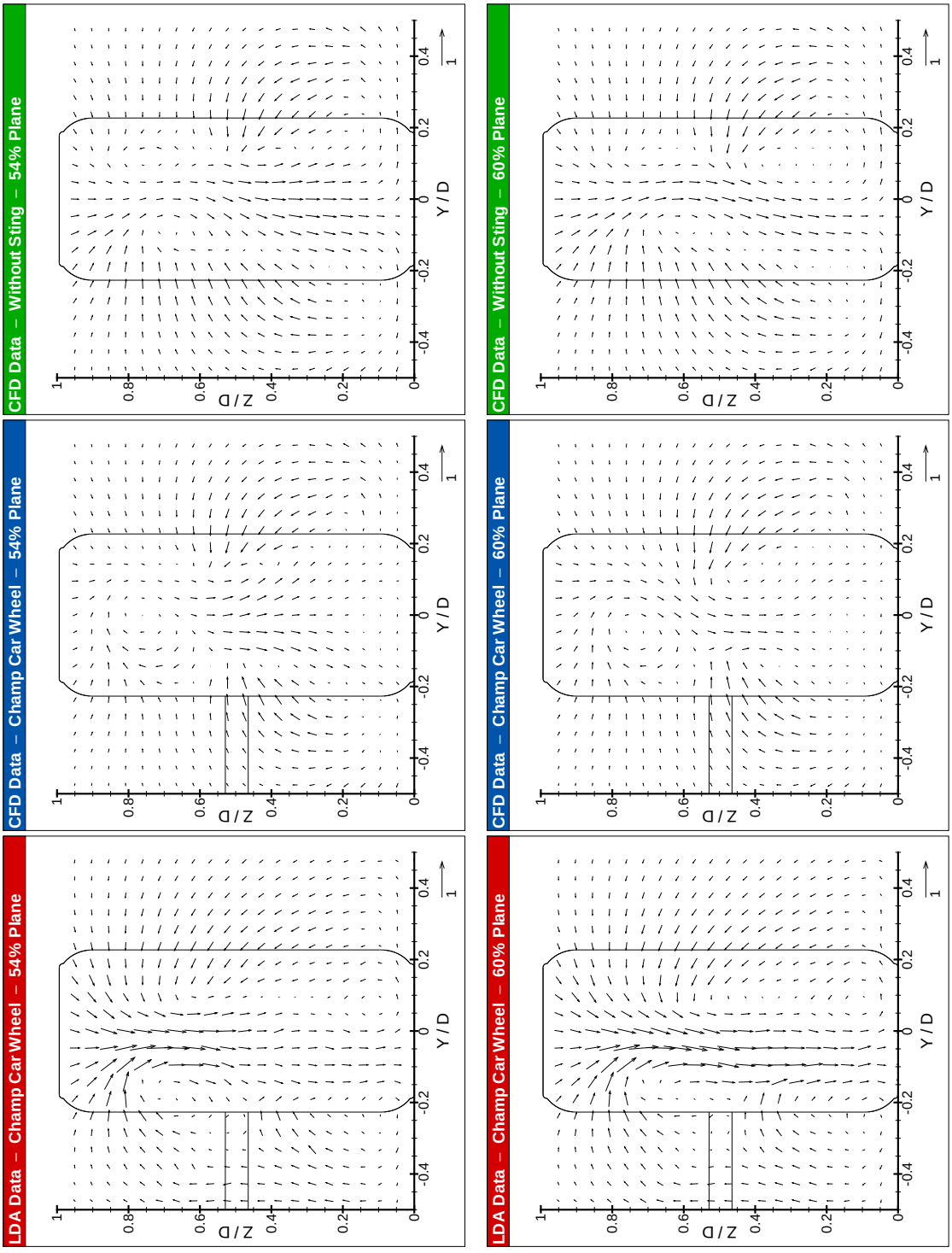

Figure 5.5: Comparison of LDA & CFD In-Plane (v-w) Vectors

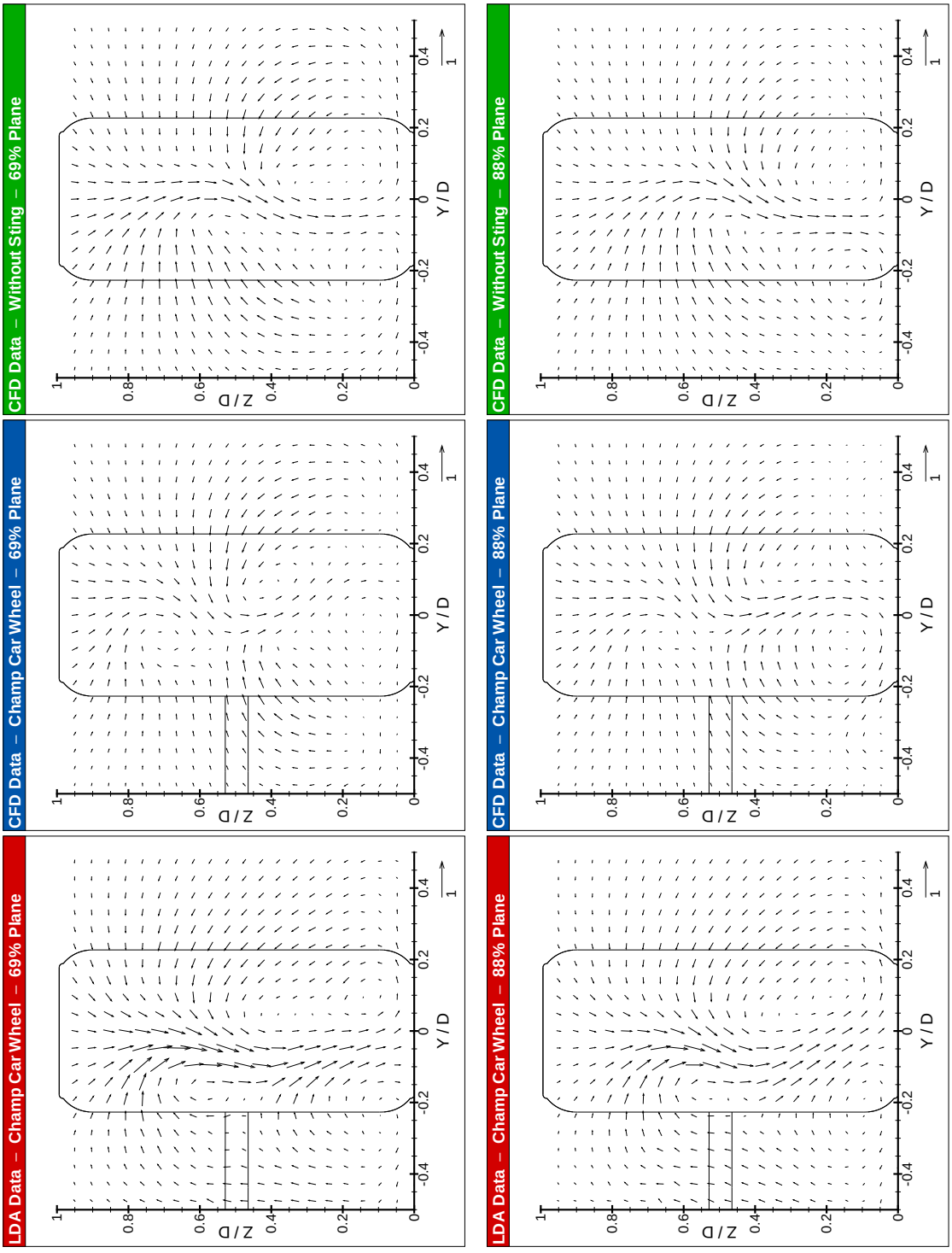

Figure 5.5: (cont.) Comparison of LDA & CFD In-Plane (v-w) Vectors

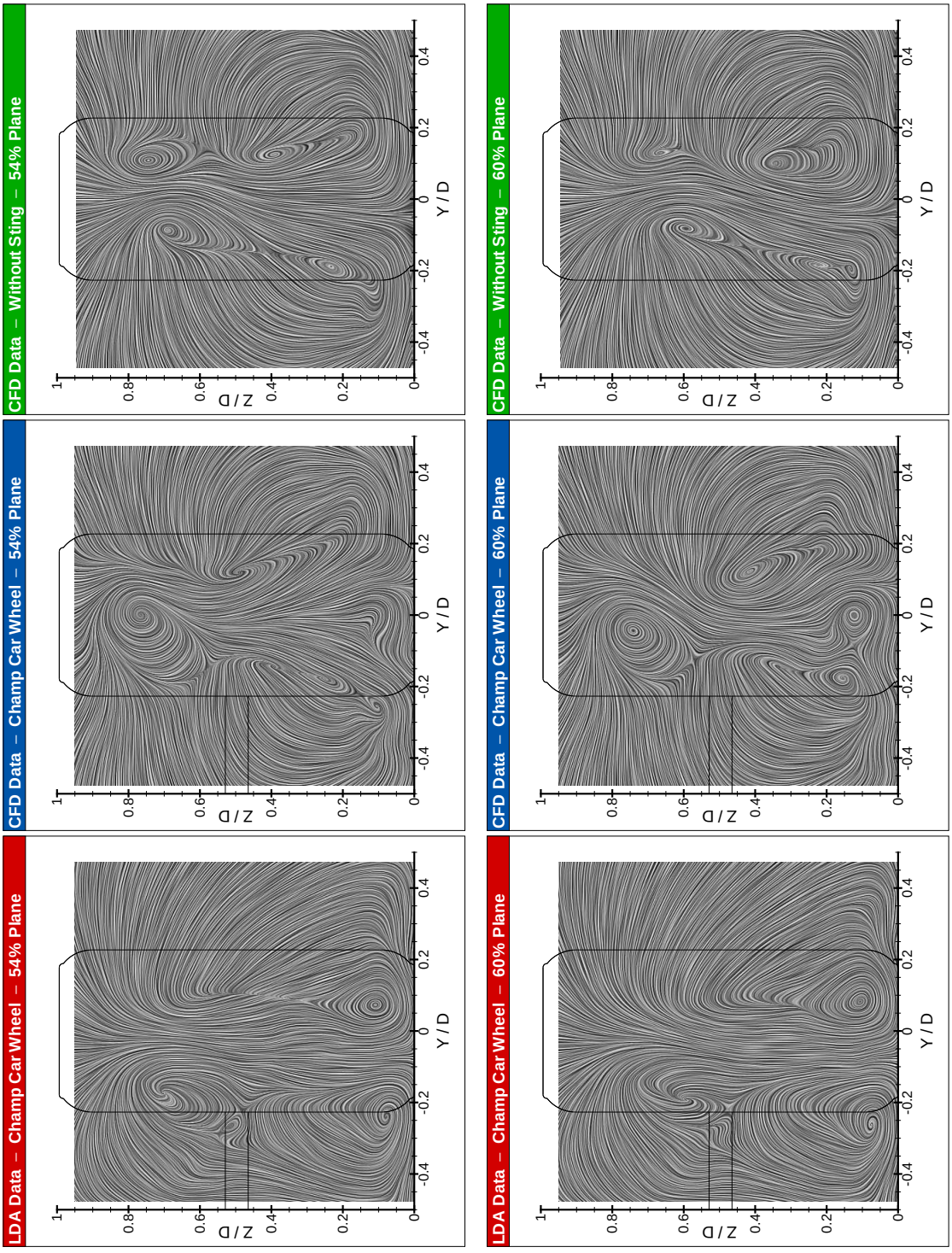

Figure 5.6: Comparison of LDA & CFD Line Integral Convolution Images

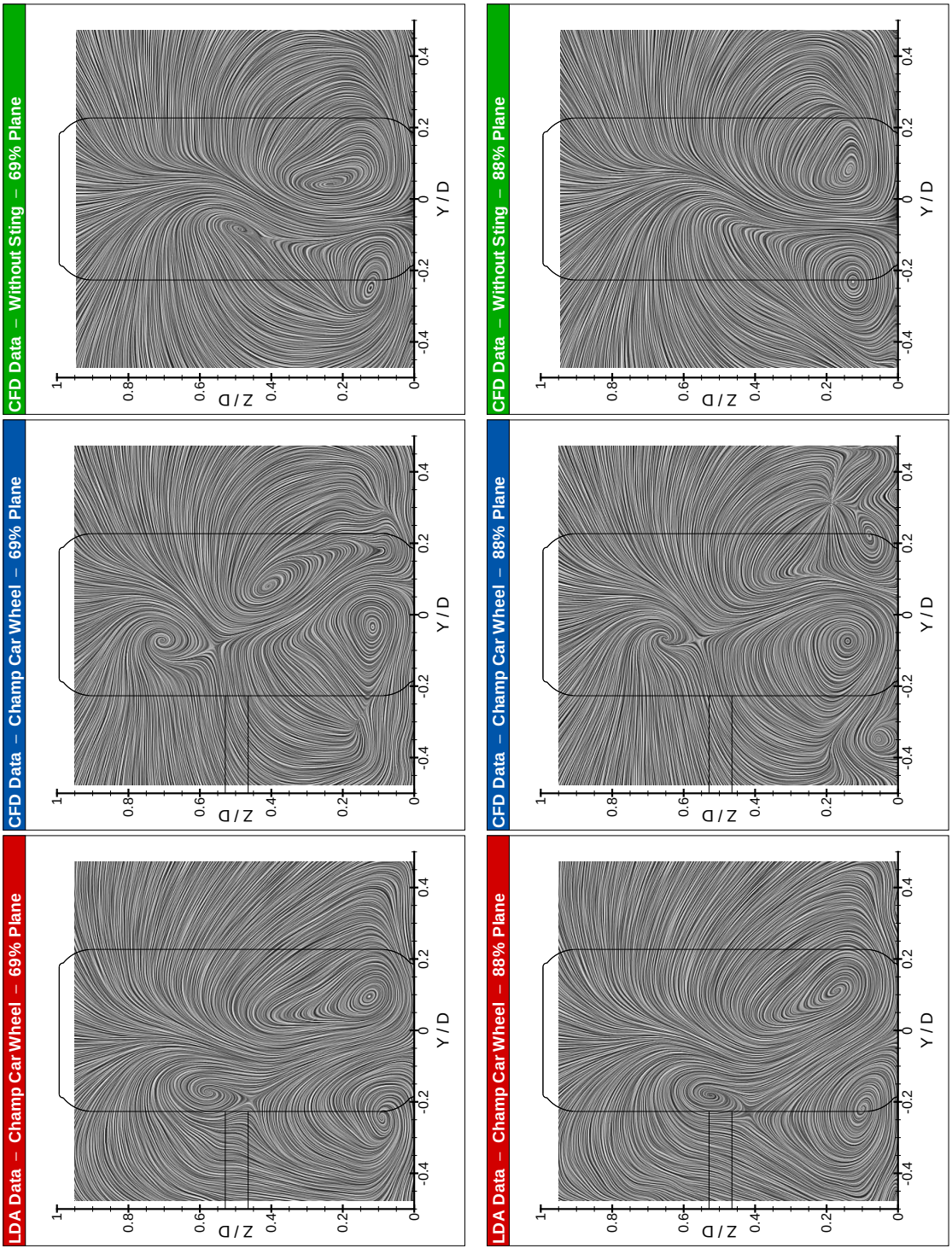

Figure 5.6: (cont.) Comparison of LDA & CFD Line Integral Convolution Images

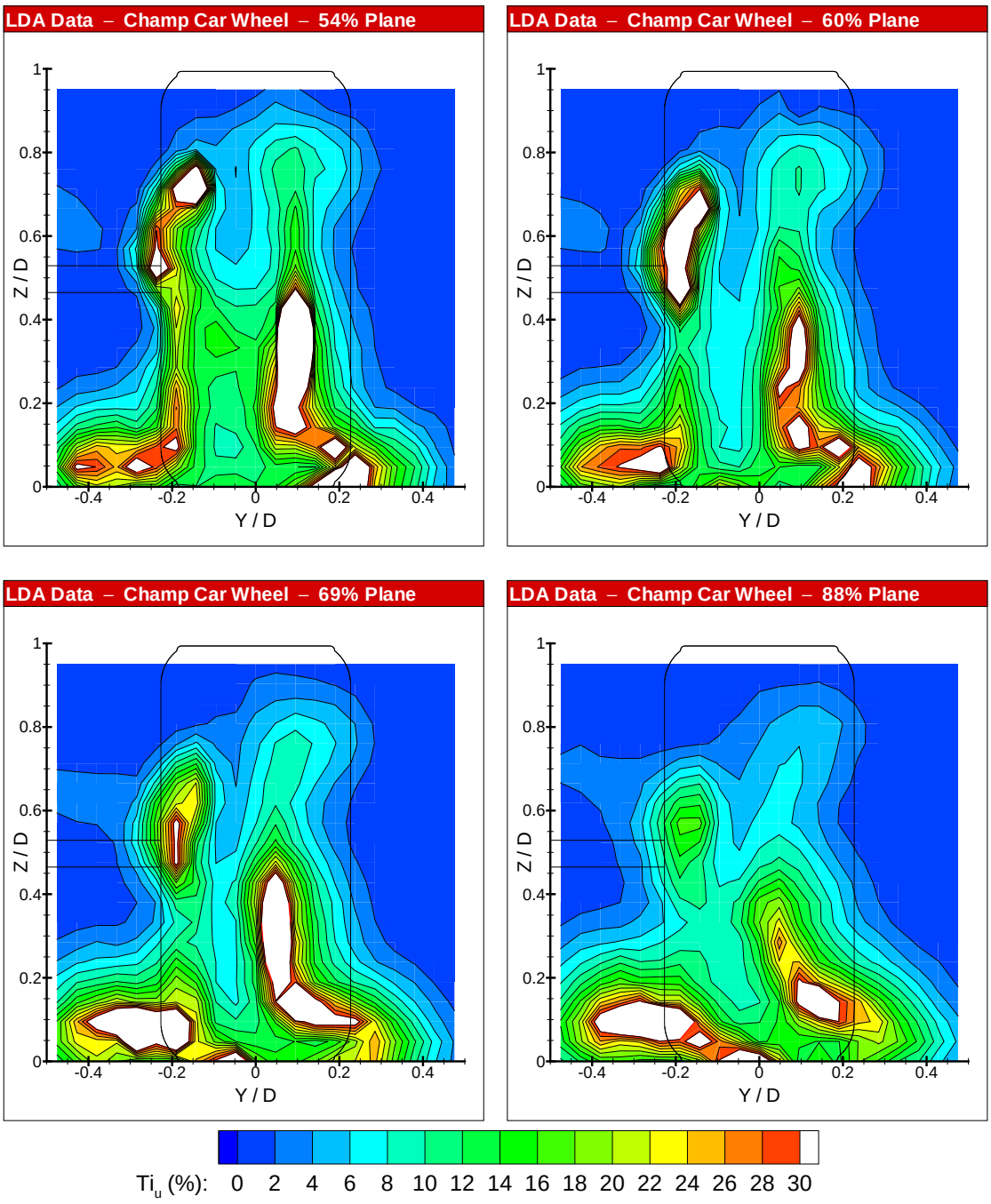

Figure 5.7: Streamwise Turbulence Distribution Ti_u

5.4.2 Verification & Validation

Whilst presenting the experimental data, Figures 5.2–5.6 also provided comparison with the results of the CFD simulation of the wheel and sting assembly.

Mean u-Velocity Contours

The overall shape of the wake in Figure 5.2 compares well with the experiment. Both the upper and lower lobes are captured as is the width in the central region. The horizontal and vertical centreline u-profiles in Figure 5.8 confirm that many of the flow features have been captured in addition to the general trends. The horizontal profile (Figure 5.8a) shows that the whilst the central region and shear layers have been well resolved the asymmetry, although present, is less pronounced than observed experimentally.

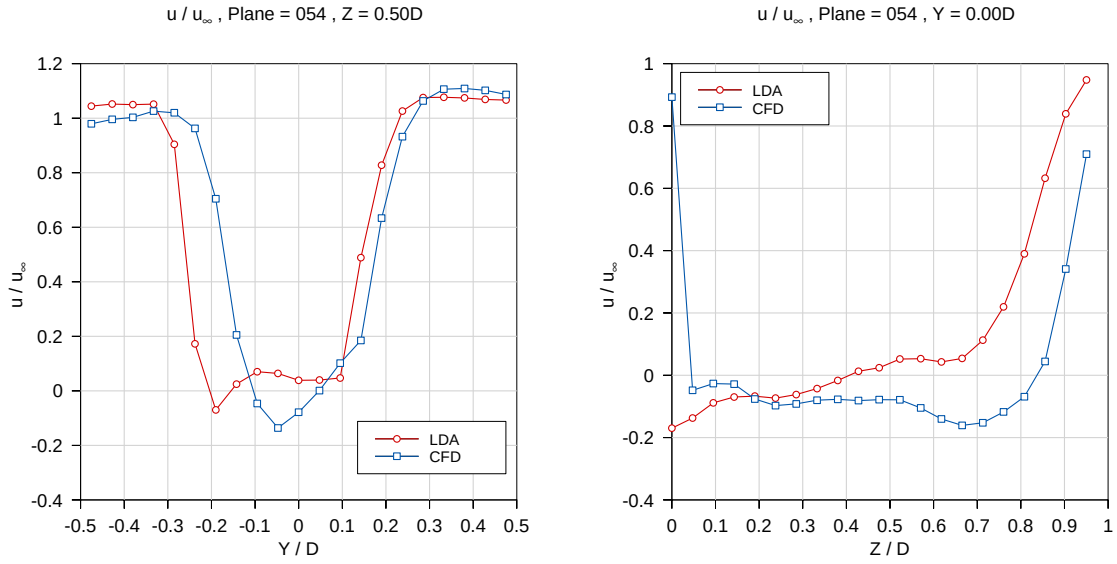

(a) Horizontal Centreline $(Z/D = 0.5)$

(b) Vertical Centreline $(Y/D = 0)$

Figure 5.8: Comparison of LDA & CFD Centreline u-Velocity Profiles - 54 % Plane with Sting

In the vertical profile (Figure 5.8b), the experimental data had almost recovered to the freestream value by the top of the measurement plane, whilst in the computational data, $u/u_\infty \approx 0.75$. This over-prediction of wake height can be clearly seen in each plane of Figure 5.2. The same profile graph also illustrates that the reversed flow region is over-predicted when $Z/D > 0.25$ and an under-prediction below that height. The similarity of the slope of the two lines as they recover to freestream suggests that the shear layers are of comparable thickness. Therefore it is the existence of reversed flow up to $Z/D \approx 0.85$ which appears to be the major factor in the over-prediction of wake height.

The features illustrated for the 54 % plane occur to a similar extent in all planes. Figure 5.9 shows a delta $(\mathrm{CFD} - \mathrm{LDA})$ plot for the 88 % plane where positive and negative values show

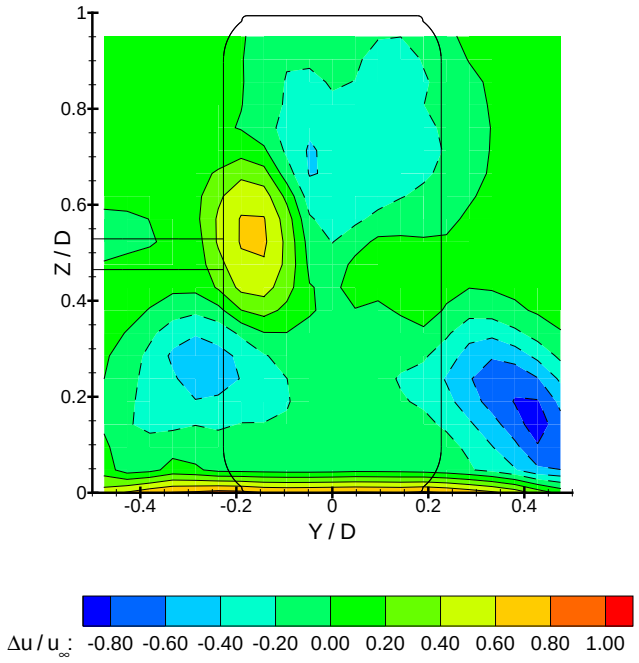

Figure 5.9: Δu - 88 % Plane $(\Delta = \text{CFD} - \text{LDA})$

over and under-prediction respectively. The figure shows:

- the increased wake height - represented by the upper negative region;
- a lack of asymmetry - represented by the positive region at half-height;
- enlarged reversed flow region - represented by the two lower negative regions.

From inspection it would appear that prediction of the extent and magnitude of reversed flow is the main discrepancy between the experimental and computational data. The CFD does, however, capture the extension of these regions beyond the projected wheel profile which was observed experimentally.

In-Plane Mean Velocity Data

The size, extent and sense of rotation of the near-wake vortex structures, including the left saddle-point, are all captured in the CFD results. Figure 5.10 again utilises the centreline velocity profiles to compare the computational and experimental results. The horizontal profiles in this figure show very similar trends over the full width of the measurement plane. The main deviation from the experimental results is in the region of $\text{Y}/\text{D} = -0.2$, which in the experimental data is the location of a saddle point. Although the saddle was captured by the CFD, it, along with the

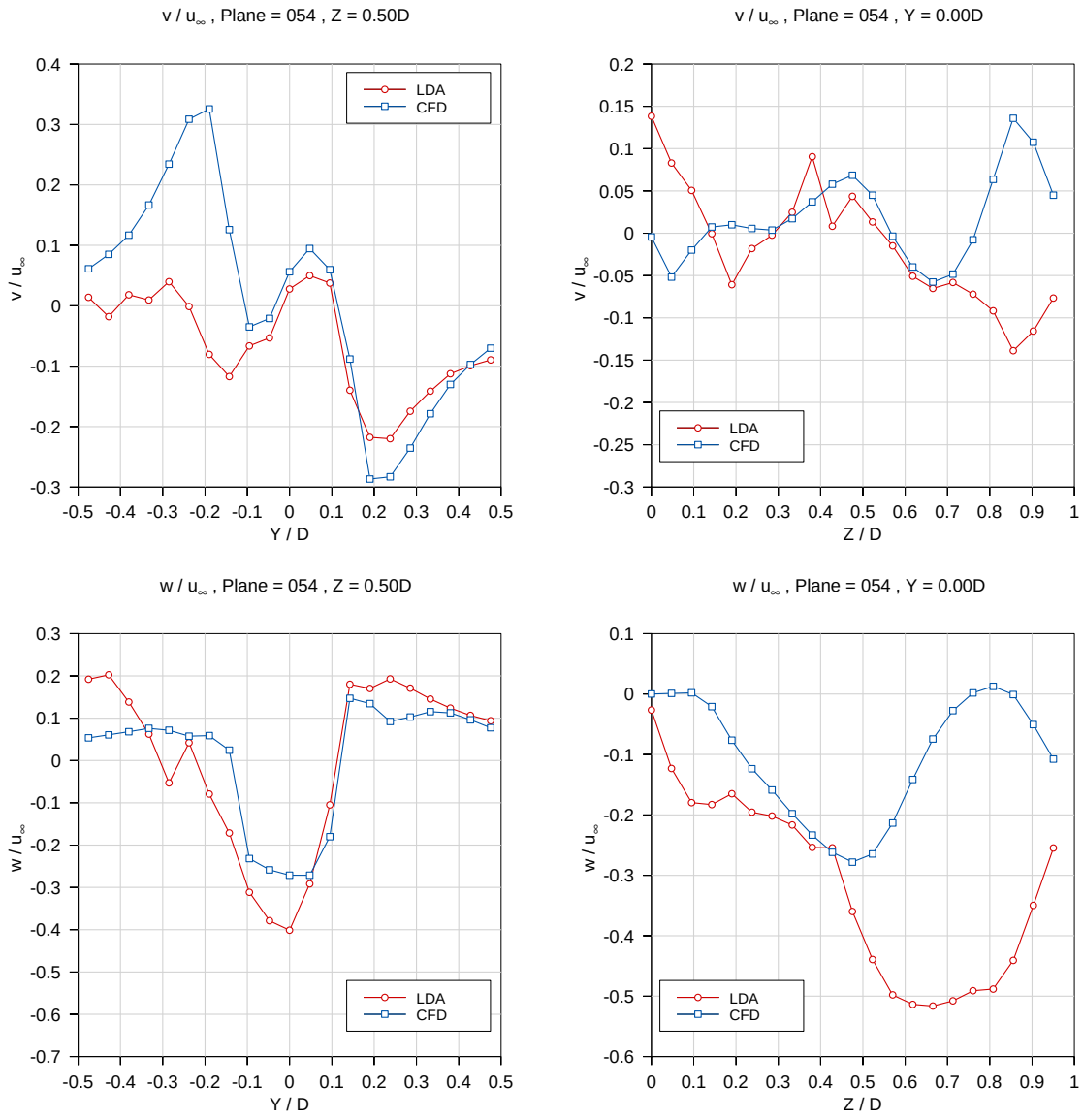

(a) Horizontal Centreline $(Z/D = 0.5)$

(b) Vertical Centreline $(Y/D = 0)$

Figure 5.10: Comparison of LDA & CFD Centreline In-Plane (v–w) Velocity Profiles - 54 % Plane with Sting

vortices, were consistently predicted higher than observed experimentally. Thus resulting in the deviation of the profiles as the computational saddle occurred above the centreline.

A similar effect can be observed in the vertical profiles of the same figure which exhibit a marked deviation above $(Z/D = 0.5)$. In this case inspection of Figure 5.6 shows that the upper vortex is predicted closer to the vertical centreline than observed. This has the joint effect of increasing v and reducing the down-wash (w) when compared with measured values.

Whilst the vortex centres remain within, or aligned with, the projected wheel profile in all planes, Figures 5.6 & 5.10, have shown that the convection of the structures and the absolute position of their centres is less well represented.

The main feature noted in the inspection of experimental v–w data was the lack of the vortex expected to be shed from the upper-right quadrant of the wheel. This phenomenon is correctly captured by the CFD and is shown clearly in the LIC plots of Figure 5.6. The CFD results do not predict the convection of the single upper vortex beyond the second plane. This reduces the asymmetry of the two final planes, a feature also noted in the u contours at these stations. However, the increasing skewness of the central down-wash region as it is convected downstream is well illustrated by the CFD.

Comparison of the LDA and CFD vector plots in Figure 5.5, and the profiles in Figure 5.10, show that the magnitudes of the v and w components are slightly under-predicted, especially in the down-wash region. This, combined with the diffusion of the upper vortex, explains why the wake of the sting rises less than experimentally observed.

Centreline Pressure Profile

Although no pressure data were recorded experimentally by the author, it was deemed appropriate to compare the predicted tyre surface pressures with the work of Hinson [20] in an attempt to understand further the mechanisms at work in the regions of interest. Hinson tested a model Formula One wheel, of similar geometry and level of detail to the one used in this work, at a comparable Reynolds number. The wheel housed several transducers which were used to resolve the surface pressures acting on the tyre during rotation. Figure 5.11 compares the circumferential pressure distribution on the tyre centreline $(Y/D = 0)$ predicted by the CFD model with that measured experimentally by Hinson.

The experimental and computational correlation in Figure 5.11 is excellent and serves to highlight several areas of interest, whilst being unable to provide a measure of the computational accuracy. Firstly, the pressure peaks immediately upstream and downstream of the contact patch (90°) are correctly predicted.

The second point of note is in the region of flow separation, $\theta \approx 265^\circ$. In both the experimental and computational data the flow tolerated only a short adverse pressure gradient and before separating just downstream of the top of the wheel. The plot does show that the base pressure

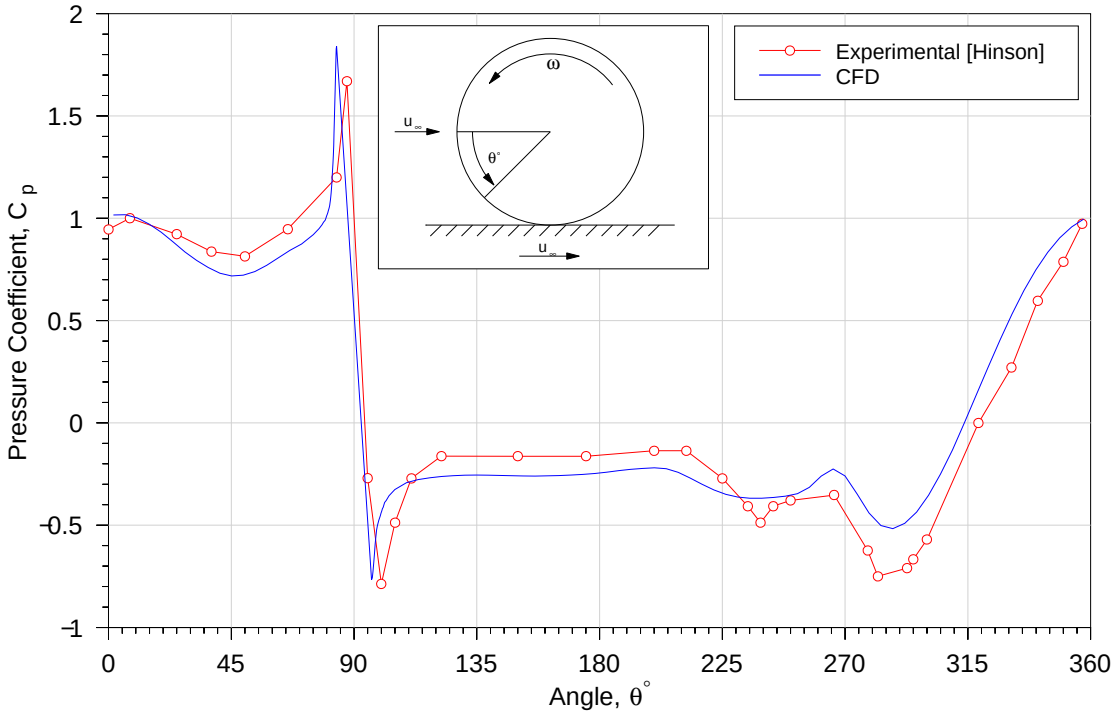

Figure 5.11: Circumferential Pressure Distribution on the Tyre Centreline

was predicted slightly low and that the suction peak upstream of separation, whilst present and in the correct location was attenuated.

This result confirms that contact patch grid adaption, wall functions and surface roughness can be successfully combined to simulate a tyre rotating in ground contact.

Wheel Drag Force

The predicted wheel drag force was compared with that measured experimentally and found to be under-predicted by 5.3 %. The measured drag coefficient, normalised by the projected frontal area, was 0.680 whilst the model predicted 0.644. This correlates with under-prediction by the simulation of the strength of the vortical structures and a taller but narrower wake.

5.4.3 Prediction of Sting Interference Effects

The two computational datasets in Figures 5.2−5.6 are compared in this subsection to determine the predicted effect of the support sting on the near-wake.

Mean u-Velocity Contours

Comparing the u contours of the two CFD simulations shows that the extent and shape of the wake in both cases is very similar, however the content is somewhat different. In the wake of the

unsupported wheel the lower lobes appear more symmetrical about the centreline $(Y/D = 0)$, whilst the bias in the upper central region has flipped to the right. Further evidence of this upper-right bias is the lack of the upper-left lobe, noted when the sting was present.

Reversed flow occurs in each measurement plane, and as noted experimentally, extends outside the projected profile of the wheel via the lower lobes. As previously mentioned, the flow in this area is more symmetrical without the sting and also more intense.

In-Plane Mean Velocity Data

Whilst the vectors in Figure 5.5 reveal that the magnitude and rotational sense of the components are comparable, the LIC plots of Figure 5.6 clearly illustrate the differences in the near-wake structures.

Most notable in the initial plane is the addition of an upper right vortex to form the contra-rotating pair expected, but not observed, in the presence of the sting. This new vortex does not convect into the second plane, whilst its partner is convected further than when the sting was present, into the third plane. The lower right structure appears initially to comprise two smaller vortices which attract as they convect down-stream and coalesce before the third plane.

The structures are of approximately the same size as in the presence of the sting although the skewness observed in the central down-wash region has reversed, correlating with the observation made during inspection of the u contours.

Centreline Pressure Profile

The removal of the support sting was found to have negligible effect on the centreline pressure profile and as such the data are omitted from Figure 5.11 for clarity.

Wheel Drag Force

A slight reduction in wheel drag force of 1.3 % was observed following the removal of the support sting.

5.4.4 CFD Flowfield Investigation

Several features were noted during the preceding sections that could not be explained using the experimental data alone. However, further investigation of the CFD data revealed a possible mechanism behind one of those features and also further sting interference effects.

Reversed Flow

It is the location of the regions of upstream flow in the near-wake of the wheel, rather than their existence, that is of interest. Inspection of both the experimental and computational data, Figure 5.2, noted that these regions extended beyond the projected profile of the wheel suggesting that they proceeded against the oncoming freestream. Further investigation was carried out using flow visualisation of the CFD results.

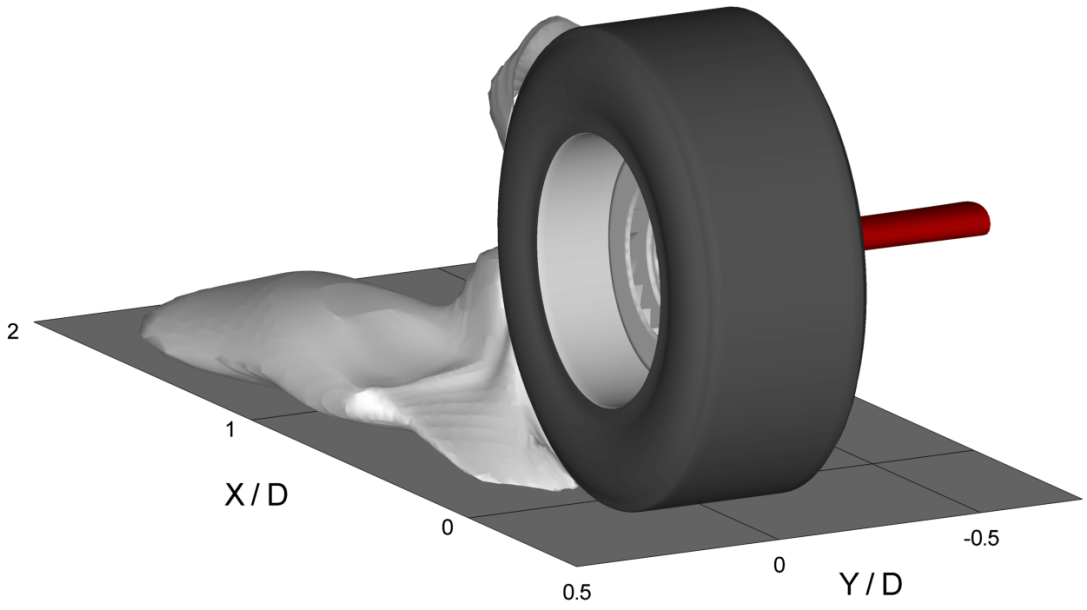

Figure 5.12: Velocity Iso-Surface $(u = 0)$ in the Near-Wake

Figure 5.12 illustrates, through an iso-surface of zero streamwise velocity, that the region of reversed flow originates just downstream of the contact patch. The geometry and motion ahead of the contact patch imparts significant lateral velocity to the fluid which subsequently deflects the freestream flow into the shape illustrated in the figure. In this way the fluid emanating from the contact patch modifies the effective shape of the wheel to include the iso-surface. Whilst the regions identified experimentally are outside the projected profile of the wheel, they are obviously within the projection of the iso-surface and as such shielded from the freestream.

Wheel Through-Flow

One of the convergence criteria for the computational models was the mass-flow-rate through the spokes of the wheel. It was noted that the sting had a significant effect on this flow, increasing the flow through the spokes by 58 % when present. A change of this magnitude could have a significant impact on the design of brake cooling. The distribution of the flow through the spokes is visualised in Figure 5.13 using contours of the axial flow component, v, on a plane just sting-side of the spokes. The interference effect of the sting appears to be to force fluid *into* the

wheel upstream of itself, in a region where fluid would be drawn *from* the wheel in its absence.

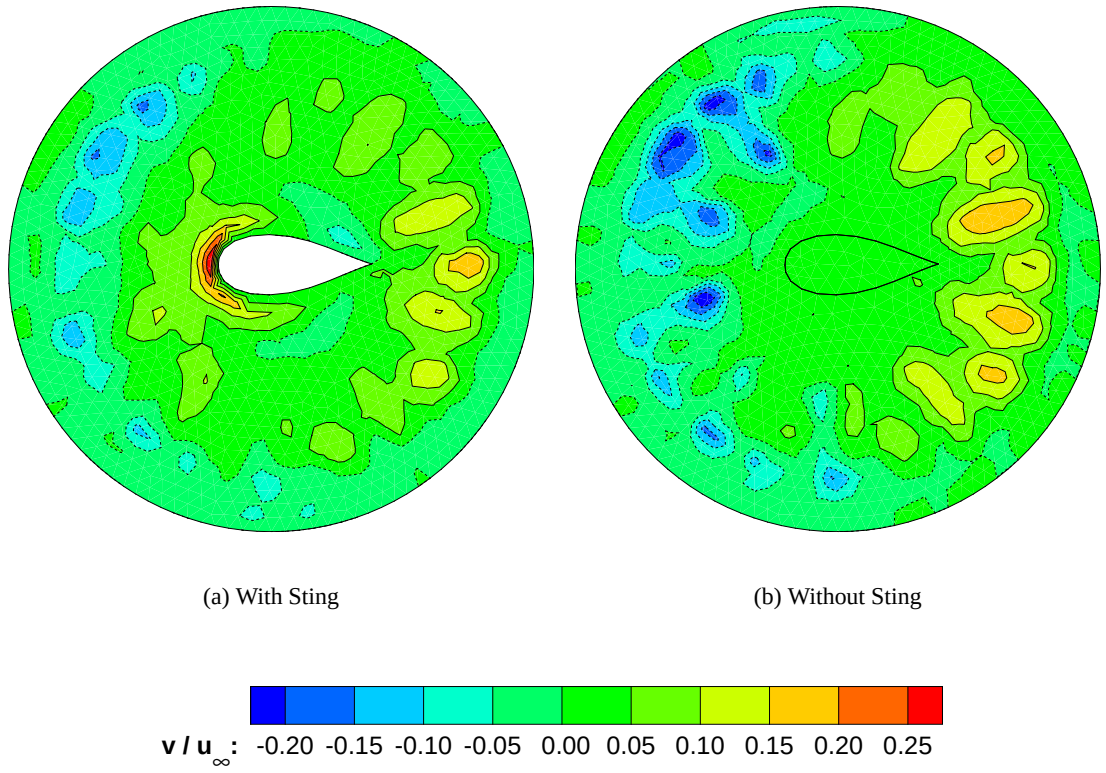

(a) With Sting (b) Without Sting

Figure 5.13: Axial Velocity (v) Contours on the Spoke-Face Plane
(negative regions bounded by dashed lines and directed out of page)

5.5 Conclusions – Phase One

Three-dimensional mean velocity data were acquired experimentally from four planes in the near-wake of a model-scale Champ Car wheel. The data were used to verify and validate a computational model of the experiment, which was in turn used to predict the interference effect of the wheel support sting.

In terms of the methodologies, the study has demonstrated the following points.

- The RMCS laser Doppler anemometer can be successfully employed in a large wind-tunnel environment.
- A relatively modest computational model can generate verifiable, valid results and be used to predict experimentally-challenging test conditions.

Aside from proving the methodologies, analysis of the results yielded several initial conclusions regarding the flow in the near-wake and the interference effects.

Near-Wake Structure

- Regions of upstream flow have been measured experimentally and observed to extend outside the projected profile of the wheel.
- The hub vortices, expected from the literature, were not observed experimentally.
- The lower vortices were larger, more defined and were convected further than the upper vortices.
- From the simulation the flow exiting the contact patch was found to locally deflect the freestream modifying the effective shape of the wheel.

Interference Effects

- The sting appears to suppress the formation of the upper, trailing vortex on the opposite side of the wheel to itself.
- Tyre centreline surface pressures and wheel forces are relatively insensitive to the presence of the sting.
- Mass flow through the spokes is greatly increased (+58 %) by the support sting, which could be expected to have an impact upon brake cooling performance.

The analysis carried out in this phase has highlighted the complexity of the near-wake and the potential discrepancy with previously-published models of this region. Phase Two will be an opportunity to test the conclusions of this phase against different test components and conditions in an attempt to clarify further the near-wake structure and the interference effects of the sting.

6 Phase Two – Formula One

6.1 Introduction

It was established during the review of published literature that a fundamental gap exists regarding the structure of the wake of a road wheel. A lack of three-dimensional velocity data, especially in the near-wake, was illustrated by the publishing of contradictory wake models in major vehicle science textbooks. Phase Two of the current work has built on the foundations of Phase One and aims to clarify the disparate literature whilst also identifying the prominent features in the wake of a wheel. This main aim is accompanied by three other novel objectives:

1. the qualitative relationship between sting design and interference effect is investigated by the sequential use of three geometrically-different support stings;
2. the flowfield of the wheel in the presence of a car is investigated and compared with that of an isolated wheel;
3. experimental evaluation of the sting interference effect is attempted by testing in a "wheels-on" configuration.

Overall the work attempts to extend the available knowledge base and open up new areas for future investigation whilst also beginning to address the industrial problem of support sting interference.

The experimental and computational methodologies proved in Phase One were retained for this work, as outlined in Chapters 3 and 4 respectively. The following sections will complete those outlines with details of the particular components and conditions used in the experimental and computational stages of this phase. The data will be presented in a similar manner to Phase One and discussed with particular reference to the aims and objectives outlined above.

6.2 Experimental Details

Chapter 3 outlined the experimental method used throughout both phases of this research. This section will focus on the introduction of the new test components, conditions and their impact on data acquisition. Wind tunnel specifications and test settings can be found in Appendices A and B respectively.

Test Components

The new test components comprised a new wheel assembly, two new support stings and a model-scale racecar. It has been important throughout this work to reflect the current state of racecar aerodynamic development. As such the additional components were provided by Jaguar Racing, having been employed in the development of their Formula One cars from 2000 onwards. The Champ Car wheel assembly used in Phase One was not re-investigated as it was incompatible with the racecar.

The 50 %-scale Formula One front wheel assembly is shown in exploded detail in Figure 3.2 on page 22 and cross-sectioned in-situ in Figure 6.1. The latter figure illustrates the hub spoke pattern (similar to that of the Champ Car wheel) and the profile of the non-deformable, carbon-fibre tyre, including the position of the grooves on its surface. The restriction of flow through the hub by the presence of the brake rotor and suspension upright is also indicated.

The detail in Figure 3.2 shows the radial ventilation channels in the aluminium brake rotor and the intricate spoke pattern of the suspension upright produced using a rapid-prototyping technique.

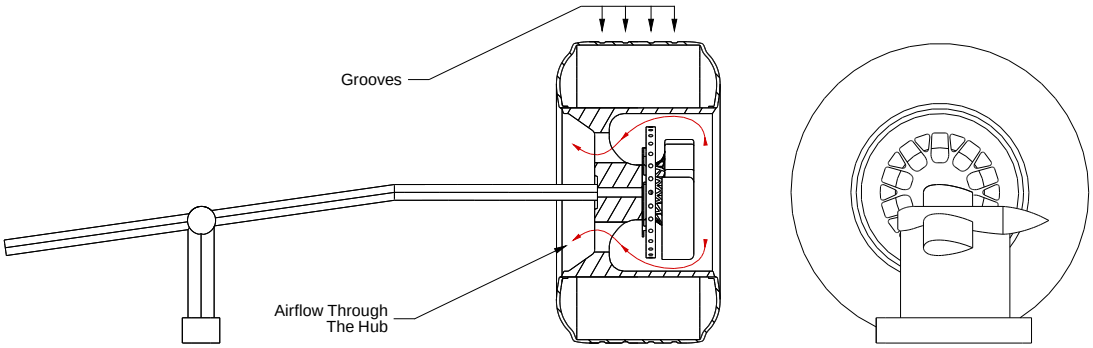

Figure 6.1: Formula One Wheel Assembly & Support Sting

The support sting shown in Figures 6.1 and 3.2 is the same as that used in Phase One. An additional two stings were used in this work and all three are shown in Figure 6.2, to scale and labelled by name. The rear view has been rotated for illustration purposes only and is not intended to suggest that the wheel was supported from both sides. The figure also includes the thickness-to-chord ratio (t/c) of the symmetrical aerofoil section closest to the wheel, where all except the carbon sting had a blunt trailing edge.

The second part of this phase included a fully-detailed, 50 %-scale model Formula One car. The car, designated R1 by Jaguar Racing, was suspended from the tunnel overhead support-strut in close proximity to the road. Only one wheel assembly was used, supported in turn by the stings and the model suspension. The lack of the other three wheels was assumed to have negligible effect in this configuration and greatly reduced the model set-up time. A photograph of the test configuration is shown in Figure 6.3.

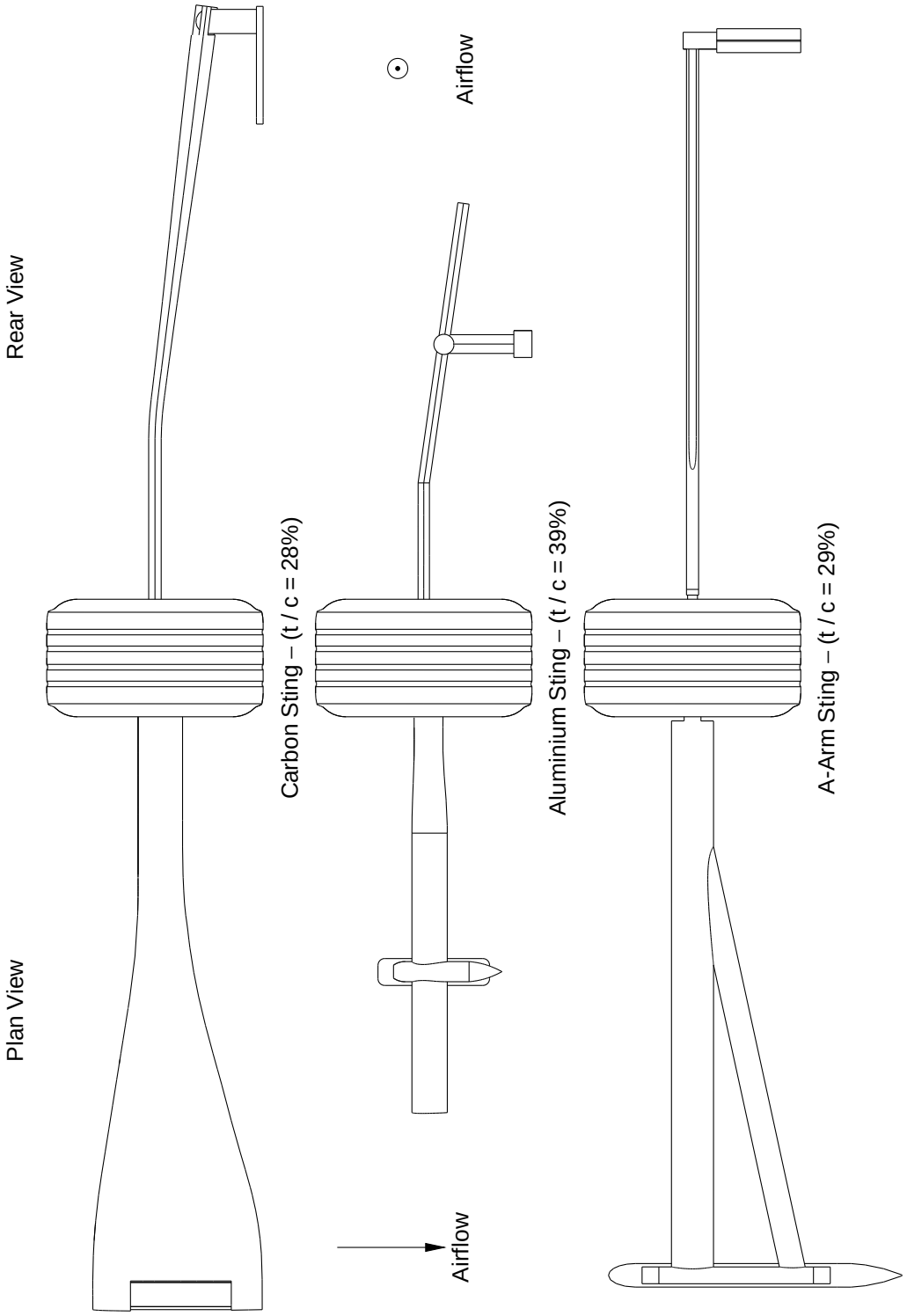

Figure 6.2: Comparison of Support Sting Geometry
Including Thickness-to-Chord Ratio of Section Nearest the Wheel

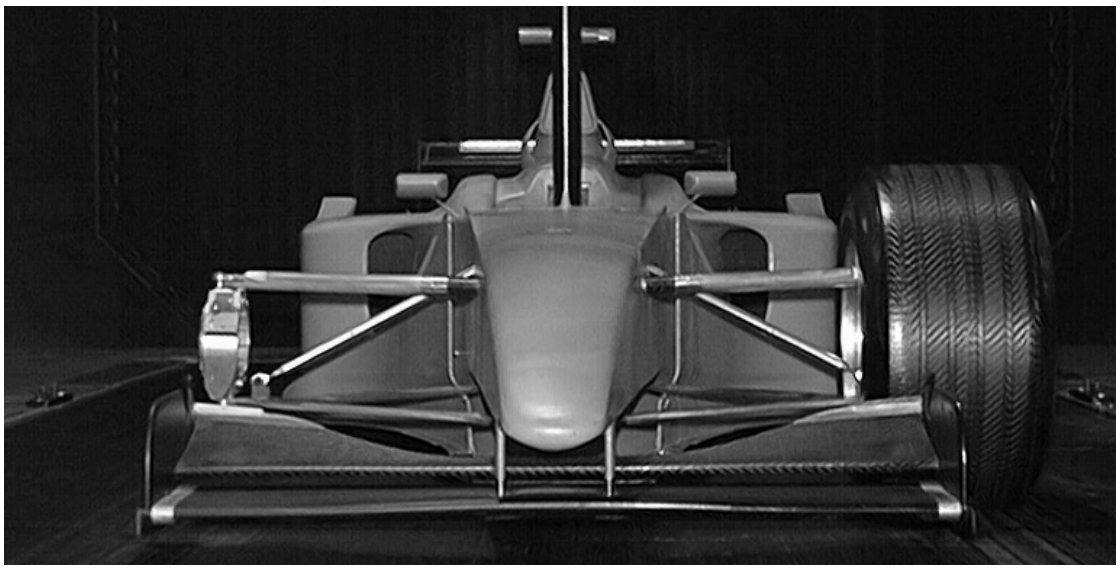

Figure 6.3: Jaguar R1 in Test Configuration (Suspension-Mounted Wheel)

Wind Tunnel

All of the testing in this phase was carried out in the D.S. Houghton open-jet wind-tunnel at a constant freestream velocity of 30 ms^{-1}. This was 150 % of the test speed used in Phase One which, combined with the increased scale of the Formula One components, increased the test Reynolds number, based on wheel diameter, to 6.8×10^5. The blockage, based on the ratio of the projected frontal areas of the wheel and wind-tunnel nozzle was 1.4 %. Air temperature, boundary layer control and the rolling road were as described in the experimental method of Chapter 3.

The aim of increasing Reynolds number was to improve comparison with the literature and to give an indication of whether the results of Phase One were Reynolds number specific. The switch to the D.S. Houghton wind-tunnel was unavoidable as the OJWT used in the initial phase was not sufficiently large to accommodate the R1 model.

Test Procedure

The measurement programme once again revolved around the extraction of planes of three-dimensional velocity data from the near-wake of the wheel. In this phase data collection was complicated by the large test section of the D.S. Houghton wind-tunnel and also by the presence of the car.

Firstly, in order for the probes to remain physically outside the wind-tunnel jet and maximise the non-intrusive quality of the LDA measurements a long focal length ($f > 2$m) was required. The Shrivenham laser Doppler anemometer can operate at this distance but has only one $f =$ 2.5m lens and therefore only one probe can be used, simultaneously recording two components

of velocity. In practice the quality of the data was improved by measuring the components individually. Three tests, therefore, were needed for each wheel and sting combination (per measurement plane), with a single component recorded in each test. The resultant components were combined and transformed into the tunnel frame of reference using the procedure described in Appendix D.

Secondly, the surfaces of the road, wheel and car reflected the laser light back towards the probe reducing the signal-to-noise ratio. The reflections from the road did not significantly affect the quality of the data and the region affected by the wheel was limited to approximately 20 points in one traverse plane (60 % of one wheel diameter downstream). However, reflections from the light-coloured barge-board of the car affected approximately one quarter of each measurement plane. It was not possible to remove the reflections completely, but the application of matt, fluorescent-magenta tape to the car doubled the data rate and increased the signal-to-noise ratio. Fluorescent magenta was found to be more effective than conventional matt black or red as it actively absorbed some laser light during fluorescence reducing the amount of light reflected at the incident wavelength.

Table 6.1 summarises the measurement planes sampled for each test configuration. All planes were 340 mm$\times$340 mm and contained 613 equi-spaced points. A maximum of 20 seconds was spent at each point collecting a maximum of 5000 samples.

Table 6.1: F1 Measurement Planes (Distance Downstream of Wheel Axis in Diameters, D)

	Measurement Plane (%D)		
Test Configuration	**60 %**	**75 %**	**100 %**
Isolated Wheel	✓	✓	✓
Wheel & Car	×	✓	✓

6.3 Computational Details

A 1.65×10^6-cell model of the Formula One wheel assembly and the aluminium support sting was generated and solved using the approach detailed in Chapter 4. 64 CPU hours were required on 8 nodes of an SGI Origin2000 26-processor machine to converge each of the supported and unsupported wheels. Three-dimensional velocity components were exported from positions equivalent to those measured experimentally, along with the circumferential surface pressure distribution on the tyre centreline $(\mathrm{Y/D}= 0)$. Details of the model and the solver settings are summarised in Appendix C.

6.4 Results & Analysis

The computational and experimental data gathered in this section will be divided into three groups and presented in a similar manner to Phase One. The experimental isolated wheel data will form one group, whilst the wheel-and-car data and the computational results will constitute the remaining two. Comparison within and between the groups will attempt to address the main aims of this study.

All velocities were non-dimensionalised by the freestream, u_∞, and distances by the wheel diameter, D. Vector plots were used to represent the direction and magnitude of the in-plane (v-w) components, along with filled contours for the stream-wise component, u and associated turbulence intensity, Ti_u. Line Integral Convolution (LIC) was once again used to give improved visualisation of the shape and extent of the near-wake vortical structures. Additionally, centreline velocity profiles were used in the verification and validation of the computational model, as were delta contours of u-velocity.

6.4.1 Isolated Wheel – Experimental Data

In this subsection the isolated wheel results will be used to evaluate the effect of the different sting designs on the near-wake of the wheel whilst further clarifying its structure. A comparison will also be made between the aluminium sting results of both phases, although the Phase One data will not be re-presented. Error analysis of the experimental data is included in Appendix E.

Mean u-Velocity Data

The contours presented in Figure 6.4 appear similar on first inspection. Closer inspection reveals the impact of sting design on several key areas of the near-wake. Initially it is informative to compare the results of the aluminium sting in Figure 6.4 with those of Phase One, Figure 5.2 on page 41.

The two studies are qualitatively, and to some extent quantitatively, comparable. The main features noted in Phase One are present in the current data, with the exception of the upper lobes. Those present include:

- a central region, of approximately the same width and height as the wheel;
- two large ground lobes;
- regions of reversed flow extending beyond the projected profile of the wheel;
- a degree of asymmetry, especially in the lobes.

Aside from the upper lobes, the Formula One data also exhibit significantly larger central and upper regions of reversed flow and are notably more symmetrical about the wheel centreline,

$Y/D = 0$. The regions of reversed flow are similar to those captured in the Phase One CFD, Figure 5.2, which had not been observed experimentally prior to this work.

Returning to the effect of the support sting design, as illustrated by Figure 6.4, the individual stings have little effect on the overall shape and extent of the near-wake. However, there does appear to be some correlation between the sting, asymmetry and reversed flow. Figure 6.5(a) reduces the data to a single contour $(u = 0)$ to delineate the edge of the reversed flow region. The regions from each support sting are overlaid and presented for each measurement plane[1]. The aluminium sting consistently has the smallest regions of reversed flow whilst the carbon sting has the largest. The carbon sting also has higher intensity reversed flow as illustrated by the u-velocity profiles shown in Part (b) of the same figure. These profiles also show all three stings exhibiting the same trends over the height of the plane and recovering to very similar values when $Z/D > 1$.

The experimental data are sufficient to confirm that the sting interferes with the reversed flow and the wake asymmetry in particular whist having little impact on the overall size and shape of the wake. However the data do not allow identification of the underlying mechanisms. Figure 6.5 clearly illustrates that a link, albeit a complex one, also exists between the design of the support sting and its impact on both the reversed flow and asymmetry.

In-Plane (v–w) Velocity Data

Phase One highlighted the four main features of the in-plane velocity data and, as with the u-contours, most are replicated in the current aluminium sting results, Figures 6.7 and 6.8 on pages 71 and 73 respectively. In both phases the vortical structures remained within or aligned with the projected wheel profile and were accompanied by large regions of up-wash at either side of the wheel. However, as the current aluminium sting results were much more symmetric about the tyre centreline $(Y/D = 0)$ the central down-wash region was not shifted towards the sting as observed in Phase One.

The most notable feature of the in-plane data of the initial phase was the absence of a vortex shed from the upper right quadrant of the wheel. The computational results of that study suggested that the absence of the upper-right vortex was due to the presence of the support sting and was therefore linked to the mass-flow-rate through the wheel. However, an upper-right structure *is* present in the current data, clearly shown in the 60 %-planes of Figure 6.8.

In an attempt to clarify the origins of the upper trailing vortices a further plane of measurements was made for each wheel and sting combination. The plane was located 0.4D downstream of the wheel axis at which point the tyre and plane intersected. This intersection coupled with points lost due to reflections from the tyre and hub surface left only the 127 uppermost points to be investigated. These points were processed using the LIC technique to generate the plots shown in Figure 6.6.

[1] The jagged saw-like contours which are prominent in these plots, but also visible in all the u-contour plots, are an artifact of the measurement grid and not a feature of the flow.

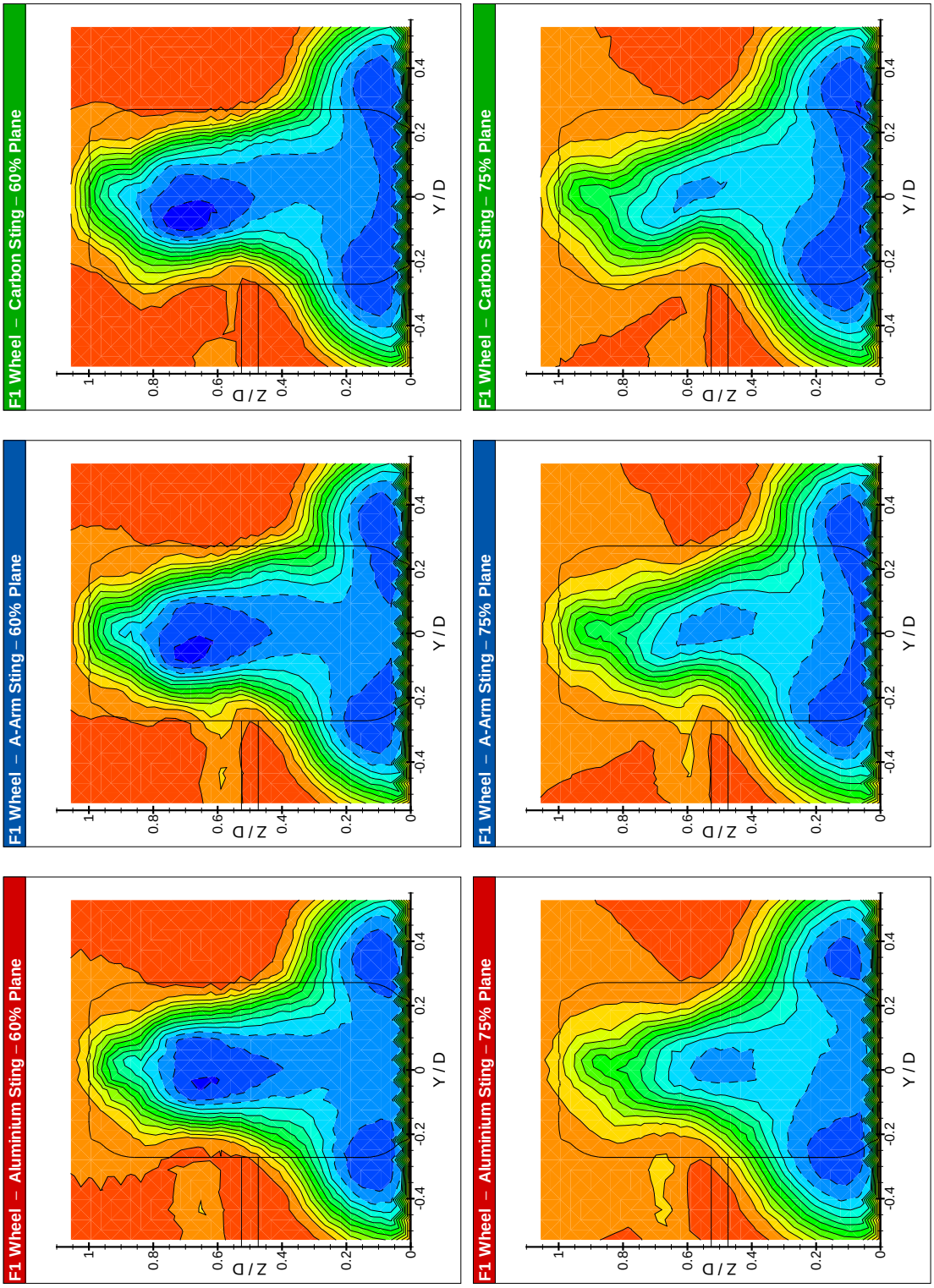

Figure 6.4: Isolated Formula One Wheel – Contours of Mean u-Velocity
(negative regions bounded by dashed lines)

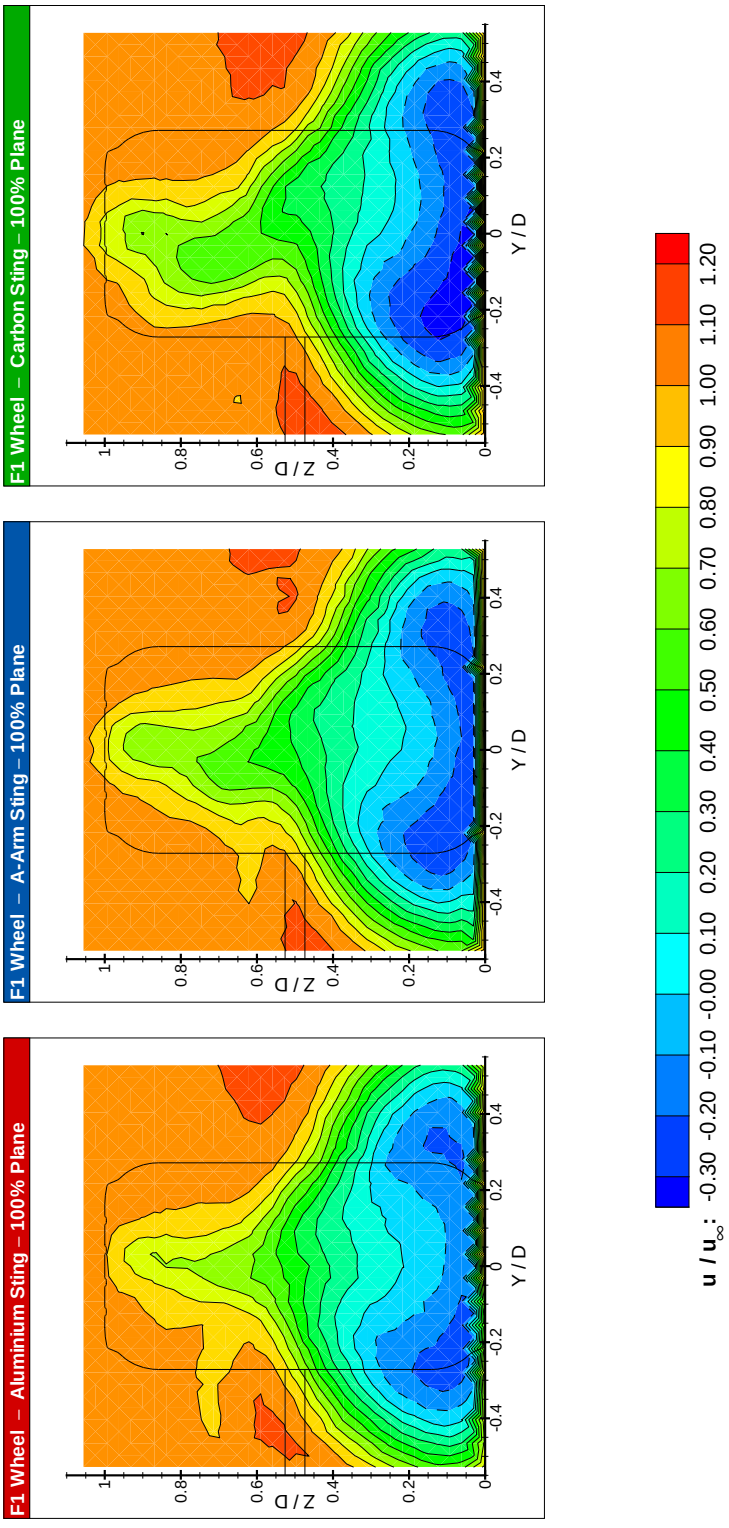

Figure 6.4: (cont.) Isolated Formula One Wheel – Contours of Mean u-Velocity (negative regions bounded by dashed lines)

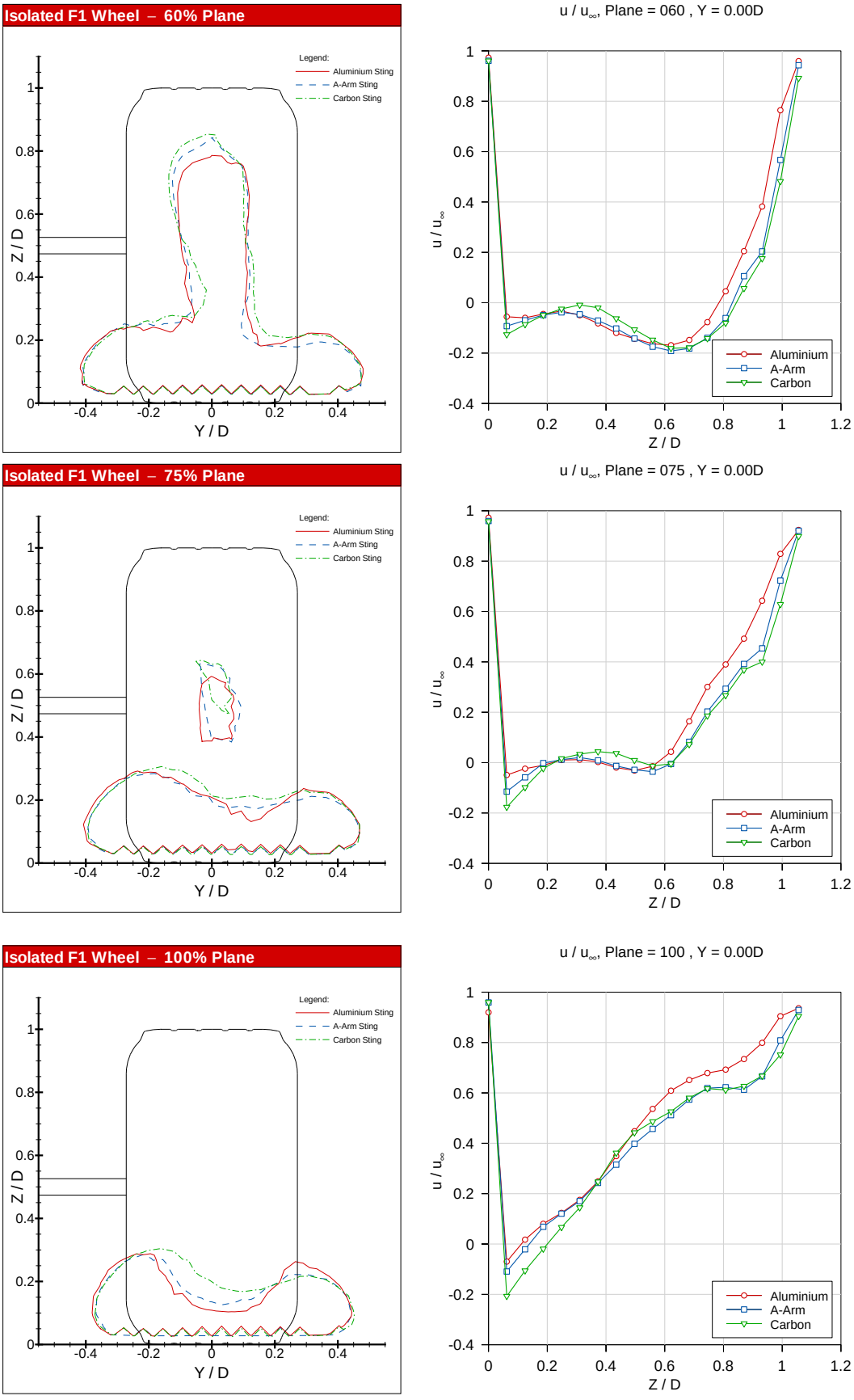

(a) Contour of Zero u-Velocity

(b) u-Velocity Profile - Vertical Centreline

Figure 6.5: Comparison of Support Stings – Effect on Reversed Flow

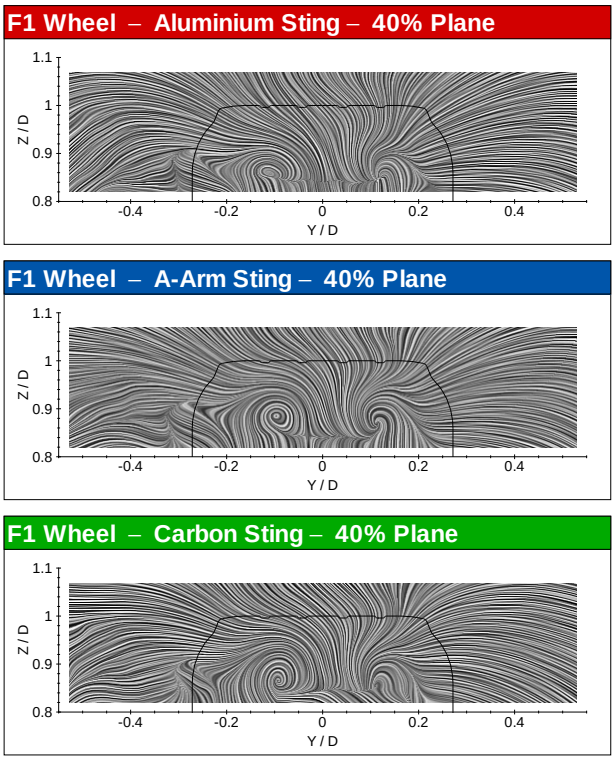

Figure 6.6: Isolated Formula One Wheel – 40 % Plane – Line Integral Convolution Images

All of the wheel and sting combinations in Figure 6.6 have a pair of trailing vortices visible at this upstream position. As with the plot of the path of the vortex core in Phase One, this figure confirms that the upper vortices measured in this phase have their origins at the top of the wheel. Their position inside the projected profile suggests that they roll up from the shoulders of the tyre immediately proceeding the flow separation, not dissimilarly to the leading edge vortices of an inclined delta wing.

It was observed in Phase One that the vortex centres remained within or aligned with the projected profile of the wheel. Figure 6.9 presents the vortex centres from all twelve planes of measurements (4 downstream stations and 3 support stings) and confirms that this observation also applies in the current Phase. The only structures to occur outside the profile are ground-level secondary flows present one wheel diameter downstream. The centres also show that the trailing vortices do not spread laterally (up to 1D downstream) as they have streamwise oriented axes.

Whilst comparison between the Formula One v–w datasets in the 60 %-plane is hindered by the points lost due to poor signal quality, they appear to illustrate a link between design of the sting and its impact on the near-wake flow. In Figure 6.8, the upper structures in the first plane of the carbon sting are notably more defined than those of the aluminium and A-arm stings. Comparison of the remaining planes reinforces the suggestion that wake asymmetry is affected by sting design, also noted in the discussion of u-data.

The data collected in this phase show that the initial conclusion that the presence of a sting

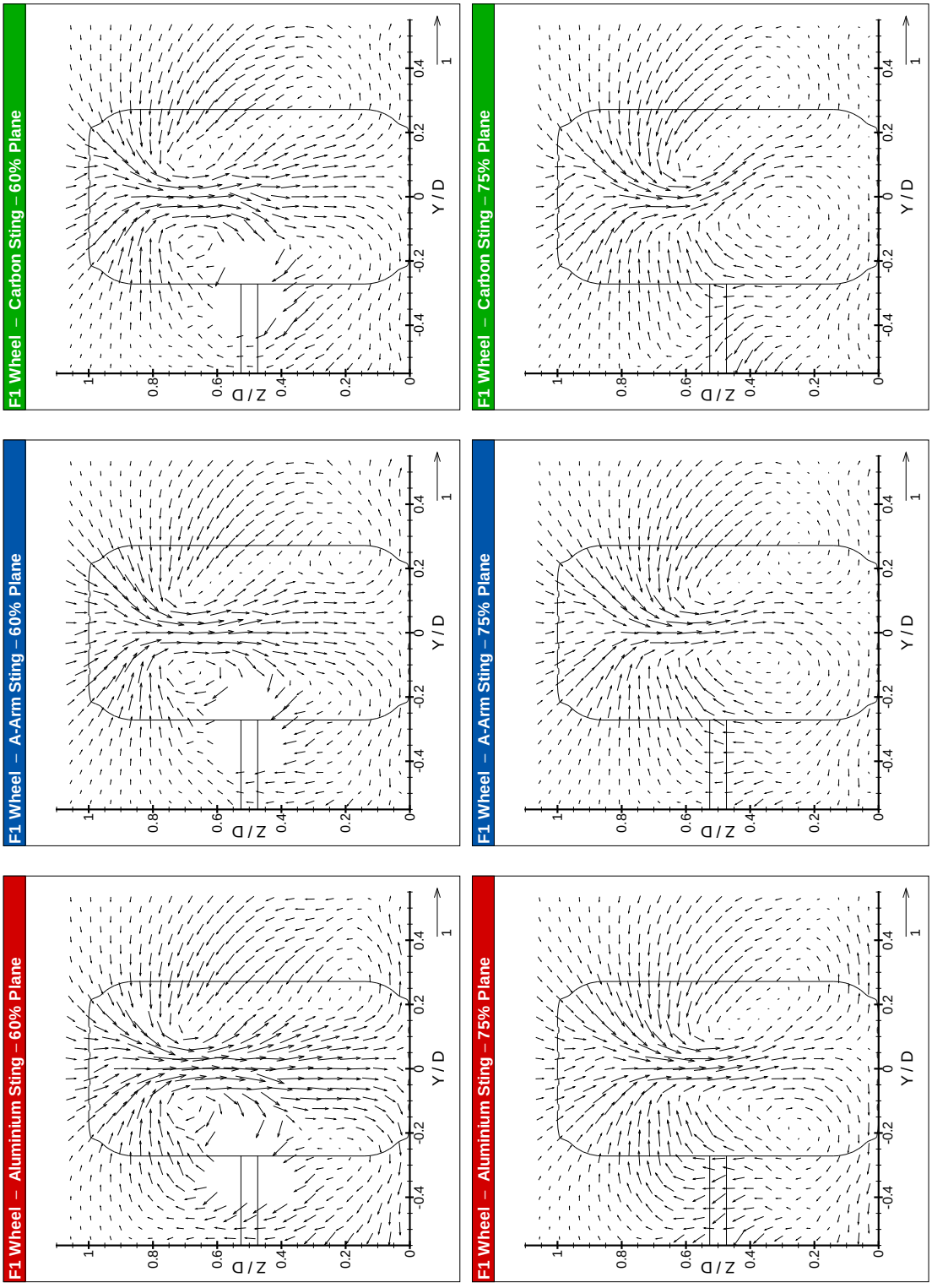

Figure 6.7: Isolated Formula One Wheel – In-Plane (v–w) Velocity Vectors

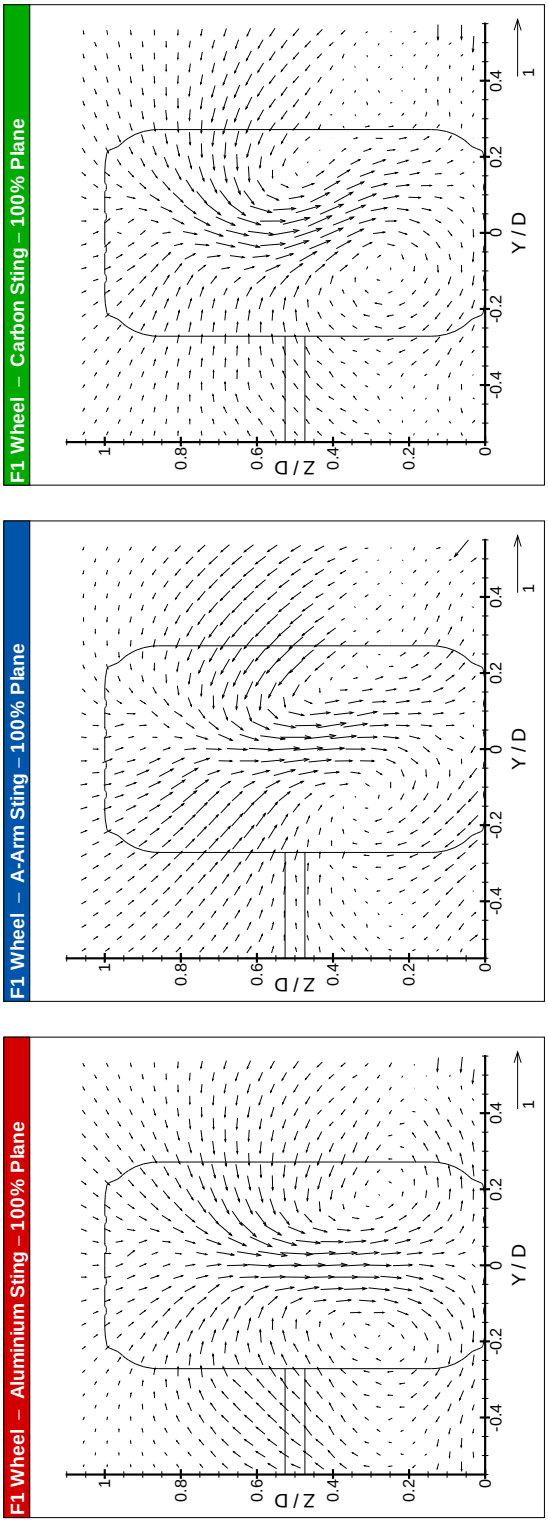

Figure 6.7: (cont.) Isolated Formula One Wheel – In-Plane (v–w) Velocity Vectors

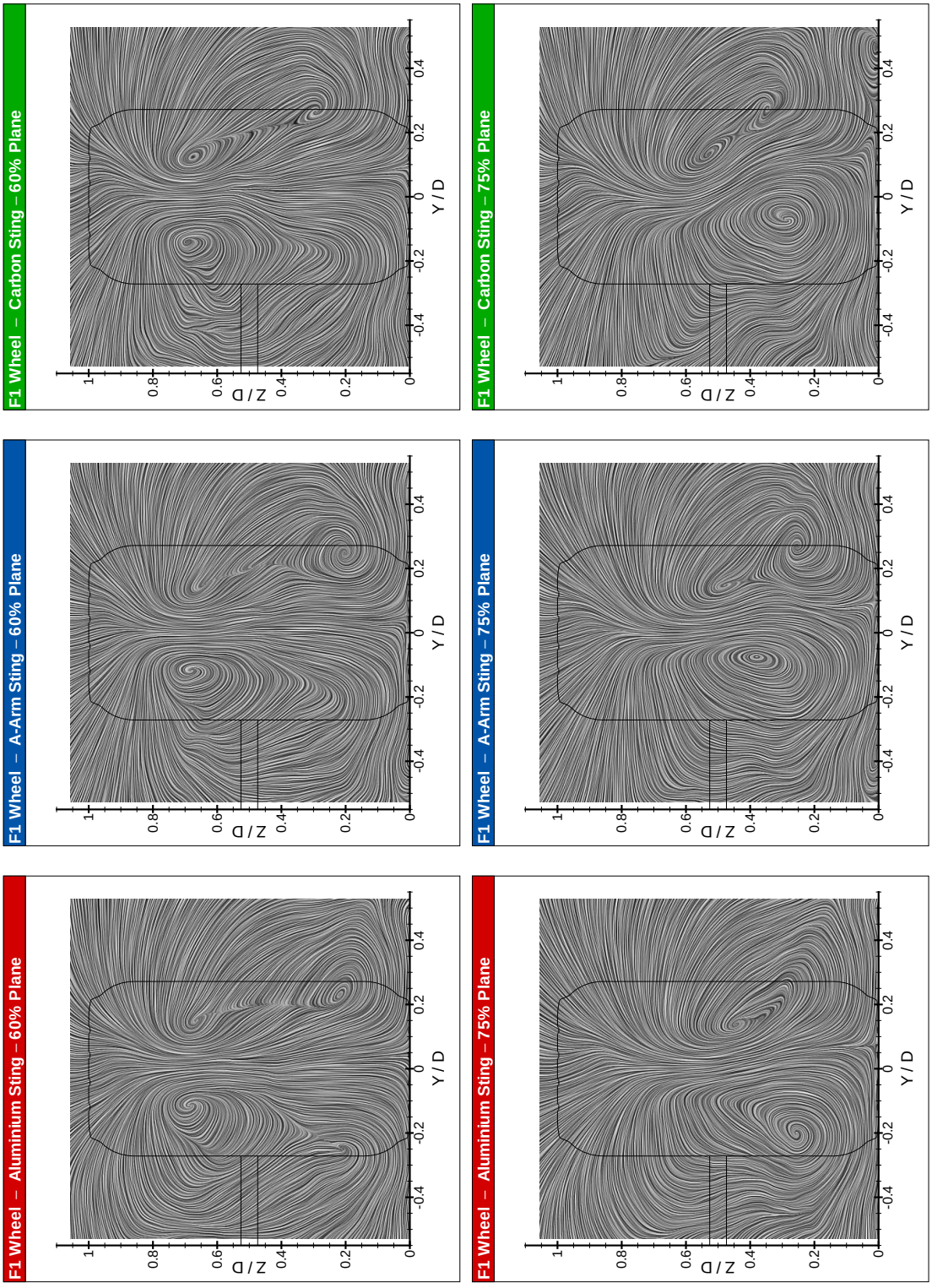

Figure 6.8: Isolated Formula One Wheel – Line Integral Convolution Images

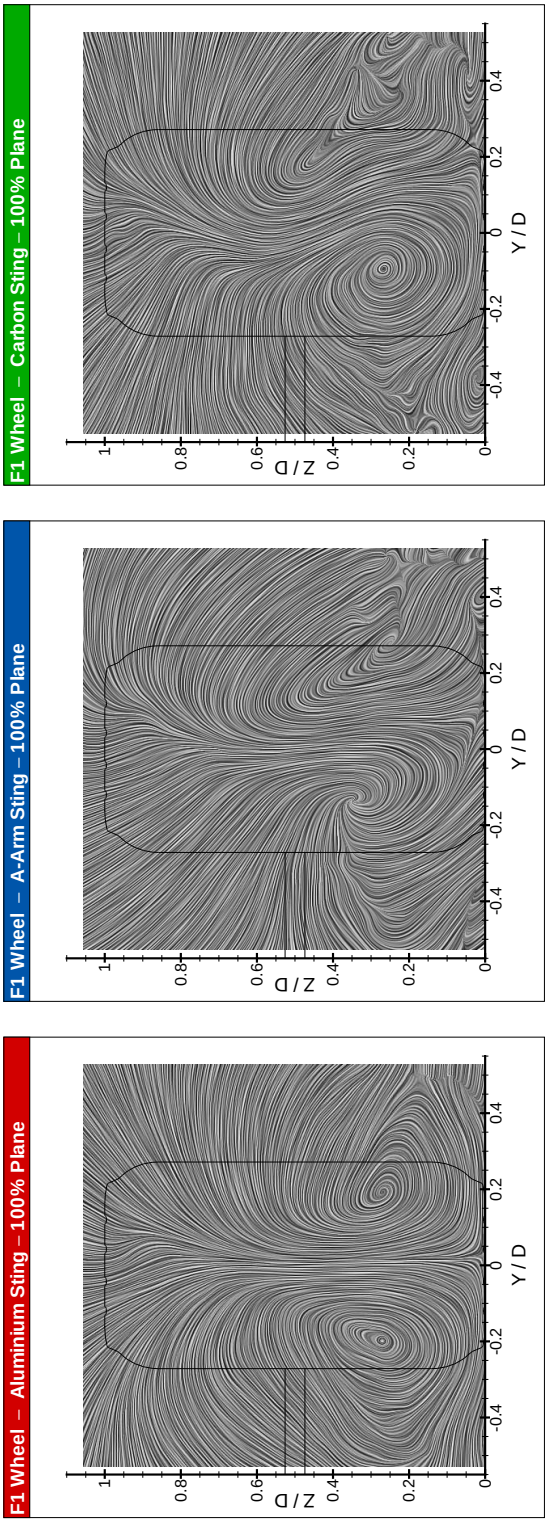

Figure 6.8: (cont.) Isolated Formula One Wheel – Line Integral Convolution Images

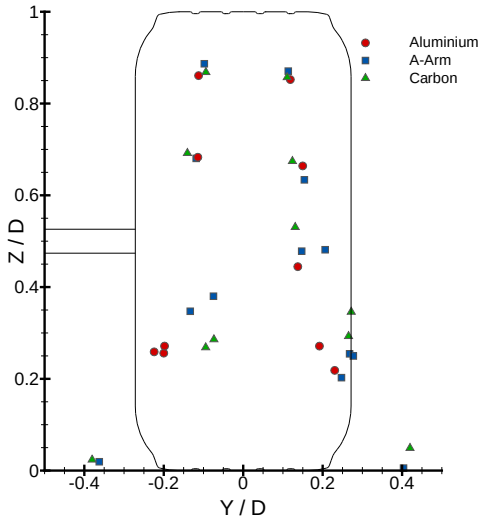

Figure 6.9: Vortex Centre Positions

suppresses the formation of an upper-right vortex is not valid in all cases. However, the data have confirmed that the sting interferes with the vortical structures in the near-wake of the wheel and this reinforces the suggestion that the magnitude of this effect is dependent on sting design.

The experimental data cannot identify the cause of the discrepancy between the two phases in the interference effect of the aluminium sting. The different test components and Reynolds numbers would be expected to account for some differences, whilst analysis of the current data suggests another contributory factor. If the scale of the wheel were to be reduced, the same sting could be expected to exhibit greater interference as it becomes relatively larger. Therefore, whilst the interference effect of the aluminium sting on a 40 %-scale wheel was vortex suppression, at 50 %-scale the effect reduces to vortex attenuation.

Streamwise Turbulence Intensity

In Phase One it was noted that the regions of high streamwise turbulence intensity ($Ti_u > 30$) corresponded with the shear layers and in particular the regions of reversed flow and trailing vortices. Figure 6.10 presents the Ti_u contours for the Formula One wheel on the same scale as Phase One and similar trends can be observed.

For example, in each of the 60 % planes of Figure 6.10 high Ti_u regions exist corresponding to the upper trailing-vortex centres, whilst much larger regions correspond to the shear layer of the lower lobes. The lower regions of high Ti_u expand as the flow is convected downstream, but now contain islands of reduced intensity which appear to correspond to the peaks in reversed flow.

One of the features noted in Phase One was the bisection of the centre of the wake by a relatively

low intensity region. This bisection is visible in Figure 6.10 and further illustrates the effect of the sting design on wake asymmetry especially as the wake is convected.

6.4.2 Isolated Wheel – Computational Data

In the following subsection the computational data will be used, as in Phase One, to predict sting interference effects on an isolated wheel. No claim is made as to the quantitative accuracy of the results and, as such, they are verified against their prediction of the features of the flow rather than their magnitudes. The data are subsequently used to provide insight into, and an indication of, the effect of the support sting. Rather than quantitative prediction of the flow surrounding the experimentally-challenging unsupported wheel.

Figures 6.12 and 6.16 show the CFD results in planes equivalent to those measured experimentally. The results of the supported- and unsupported-wheel simulations are included one above the other for comparison.

Mean u-Velocity Data

Following analysis of both phases of experimental work it has been proposed that the near-wake of an isolated wheel would include a narrow central section, ground lobes, asymmetry and reversed flow. Whilst all of these features are present, the results of the simulation exhibit the same issues identified in Phase One. For example, while the key features of the aluminium sting flowfield are captured (Figure 6.4), their sizes and/or extents are not.

Figure 6.11(a) shows that on the horizontal centreline the central section of the wake is predicted wider than observed experimentally although the trend and shear layer thickness has been captured. Whilst the magnitude of the reversed flow is better predicted than in Phase One its distribution is not, as shown in both centreline velocity profiles. The negative peak at $Z/D \approx 0.7$ seen in both phases is the major factor in the consistent over-prediction of wake height.

The delta plot in Figure 6.13 shows that the discrepancies noted in the early planes continued downstream. The upper negative region illustrates the over-prediction of wake height whilst the positive region in the lower-right corner is due to the reduced size of the ground lobe in this area.

In terms of the effect of the sting on the flowfield, the results in Figure 6.12 agree with the experimental data, in that the sting has little impact on the shape and extent of the wake but does affect the reversed flow and hence the asymmetry.

In-Plane (v–w) Velocity Data

The velocity profiles of the in-plane data, Figure 6.14, clearly show the main areas of discrepancy between the simulated and measured results. For example, in part (a) of this figure the CFD and LDA results both follow the same trends excepting that is the region surrounding $Y/D \approx -0.3$

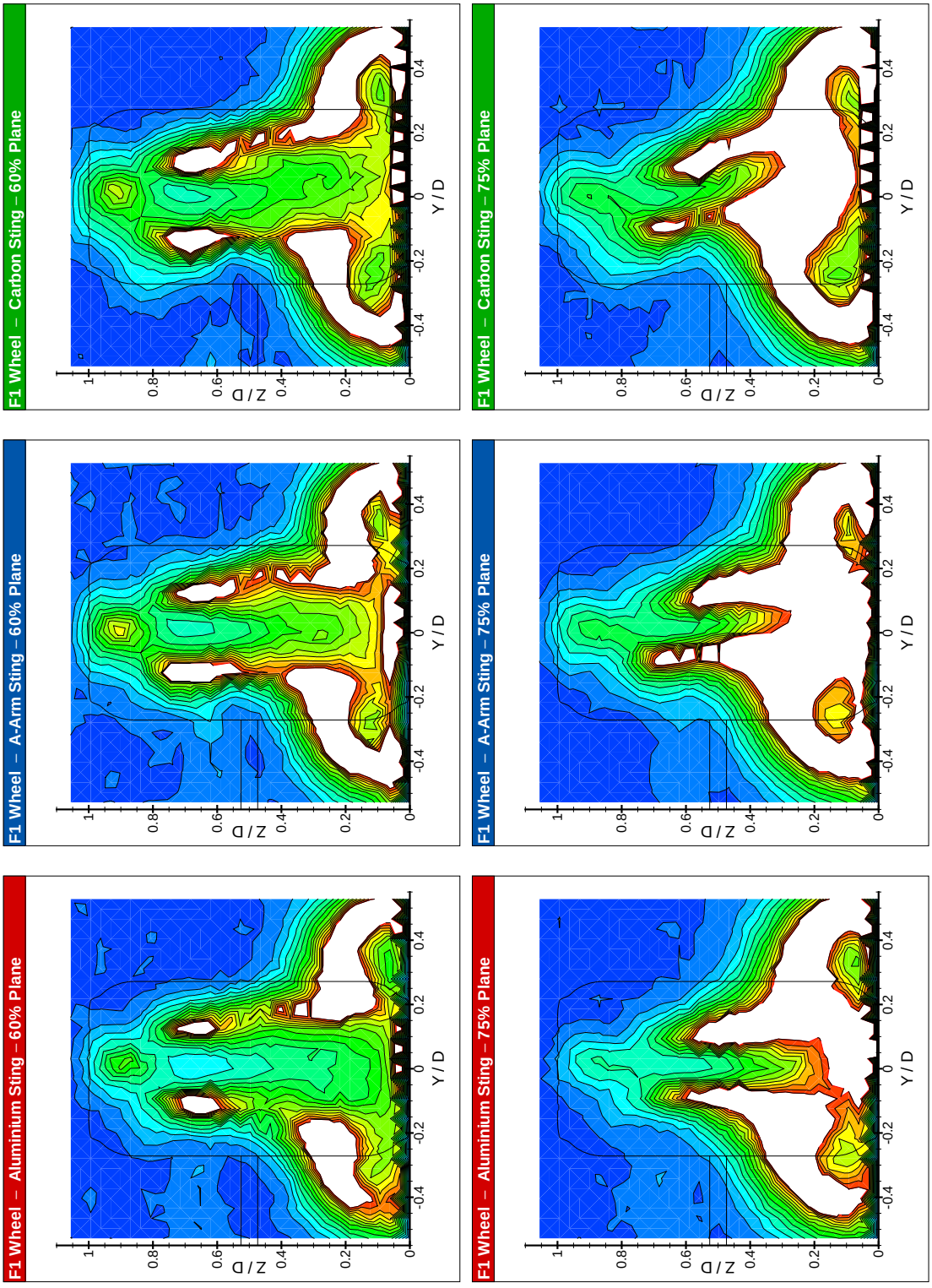

Figure 6.10: Isolated Formula One Wheel – Contours of Streamwise Turbulence Intensity

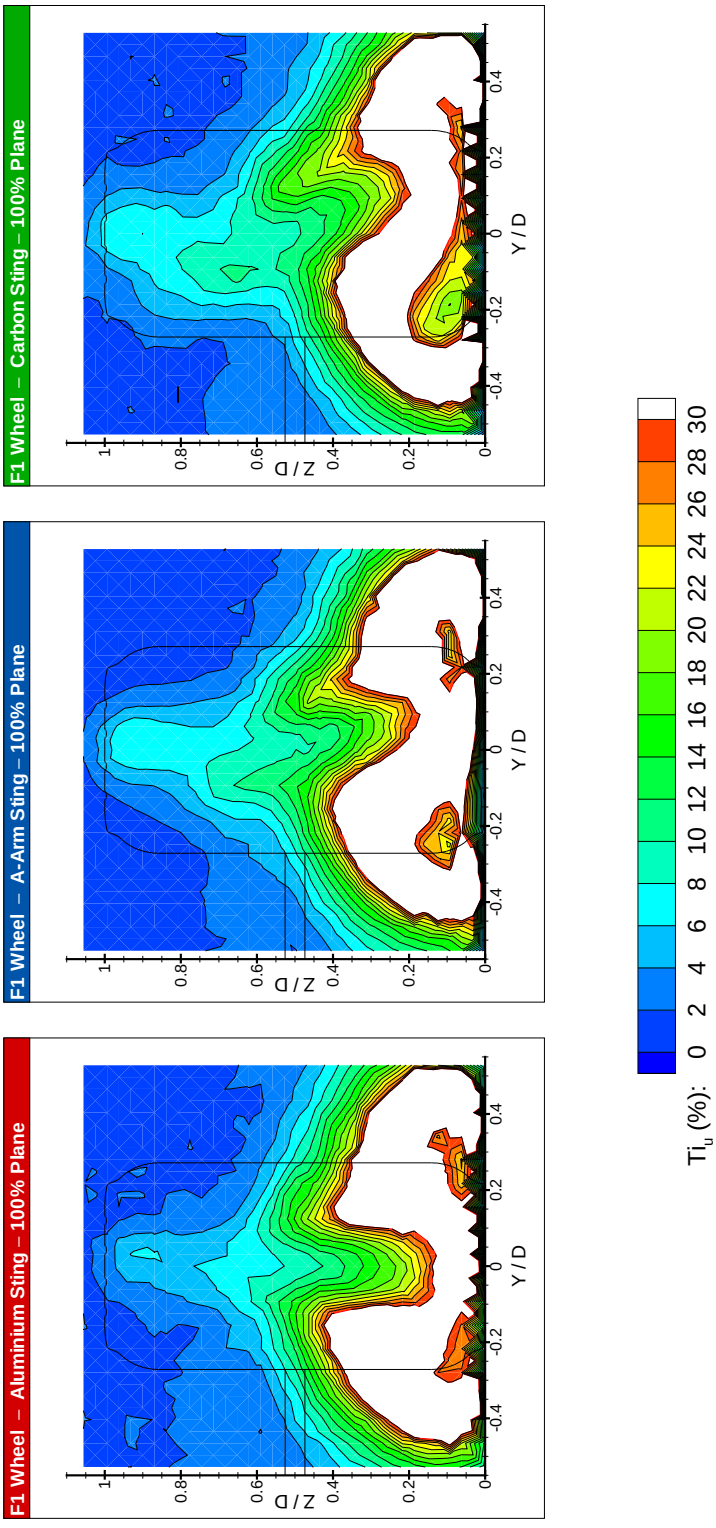

Figure 6.10: (cont.) Isolated Formula One Wheel – Contours of Streamwise Turbulence Intensity

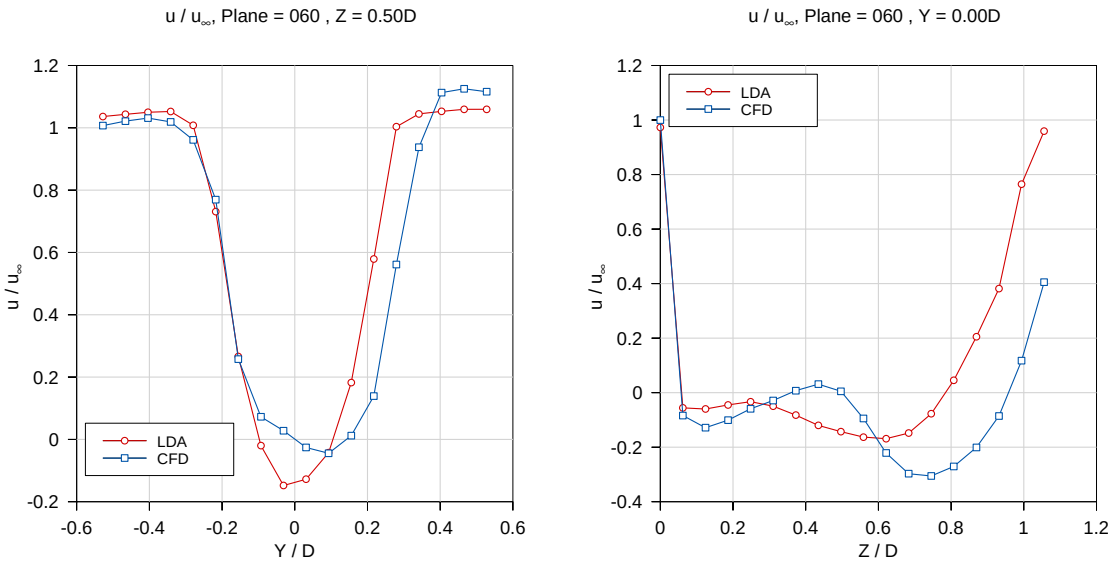

(a) Horizontal Centreline $(Z/D = 0.5)$

(b) Vertical Centreline $(Y/D = 0)$

Figure 6.11: Comparison of LDA & CFD Centreline u-Velocity Profiles - 60 % Plane with Sting

which was adversely affected by reflections in the experiment. The w-profile shows that the CFD did not capture the magnitude of the down-wash (negative w) in the centre of the plane. An observation which can also be made from the corresponding plot of the vertical centreline. Of the three velocity components, the centreline profiles have revealed that w-velocity is the least well predicted.

The vector plots of the computational data, Figure 6.15, are included to show that the direction of the flow was the same as measured experimentally, whilst the LIC plots of Figure 6.16 illustrate far more clearly the predicted structure of the wake.

The CFD simulation of the supported wheel correctly predicts the presence of two upper structures and also increased definition of the upper-left structure. The centres of the trailing vortices are too high, although this was expected following the over-prediction of wake height in the u-data. The poor prediction of the right ground lobe has resulted in the lack of a coherent lower right vortical structure.

The prediction of the flow about an unsupported wheel in Figure 6.16 shows, as observed experimentally, that the sting has an isolated effect on the vortical structures in the near-wake. In particular the sting affects the upper-right vortex in the 60 %-plane and the main vortex in the 100 %-plane.

Centreline Pressure Profile

Phase One used experimental surface pressure data, published by Hinson [20], as validation criteria for the computational model. In Phase Two the same data are even more applicable as

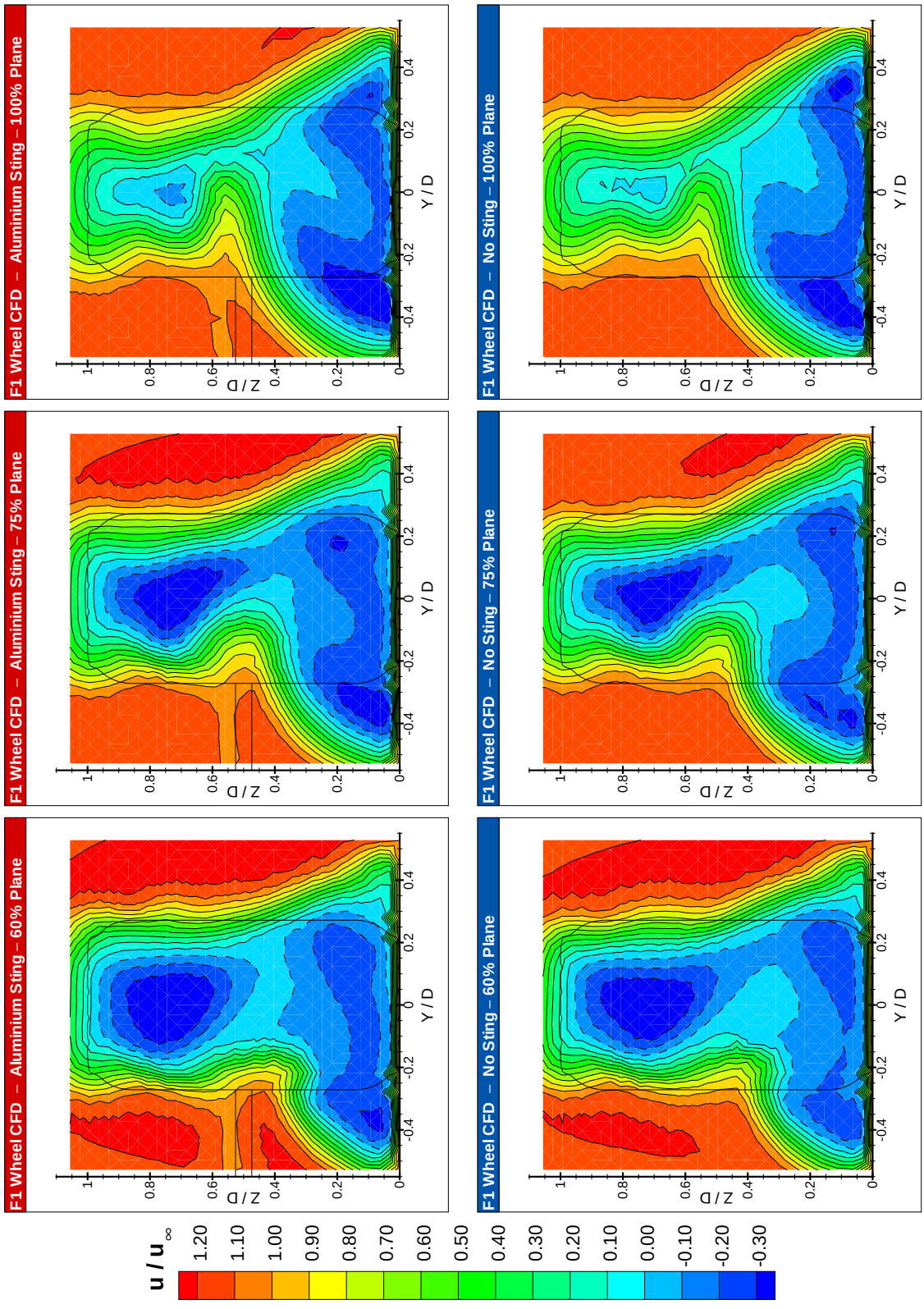

Figure 6.12: Isolated Formula One Wheel – CFD Contours of Mean u-Velocity
(negative regions bounded by dashed lines)

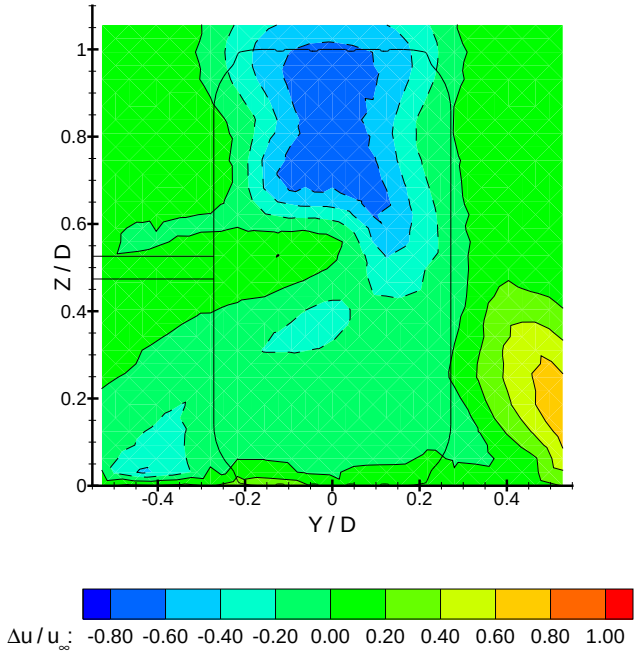

Figure 6.13: Δu - 100 % Plane $(\Delta = \text{CFD} - \text{LDA})$

the Formula One wheel used by Hinson was almost identical to that used in this phase. Figure 6.17 presents the experimental and computational circumferential pressure profiles at the tyre centreline $(\text{Y}/\text{D} = 0)$.

The main regions of interest in Figure 6.17 are around the contact patch $(\theta = 90^\circ)$ and the separation zone $(\theta \approx 270^\circ)$ as they are widely considered to be two of the governing features of wheel flowfields.

In the vicinity of the contact patch, the computational model predicts both the upstream and downstream pressure peaks measured by Hinson and discussed in the literature review. Whilst both peaks are over-predicted in comparison with Hinson's data, they are not excessive since Fackrell [12] experimentally measured an upstream peak of $C_p \approx 2$.

Experimental flow separation can be seen to occur at approximately the highest point of the tyre, $(\theta \approx 270^\circ)$ after a slight region of adverse pressure $(285^\circ \geq \theta \geq 270^\circ)$. In the computational case the flow does not tolerate any adverse pressure gradient and separation is predicted to occur when $\theta \approx 295^\circ$, upstream of the highest point of the tyre.

During discussion of the CFD u-contours it was noted that the height of the wake was consistently over-predicted. The experimental data presented in Figure 6.17 suggests that this could also be a consequence of predicting flow separation upstream of the highest point of the wheel.

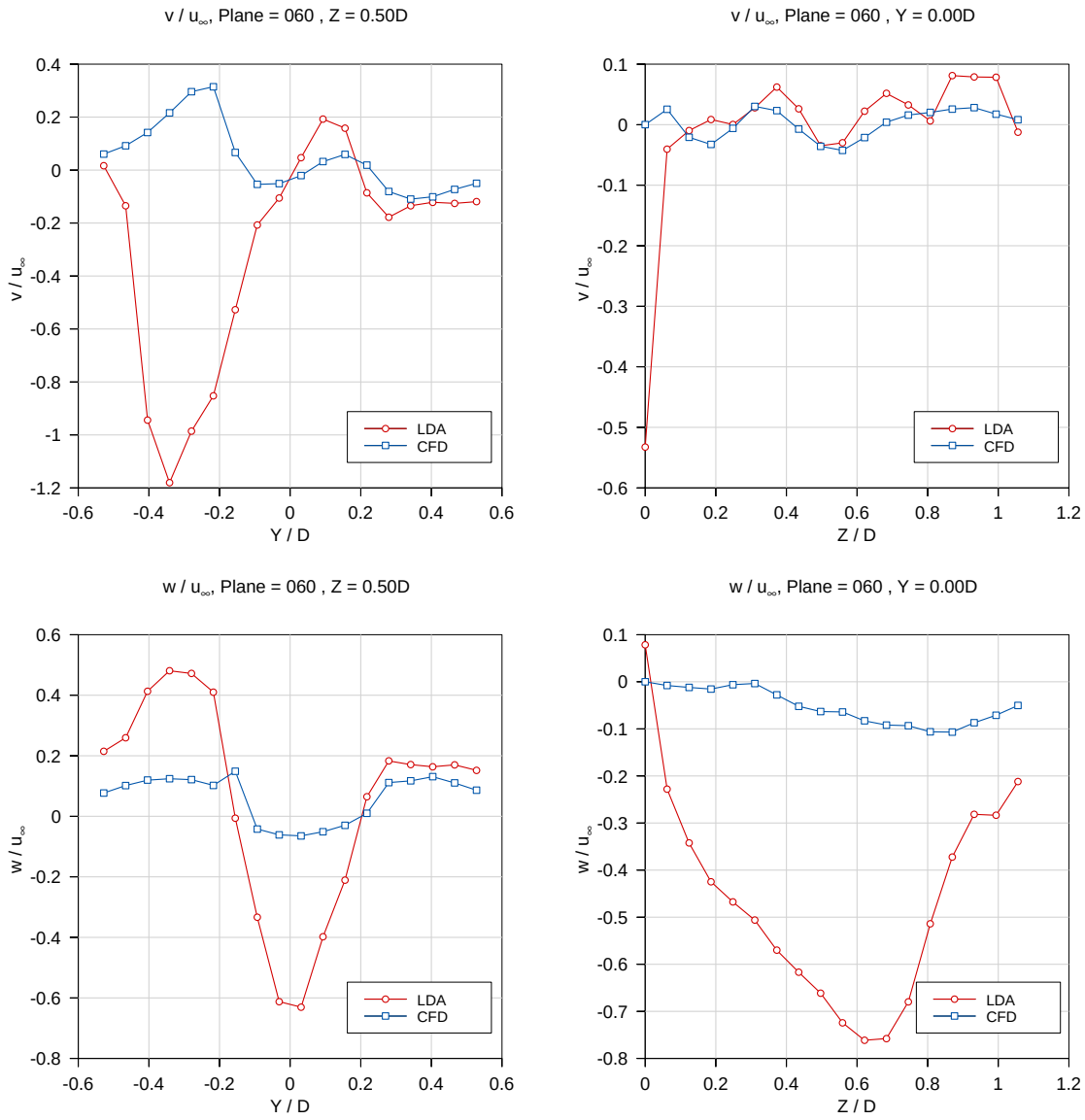

(a) Horizontal Centreline $(Z/D = 0.5)$

(b) Vertical Centreline $(Y/D = 0)$

Figure 6.14: Comparison of LDA & CFD Centreline In-Plane (v–w) Velocity Profiles - 60 % Plane with Sting

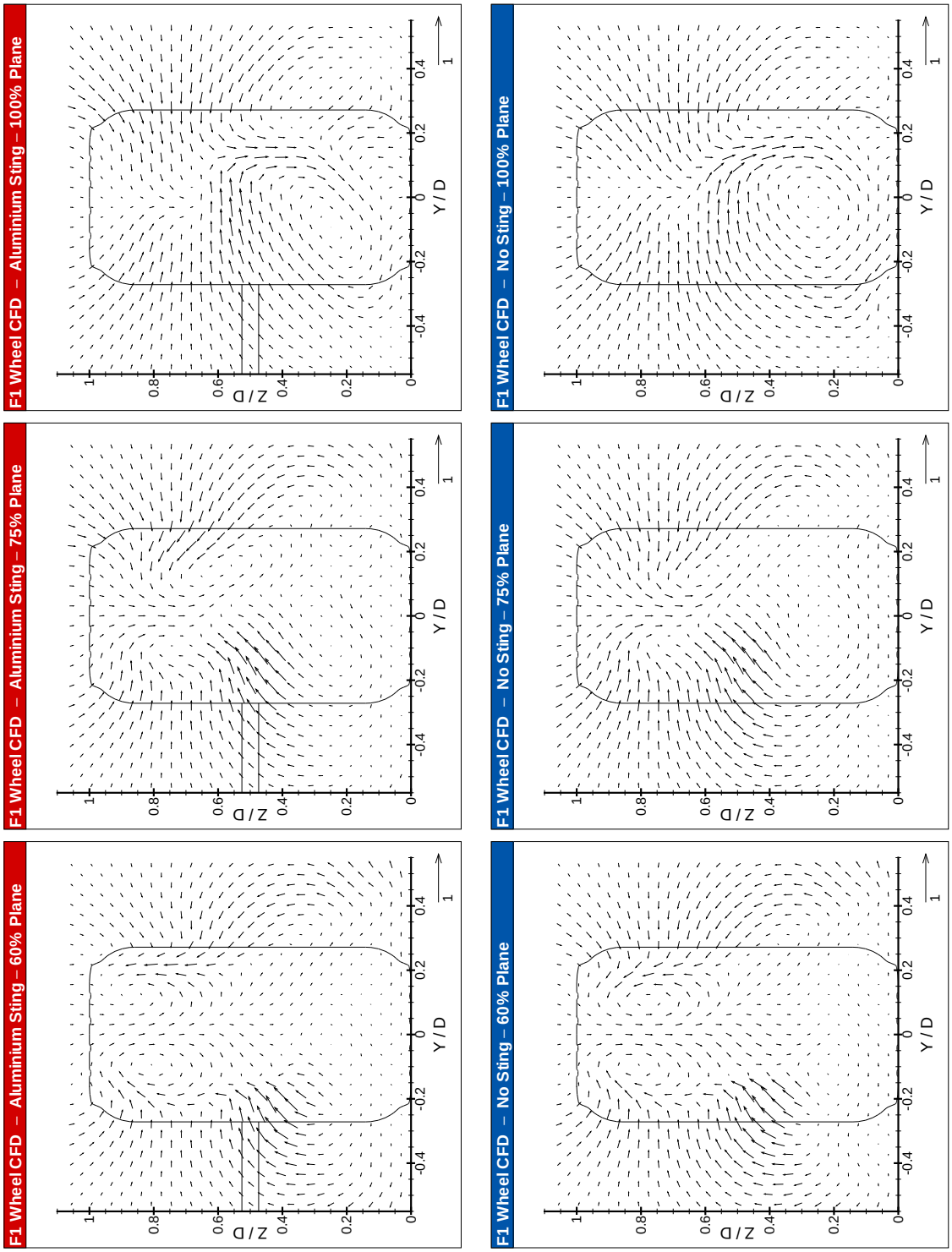

Figure 6.15: Isolated Formula One Wheel – CFD In-Plane (v–w) Velocity Vectors

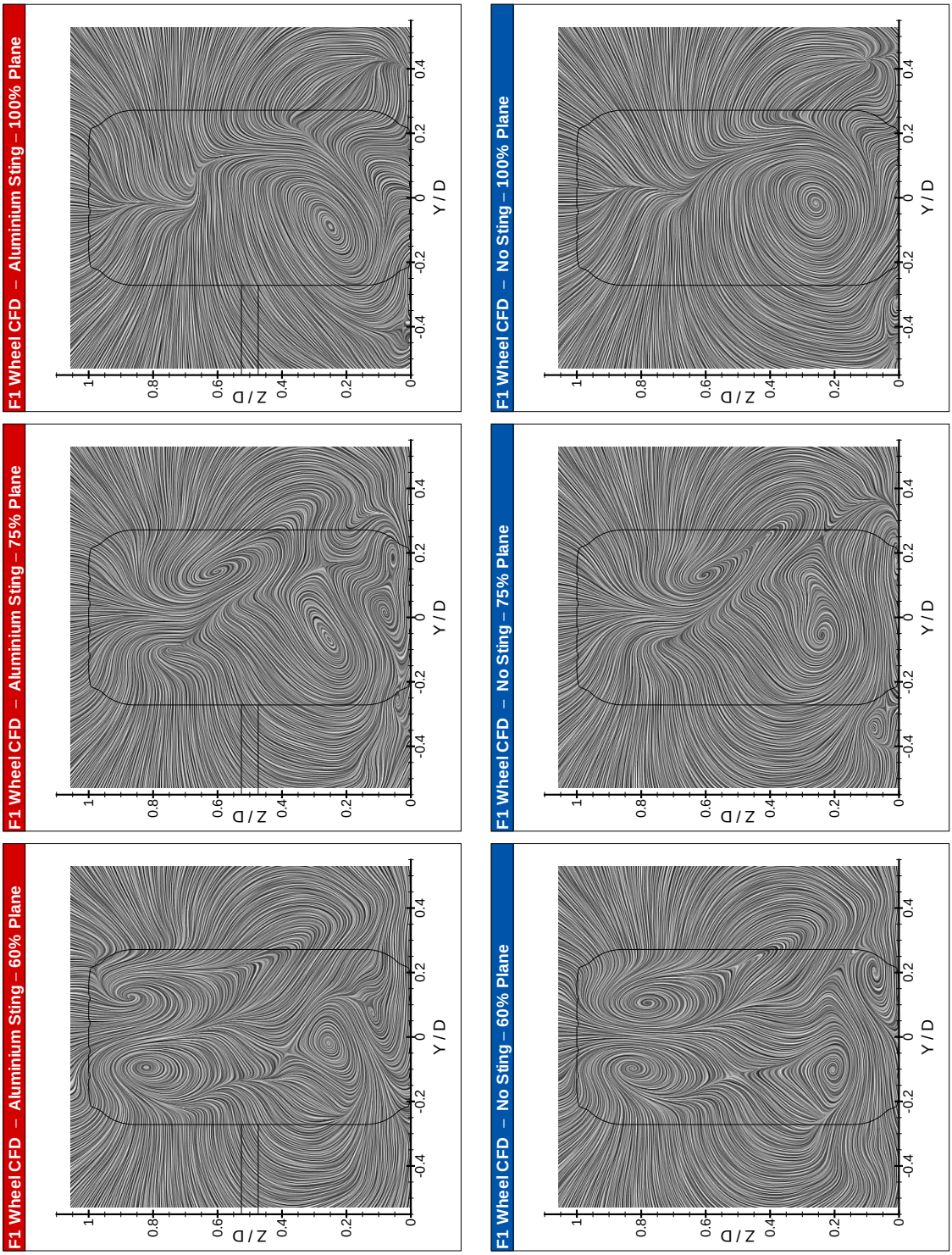

Figure 6.16: Isolated Formula One Wheel – CFD Line Integral Convolution Images

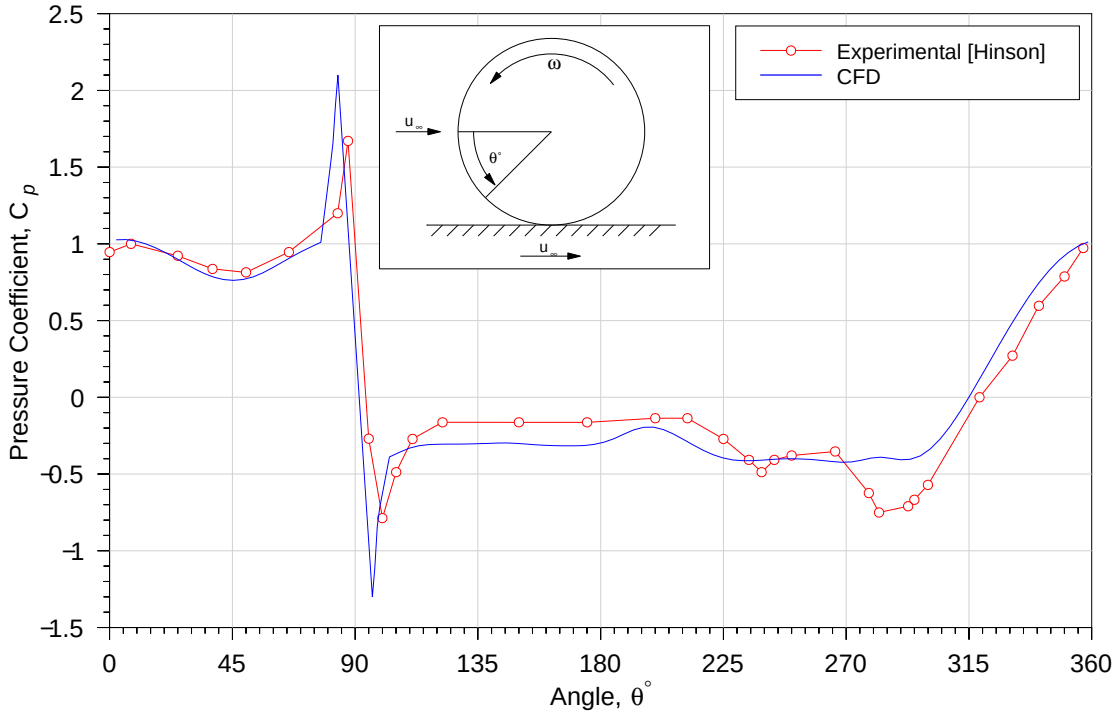

Figure 6.17: Circumferential Pressure Distribution on the Tyre Centreline $(\mathrm{Y/D} = 0)$

Wheel Through-Flow

Inspection of the CFD data once again found that the support sting significantly modified the mass-flow through the wheel. The CFD predicted that presence of the aluminium sting decreased mass-flow through the Formula One wheel by 42 %. In Phase One the same sting was predicted to *increase* the flow through the Champ Car wheel by 98 %. The magnitudes of these changes reinforce the earlier proposal that the aluminium sting had a larger interference effect on 40 %-scale Champ Car components than on the current Formula One components at 50 %-scale. The direction of the change reflects the observation that the net flow through the wheel was from outside to inside in the case of the Champ Car wheel assembly and vice-versa for the Formula One components.

Whilst the direction of the flow through the wheel has reversed from Phase One to Phase Two, the mechanisms behind the sting interference remain the same. Figure 6.18 uses contours of the v-component of velocity (axial with the wheel) to represent the flow entering and leaving the wheel hub and graphically illustrate the change in wheel through-flow. Figures 6.18(a) and (b) are planes located immediately outside the wheel spokes, with and without a support sting respectively. Figures 6.18(c) and (d) are similar planes located at the inside edge of the wheel hub, again with and without support stings. The freestream flow direction is from left to right, as illustrated by the outline of the support sting in Figure 6.18(a).

Comparison of the outer planes confirms that the support sting modifies the flow throughout the plane, especially in its immediate vicinity and in its wake. Its net effect is to reduce the amount

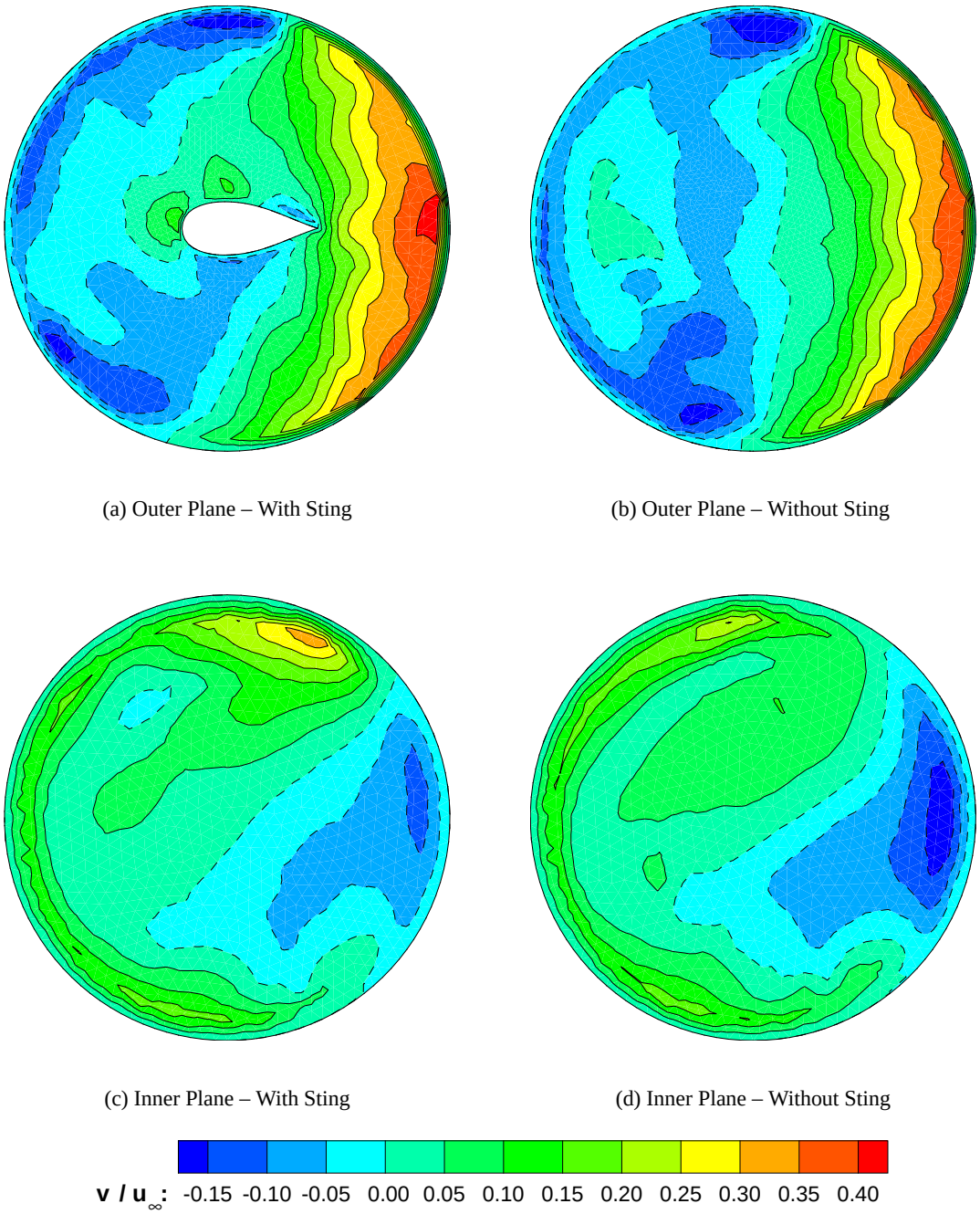

(a) Outer Plane – With Sting

(b) Outer Plane – Without Sting

(c) Inner Plane – With Sting

(d) Inner Plane – Without Sting

Figure 6.18: Axial Velocity (v) Contours on the Inner and Outer Planes of the Wheel Hub (negative regions bounded by dashed lines and directed out of page)

of flow leaving the wheel hub, which in these planes corresponds to negative axial velocity.

As the contours are axial, it follows that on the inner side of the wheel the negative flow is now entering the wheel hub. Just as the sting reduced the flow leaving the outside of the wheel, it also reduces the flow entering through the inner plane. One of the interesting features of this plane is the peak in the region of positive axial velocity (flow leaving) at the top of the hub. In the presence of the sting this peak was intensified and rotated from $\theta \approx 280^\circ$ to around 240°. Further inspection of the CFD data has shown that when the sting is present the flow leaving the hub at around $\theta = 240^\circ$ is entrained along the tyre sidewall into the formation region of the upper-right vortex. It is proposed that it is this interference effect that is responsible for the attenuation of the upper-right vortex noted in the experimental data. The same effect has been found to occur with the Champ Car wheel in the computational results of Phase One. In that case the upper-right vortex was suppressed by the increased entrainment of flow from the wheel hub in the presence of the sting. As the computational data from Phase One provided clearer visualisation of the entrainment of the flow from the hub into the wake, it was used to provide the visualisation shown in Figure 6.19.

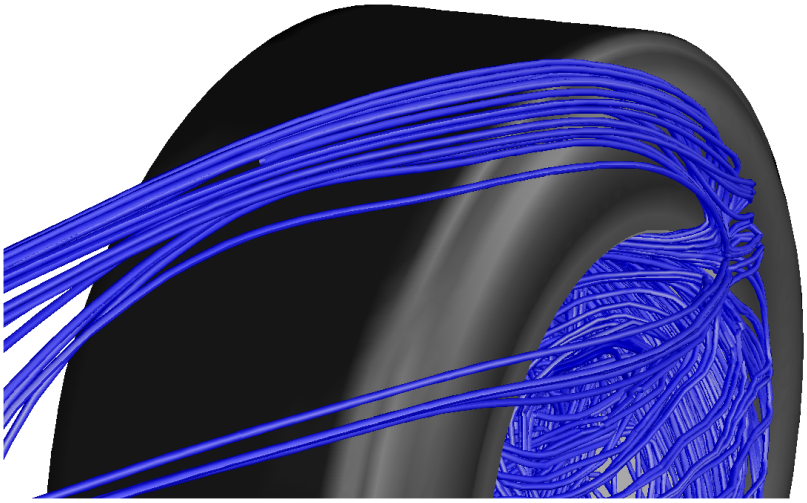

Figure 6.19: Entrainment of Flow from the Wheel Hub into the Wake
(through-flow from left to right) Champ Car Wheel & Aluminium Support Sting

In addition to its impact upon the wheel wake, modification of the wheel through-flow by a support sting will have implications for the design of brake cooling ducts and cooling performance in general.

6.4.3 Wheel-&-Car Data

In this section the effect of the presence of the car will be investigated by comparison of the isolated-wheel results with those collected in the presence of the car. The latter will also be used

to determine the interference effects of the support stings on this modified flowfield. To the best of the author's knowledge this is the first time data of this type have been published.

Mean u-Velocity Contours

The contours in Figure 6.20 exhibit most of the features identified as characteristics of the wake of an isolated wheel. The narrow central section, ground lobes, asymmetry and reversed flow are all in evidence in each test configuration. The presence of the car has, as expected, significantly modified the isolated wheel flow (cf. Figure 6.4). The interference effect of the car will undoubtedly depend upon its configuration; factors such as front wingspan and down-force level can be expected to be critical. From the data gathered several new observations have been made, which apply to all of the tested wheel mountings.

Firstly, the narrow central section of the wake was significantly taller in the presence of the car. In the 75 %-plane with the aluminium sting, the wake was approximately one third taller than in the isolated case. The analysis of the CFD data has shown that increased wake height is indicative of upstream motion of the separation position. This therefore suggests that the presence of the car changes the angle at which flow separates from the tyre $(\theta > 270^{\circ})$.

The ground lobes, although present, were greatly affected by the presence of the car. In the 75 %-planes of Figure 6.20 the right lobe, nearer the car, has been effectively separated from the main body of the wake at $Y/D \approx 0.1$. This separation is also the main feature of the asymmetry in the u-contours. In all cases, and both planes, the lobes are more compact than those measured in the wake of an isolated wheel. As the ground lobes emanate from the disturbance caused by the strong viscous actions in front of the contact patch [12] they are likely to have been reduced by the close proximity of the front wing. However, the interference between the wheel and wing can only be supposed, as its investigation was beyond the scope of this study, requiring tests to have been carried out with and without the front wing.

The presence of the car also affected the reversed flow in the region of the taller wake and the reduced lower lobes. The upper reversed flow in the 75 % plane was been strengthened by the presence of the car, whilst the extension beyond the projected profile, and the magnitude of the lower reversed flow, have been reduced. By the 100 % plane no reversed flow exists, in marked contrast to the isolated wheel. A link was proposed in Chapter 5 between the lower lobes and the reversed flow contained within, from which it would follow that a reduction of the former would also reduce the latter.

Whilst the effect of the car was dramatic, the interference effect of the support stings in the presence of the car was less so. Following inspection of the isolated wheel data it was proposed that the design of the support sting had little effect on the overall shape and extent of the velocity deficit but did impact on the reversed flow and asymmetry. In the presence of the car the sting still modifies the reversed flow but has little impact on the asymmetry, which in this configuration is proposed to be caused by the front wing.

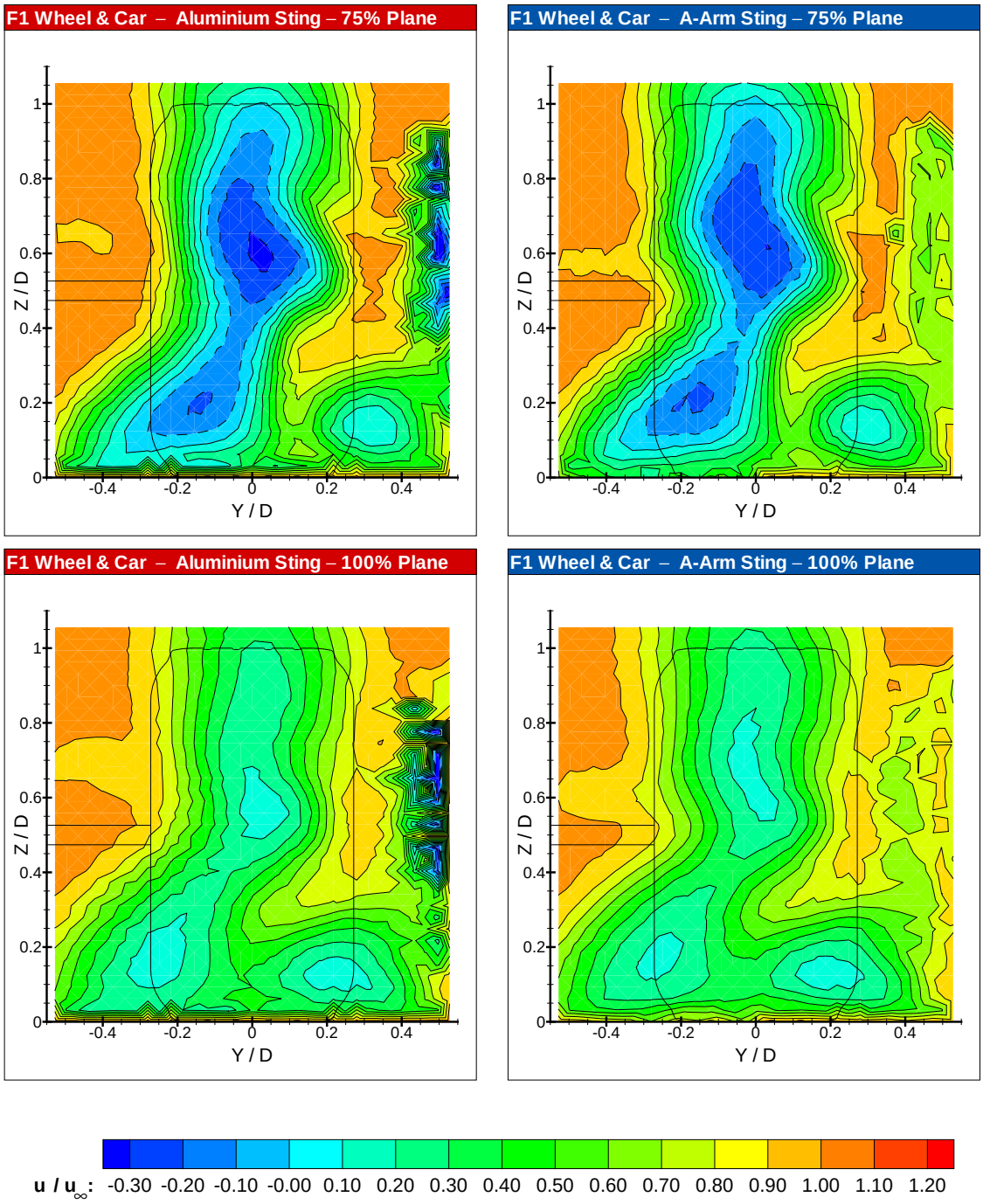

Figure 6.20: Formula One Wheel & Car – Contours of Mean u-Velocity
(negative regions bounded by dashed lines)

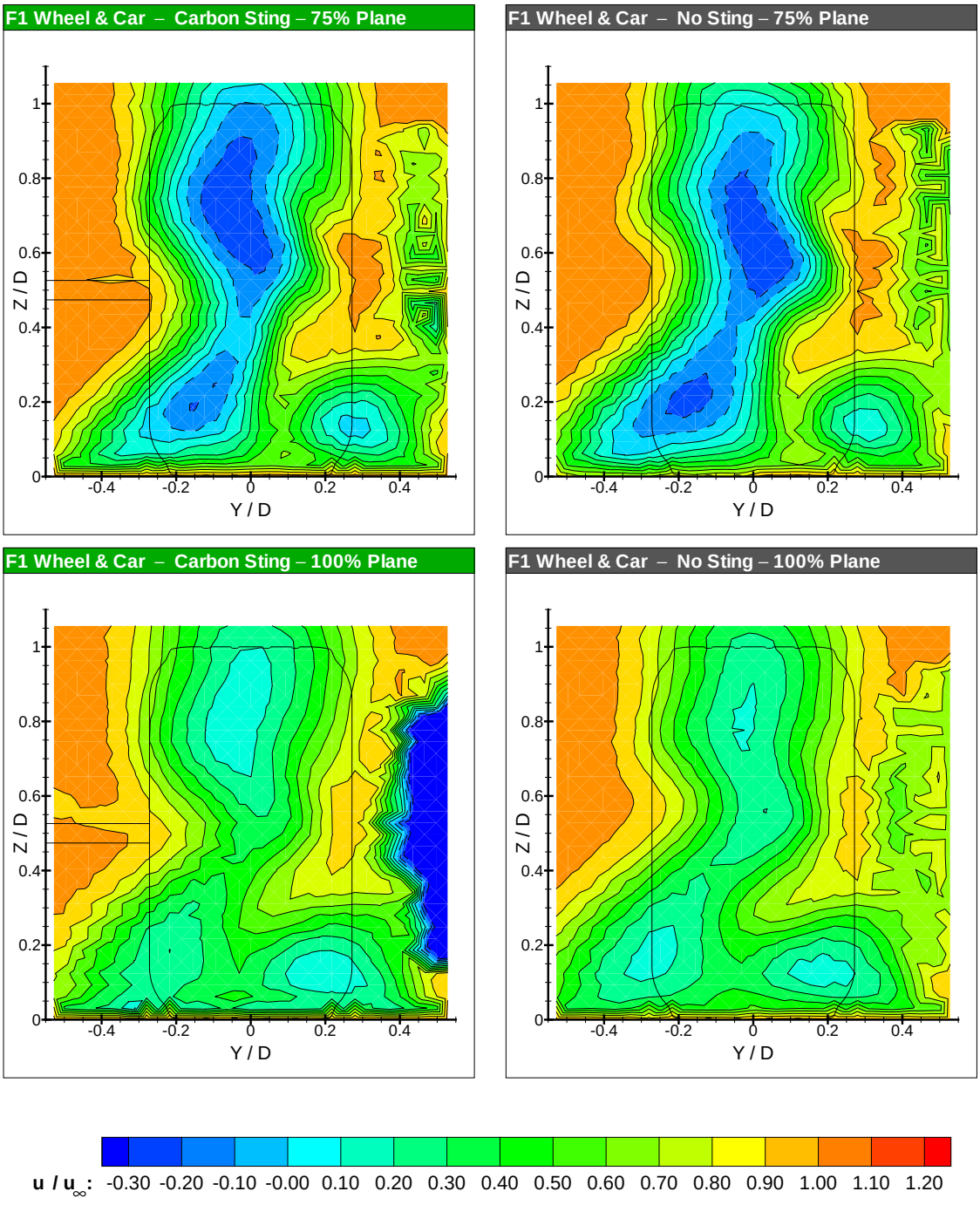

Figure 6.20: (cont.) Formula One Wheel & Car – Contours of Mean u-Velocity (negative regions bounded by dashed lines)

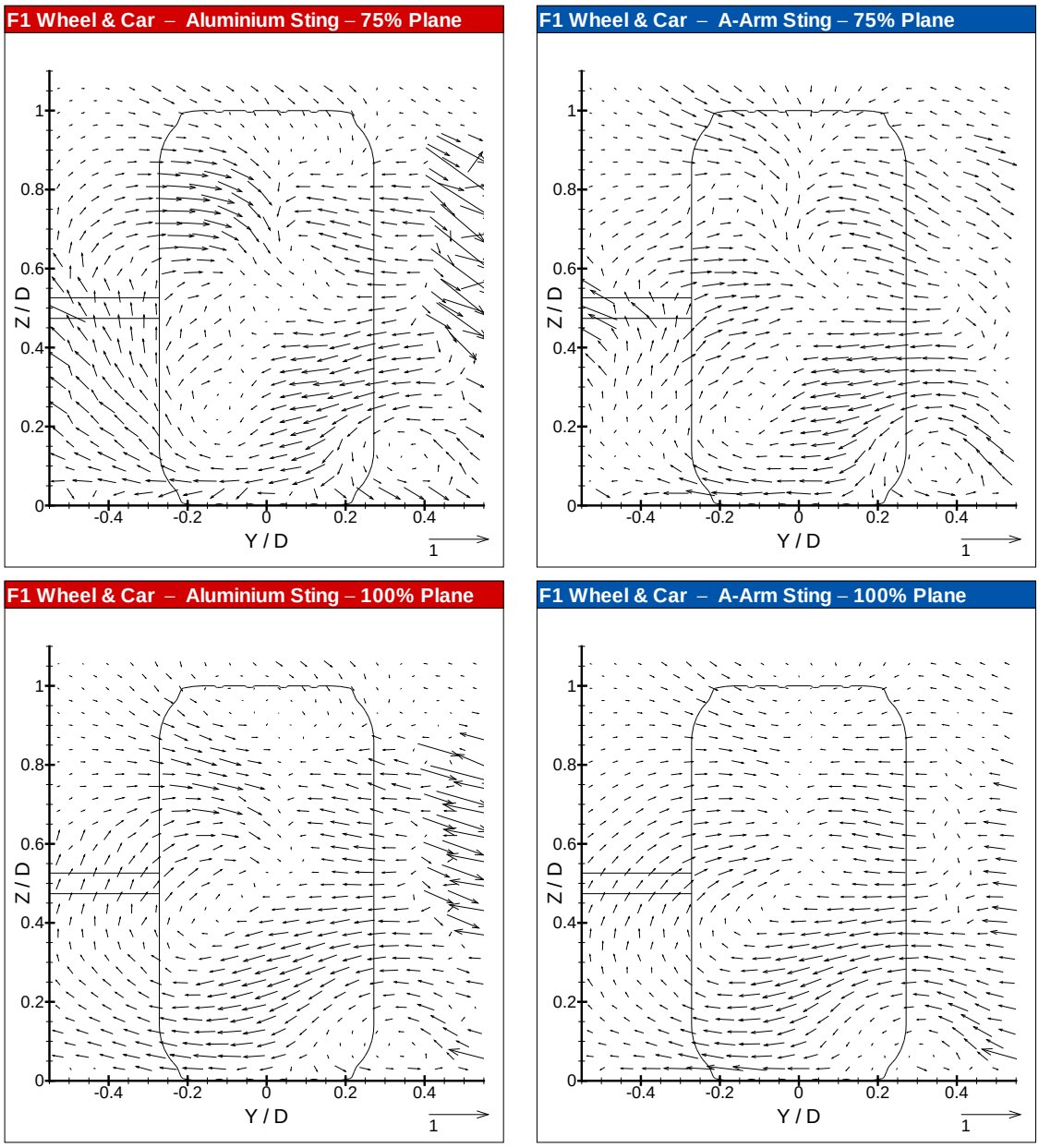

Figure 6.21: Formula One Wheel & Car – In-Plane (v–w) Velocity Vectors

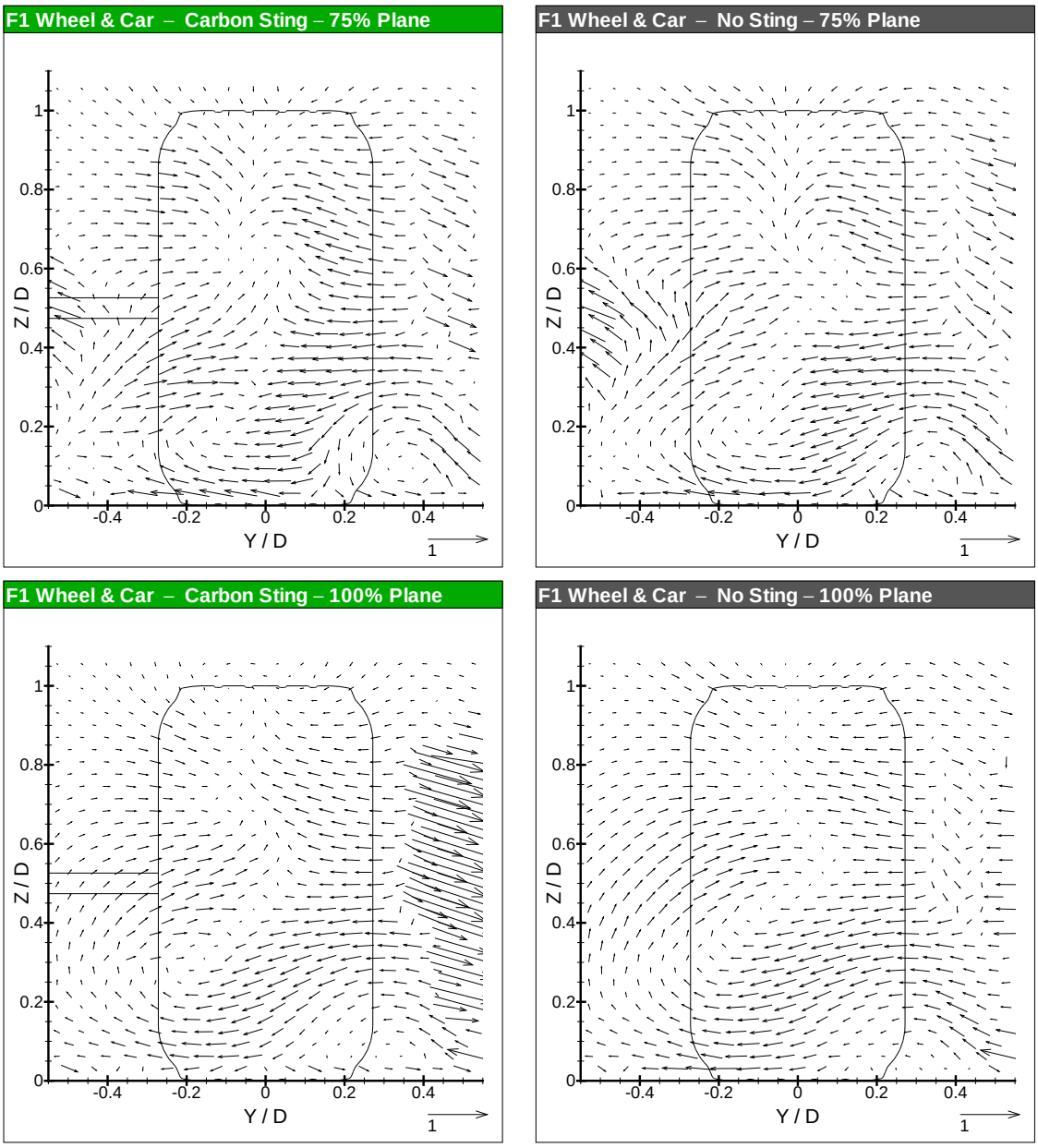

Figure 6.21: (cont.) Formula One Wheel & Car – In-Plane (v–w) Velocity Vectors

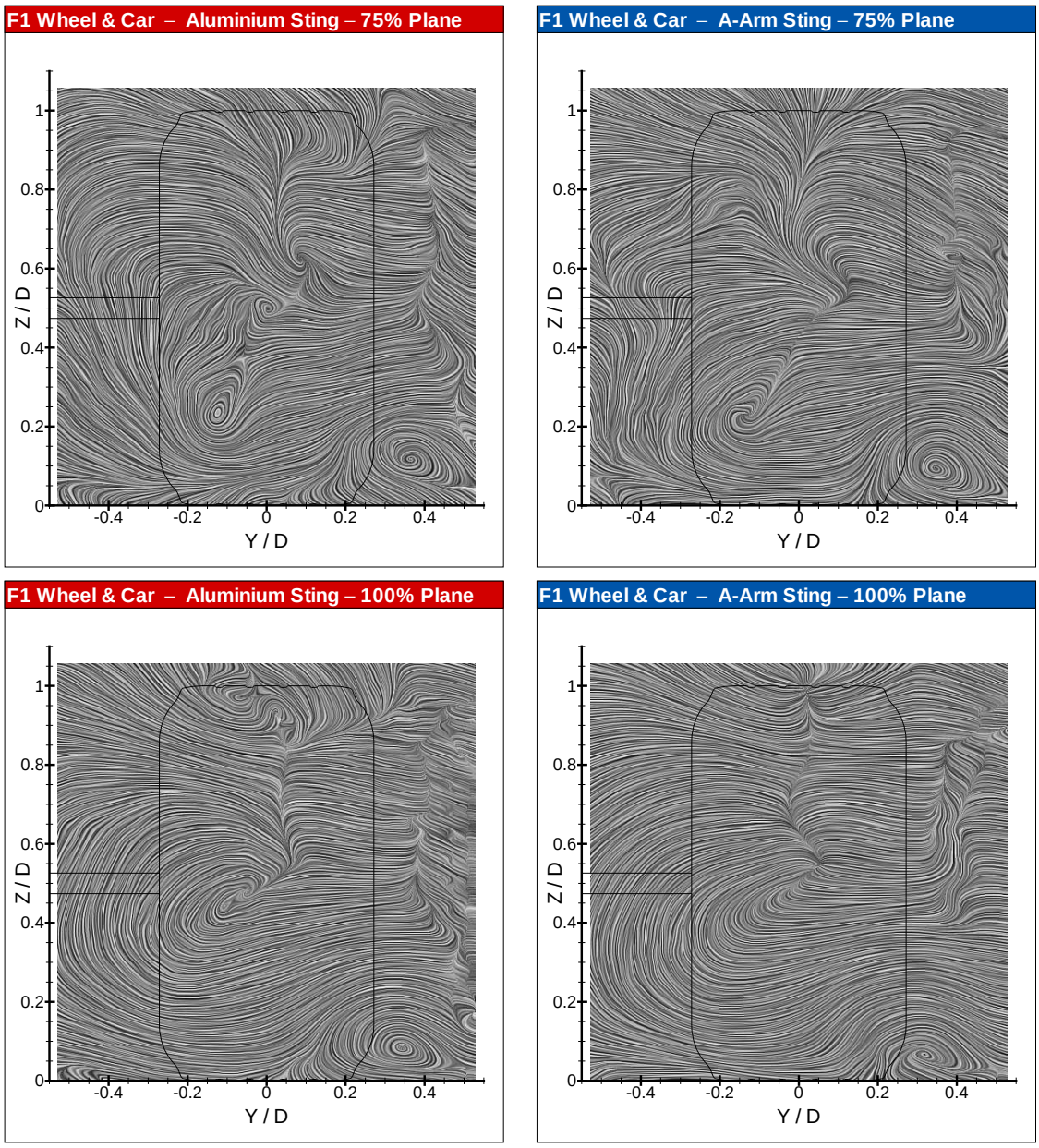

Figure 6.22: Formula One Wheel & Car – Line Integral Convolution Images

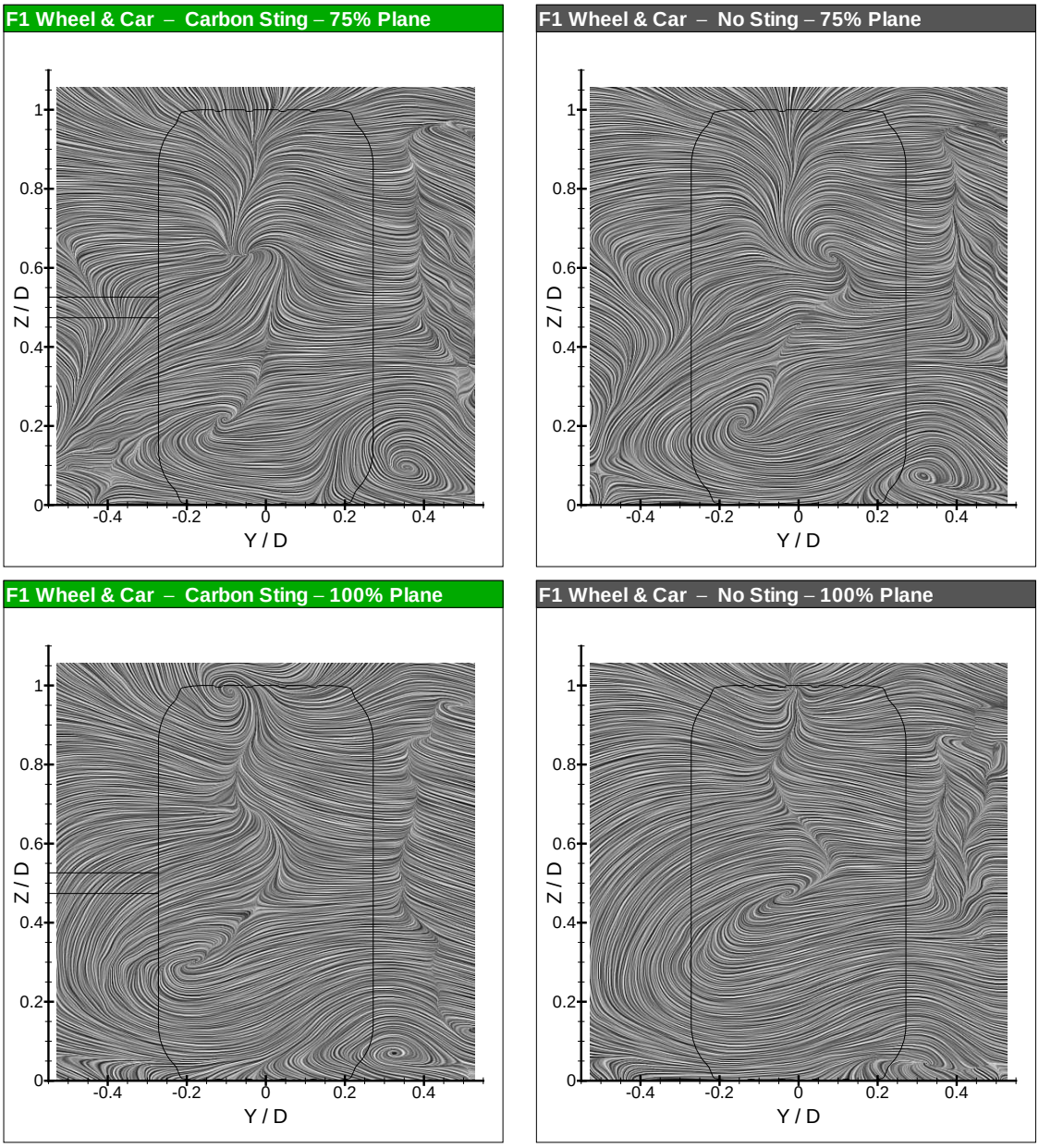

Figure 6.22: (cont.) Formula One Wheel & Car – Line Integral Convolution Images

It has been suggested in this thesis that the modified mass-flow through the wheel, caused by the presence of the sting, is the root of the interference effects observed in the wake. In the presence of the car, the suspension members could be expected to similarly modify the mass-flow through the wheel and, because of their size, act to reduce the interference effects of the support sting. Investigation of this would require testing with and without the suspension members which was beyond the scope of this study.

In-Plane (v–w) Velocity Data

The data presented in Figures 6.21 and 6.22 illustrate the effect of the presence of the car when compared with Figures 6.7 and 6.8 respectively. The differences are even more striking than those of the u-contours. The trailing vortices observed in the near-wake of an isolated wheel are present although they are much less defined. At 0.75D downstream the wake of the wheel in the presence of the car appears to comprise one central-upper, and two ground vortices which, following convection, are reduced to two ground vortices at one wheel-diameter downstream.

Of these features, only the lower-right structure is well defined but much lower and smaller than observed in the isolated wheel wake. The two remaining structures are also of reduced size with the previous large regions of rotating flow replaced by horizontal in-flow (towards $\mathrm{Y/D} = 0$). This results in what appears to be a line-sink from $0.5 < \mathrm{Z/D} < 0.8$, in the 100 %-plane LIC plots of Figure 6.22. There is also no central down-wash region bisecting the plane and allowing the majority of the flow to be entrained into the large left structure. The small, lower-right structure seems to be isolated, having only a localised effect on the overall flow.

The plots of the in-plane velocity data, Figures 6.21 and 6.22, have shown that the presence of a support sting has a similar interference effect on the wheel-and-car combination as on an isolated wheel. The data have revealed that the magnitude and position of the structures are affected not only by the support sting but also by its design. The magnitude of the interference in the presence of the car was reduced when compared with an isolated wheel, which was proposed earlier to be due to the added interference of the suspension members.

Streamwise Turbulence Intensity

As all three components of velocity have shown marked difference in the presence of the car it is unsurprising to find that the distribution of the streamwise turbulence was also altered. Figure 6.23 compares the $\mathrm{Ti_u}$ distribution of the aluminium sting data with and without the car and also the data gathered when the wheel was mounted on the car suspension (no sting).

The effect of the car can be seen by comparing the aluminium sting results. The changes correlate well with those noted in the u-data as the high $\mathrm{Ti_u}$ regions in the presence of the car still correspond with the areas of reversed flow and the trailing vortices along with the line-sink noted in the in-plane data. The distribution is taller and narrower than that of the isolated wheel and concentrated almost exclusively (neglecting regions caused by surface reflections) within

the projected profile. By the final plane the turbulence level has dropped significantly below that observed in the wake of an isolated wheel with only two small regions of high Ti_u remaining.

Comparing the two datasets which were gathered in the presence of the car serves to highlight the effect of the sting on the streamwise turbulence distribution. Without the sting the main points of note were:

- a larger central region of high Ti_u extending beyond the tyre profile at the lower left shoulder;
- reduced intensity in the core of the inside ground vortex;
- reduced turbulence one wheel diameter downstream.

These observations confirm that in addition to its effect on the velocity components in the near-wake, the support sting modified the distribution and intensity of the streamwise turbulence.

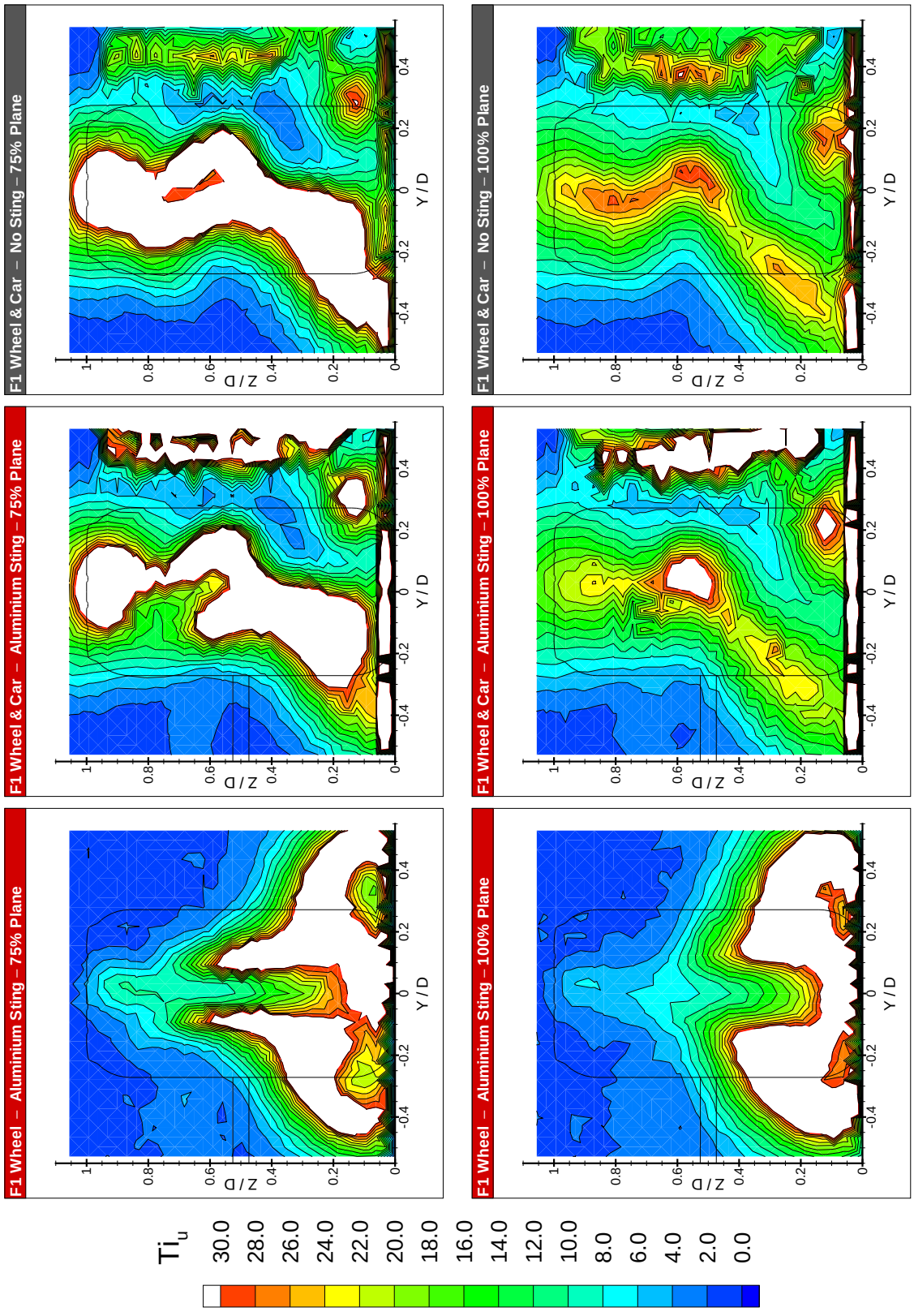

Figure 6.23: Comparison of Streamwise Turbulence Intensity Distribution

7 Conclusions

This chapter presents the overall conclusions of this work as determined by both phases of the investigation. The issues raised and the new areas of investigation opened up by this work are presented as subjects for further examination. The four main objectives attempted to expand the available knowledge base by:

1. identifying the prominent features in the wake of a wheel, which also would allow the disparate wake models in the literature to be re-visited;
2. investigating the qualitative relationship between sting design and interference effect by sequentially analysing three geometrically-different support stings;
3. investigating the flowfield of the wheel in the presence of a car and comparing it with that of an isolated wheel;
4. experimentally evaluating the sting interference effect by testing against a “wheels-on” car configuration.

Wheel Wake

An investigation of the structure of the near-wake of an isolated wheel rotating in ground contact was found to be incomplete in the existing literature. The data gathered in Phases One and Two have been used along with the literature to clarify the near-wake structure. The following features have been highlighted as the main characteristics of such a wake.

- A region of velocity deficit in the shape of an inverted-T, ($\perp$).
- Large regions of reversed flow exist both in the vertical and horizontal sections. In the latter, the regions extend beyond the projected profile of the wheel.
- A trailing vortex system consisting of two contra-rotating vortex pairs, one in the upper half of the wake, and one at ground level.
- All four vortices are centred within, or aligned with, the projected profile of the wheel and have a streamwise axis and thus do not spead laterally up to one wheel diameter downstream.

- The ground vortex pair are larger, more defined and convected further than the upper vortices.

The mechanism by which the reversed flow appears to proceed upstream outside the lee of the wheel has been identified. It is proposed that, just upstream of the contact patch, the convergence of the tyre and road surfaces combine to produce a localised lateral jet on each side of the wheel. The jets deflect the freestream flow as it passes the lower shoulders of the wheel, thus modifying its effective shape (see Figure 5.12 on page 55). It is this deflection that generates the lower lobes and entrains the observed regions of reversed flow.

The two independent and contradictory models of the wheel trailing-vortex system from the literature have been re-visited and revised. Figure 7.1 shows the two original models, 7.1(a) by Cogotti [10] and 7.1(b) by Merker and Berneburg [17]. Each arrow on the models represents the projection of a streamwise trailing vortex in a plane close to the wheel, and indicates their size and rotational sense. Both of these models were based solely on consideration of vortex theory and not on experimental work. The revised model shown in 7.1(c) is based on the experimental data gathered in both phases of the current work and reflects the previously-noted characteristics of an isolated wheel.

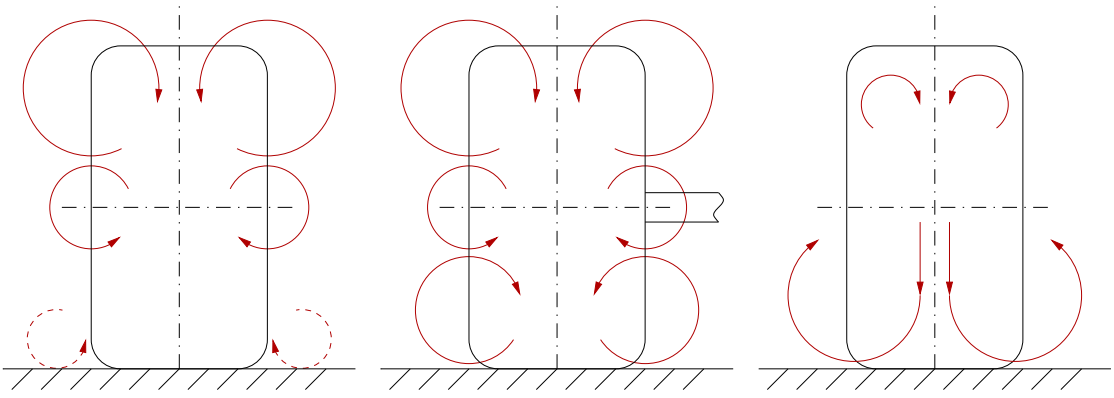

(a) After Cogotti [10]

(b) After Merker and Berneburg [17]

(c) Revised Model

Figure 7.1: Models of the Trailing-Vortex System Induced By a Wheel Rotating on the Ground

The wake of an isolated wheel was observed to exhibit some asymmetry about the $Y/D = 0$ centreline. The revised wake model of Figure 7.1(c) is intended to represent a generic wheel and as such does not include asymmetry, which was found to be strongly dependent upon the particular test components.

Sting Interference Effects – Isolated Wheel

The initial conclusions of Phase One regarding the interference effect of the support sting have been modified following analysis of the Formula One experimental results in Phase Two. The

published data regarding the interference effect of wheel support stings has been significantly extended by this work. In particular the combined results of the two phases have produced the following proposals for the specific effects of the presence of a support sting. The sting was found to modify:

- the mass-flow through the wheel hub;
- the location and definition of the vortical structures, especially the upper pair;
- the location, extent and magnitude of the reversed flow.

The computational models were used to provide insight into the flow around an unsupported wheel and a strong link was found between the change in mass-flow and the interference with the upper vortices. It is proposed that the sting increases the amount of flow discharged from the inside of the hub, which is in turn entrained into the formation region of the upper-right vortex. The magnitude of the effect was experimentally observed to range from vortex suppression in the case of the 40 %-scale Champ Car wheel, to vortex attenuation in the case of the 50 %-scale Formula One wheel.

The sting was found to have little impact on the overall shape and extent of the wake, nor on its convection.

Interference Effects in the Presence of a Car

The fundamental isolated wheel investigations have been extended in the second phase of this work to the more usual context of a wheel in the proximity of a car. The flow surrounding an exposed monoposto racecar wheel has, to the best of the author's knowledge, not been reported in the literature since the very early work of Stapleford and Carr [9] in 1970.

Phase Two of the current work has observed that the previously-outlined, main characteristics of the wake of an isolated wheel can also be found in the presence of the car. The magnitude to which the wake of the wheel on the car differs from an isolated wheel can be expected to depend on the specific geometry and configuration of the car.

The main effects of the Jaguar R1 model were found to be:

- modification of the in-plane velocity components, reducing both the rotation and down-wash present in the wake;
- reduction in the convection of the regions of reversed flow; no upstream flow was observed at one wheel diameter downstream of the wheel in the presence of the car;
- alteration of the angle of flow separation from the tyre ($\theta > 270^{\circ}$), as indicated by the taller and wider central section of the wake.

Sting Interference Effects – Wheel & Car

The wheel support sting was found to exhibit the same interference effects on the wheel in the presence of the car as for the isolated wheel, but to a lesser extent. It is suggested that the reduced interference was caused by the car suspension members. It is hypothesised that these struts modify the wheel through-flow in a similar manner to that of the support sting, but acting opposite to, and thus reducing, the sting interference.

7.1 Recommendations for Future Work

The review of the literature and the results presented in this work have shown that the aerodynamics of a wheel rotating in ground contact is an experimentally and computationally challenging area of investigation. The contributions made by this work have gone some way to furthering the understanding of this complex flow but have also identified several areas beyond the scope of the present project as targets for future investigation.

Isolated Wheels

The non-intrusive nature of laser flow measurement should be exploited to investigate the dominant features of wheel flows, such as the separation and contact patch regions. Measurements made in the separation zone could be used to validate the proposition made by Fackrell [12] that flow separation occurred above the tyre surface. Measurement of the contact patch jet and the flow around the lower shoulders of the tyre would provide the currently-missing link between the wake of the wheel and the mechanisms proposed to generate its distinctive shape.

Support Sting Interference

Experimental data are required to validate a proposal of this work, based on computational data, that the support sting modifies the mass-flow through the wheel. Experimental measurement of the axial velocity at the inner and outer planes of the wheel would be difficult, especially for laser-based techniques. Optical access, particularly to the inner side of the wheel, and the proximity of the surface of the hub to the measurements at the outer plane, would be the main problems encountered if LDA were used. An indication of the effect of the support sting on mass-flow through the wheel could be achieved by the use of a pressure-tapped upright or brake disc. A configuration such as this could subsequently be used to determine the effect of modifications to a sting in an attempt to reduce its interference effect.

The suspension of a model car could be modified to measure the drag of the wheel and the system used to evaluate the effect of sting design on wheel drag. A combination of this system with a pressure-tapped upright/brake disc could be used to perform a complementary study to the work presented in the previous chapters.

Wheel & Car Combination

A pressure-tapped upright or brake disc could also be used to validate the proposal that the suspension members of the car also modify the mass-flow through the wheel. Other areas of interest would include the interaction between the wheel and the front wing, with particular reference to the design of the wing end-plate. With the car in a “wheels-on” configuration measurements could be made in front of and in the wake of the wheel, with and without the front wing. Instrumented suspension could be used to determine the effect of the wing on wheel forces and whether the end-plate could be optimised to reduce the considerable drag of the wheel.

References

[1] P. G. Wright. *Ferrari Formula 1: Under the Skin of the Championship-Winning F1-2000*. Society of Automotive Engineers, Warrendale, PA, 2004.

[2] R. T. Griffiths and C. Y. Ma. Differential bounday-layer separation effects in the flow over a rotating cylinder. *The Aeronautical Journal of the Royal Aeronautical Society*, 73:524–526, June 1969.

[3] S. C. Clark. *An Investigation of the Flow Around a Rotating Cylinder Near the Critical Reynolds Number*. MSc thesis, Cranfield University, 1975.

[4] ESDU. Mean forces, pressures and moments for circular cylindrical structures: Finite-length cylinders in uniform and shear flow. Data Item 81017, Engineering Sciences and Data Unit, London, UK, 1987.

[5] P. W. Bearman and M. M. Zdravkovich. Flow around a circular cylinder near a plane boundary. *Journal of Fluid Mechnics*, 89(1):33–47, 1978.

[6] A. E. Perry and M. S. Chong. A description of eddying motions and flow patterns using critical-point concepts. *Ann. Rev. Fluid Mech.*, 19:125–155, 1987.

[7] J. M. Délery. Robert Legendre and Henri Werlé: Towards the Elucidation of Three-Dimensional Separation. *Ann. Rev. Fluid Mech.*, 33:129–154, 2001.

[8] A. Morelli. Aerodynamics actions on an automobile wheel. In *Proc. of 1st Symposium on Road Vehicle Aerodynamics*, Paper 5, City University, London, Nov. 1969.

[9] W. R. Stapleford and G. W. Carr. Aerodynamic characteristics of exposed rotating wheels. Report 1970/2, Motor Industry Research Association, Nuneaton, UK, 1970.

[10] A. Cogotti. Aerodynamic characteristics of car wheels. *Int. J. of Vehicle Design*, Technological Advances in Vehicle Design Series, SP3, *Impact of Aerodynamics on Vehicle Design*, pages 173–196, 1983.

[11] J. E. Fackrell and J. K. Harvey. The flow field and pressure distribution of an isolated road wheel. In *Advances in Road Vehicle Aerodynamics*, Paper 10, pages 155–165. BHRA Fluids Engineering, Cranfield, UK, 1973.

[12] J. E. Fackrell. *The Aerodynamics of an Isolated Wheel Rotating in Contact with the Ground*. PhD thesis, University of London, 1974.

[13] J. E. Fackrell and J. K. Harvey. The aerodynamics of an isolated road wheel. In *Proc. of AIAA 2nd Symposium on Aerodynamics and Competition Automobiles*, volume 16, pages 119–125, Los Angeles, CA, 1974.

[14] J. E. Hackett, J. B. Baker, J. E. Williams, and S. B. Wallis. On the influence of ground movement and wheel rotation in tests on modern car shapes. Technical Paper 870245, Society of Automotive Engineers, Warrendale, PA, 1987.

[15] P. W. Bearman, D. De Beer, E. Hamidy, and J. K. Harvey. The effect of a moving floor on wind-tunnel simulation of road vehicles. Technical Paper 880245, Society of Automotive Engineers, Warrendale, PA, 1988.

[16] E. Merker, N. Breuer, H. Berneburg, and H. J. Emmelmann. On the aerodynamic interference due to the rotating wheels of passenger cars. Technical Paper 910311, Society of Automotive Engineers, Warrendale, PA, 1991.

[17] E. Merker and H. Berneburg. On the simulation of road driving of a passenger car in a wind tunnel using a moving belt and rotating wheels. In *Proc. of 3rd Int. Conf. Innovation and Reliability*, Florence, Italy, April 8–10 1992.

[18] J. Wildi. Wind tunnel testing of racing cars – The importance of the road simulation technique. In *Proc. of RAeS Conf. on Wind Tunnels and Wind Tunnel Testing*, Southampton, UK, September 1994.

[19] R. Mueller, N. Singer, and W. Eckert. Moving belt with distributed suction in the Porsche model wind tunnel. Technical Paper 1999-01-0650, Society of Automotive Engineers, Warrendale, PA, 1999.

[20] M. Hinson. *Measurement of the Lift Produced by an Isolated, Rotating Formula One Wheel Using a New Pressure Measurement System*. MSc thesis, Cranfield University, 1999.

[21] A. P. Mears, R. G. Dominy, and D. B. Sims-Williams. The flow about an isolated rotating wheel – Effects of yaw on lift, drag and flow structure. In *Proc. of 4th MIRA International Vehicle Aerodynamics Conference*, Warwick, UK, 2002.

[22] A.P. Mears, R. G. Dominy, and D. B. Sims-Williams. The air flow about an exposed racing wheel. Technical Paper 2002-01-3290, Society of Automotive Engineers, Warrendale, PA, 2002.

[23] A. P. Mears, S. C. Crossland, and R. G. Dominy. An investigation into the flow-field about an exposed racing wheel. Technical Paper 2004-01-0446, Society of Automotive Engineers, Warrendale, PA, 2004.

[24] A. P. Mears and R. G. Dominy. Racing car wheel aerodynamics – Comparisons between experimental and CFD derived flow-field data. Technical Paper 2004-01-3555, Society of Automotive Engineers, Warrendale, PA, 2004.

[25] R. Knowles, A. Saddington, and K. Knowles. On the near wake of rotating, 40%-scale Champ Car wheels. *SAE 2002 Transactions - Journal of Passenger Cars: Mechanical Systems*, 6:2245–2253, 2002.

[26] A. R. Purvis. *The Wake Behind a Deformable Racing Tyre*. MSc thesis, Cranfield University, 2003.

[27] L. Axon, K. P. Garry, and J. Howell. An evaluation of CFD for modelling the flow around stationary and rotating isolated wheels. Technical Paper 980032, Society of Automotive Engineers, Warrendale, PA, 1998.

[28] L. Axon. *The Aerodynamic Characteristics of Automobile Wheels – CFD Prediction and Wind Tunnel Experiment*. PhD thesis, Cranfield University, 1999.

[29] L. Axon, K. P. Garry, and J. Howell. The influence of ground condition on the flow around a wheel located within a wheelhouse cavity. Technical Paper 1999-01-0806, Society of Automotive Engineers, Warrendale, PA, 1999.

[30] A. F. Skea, P. R. Bullen, and J. Qiao. The use of CFD to predict the air flow around a rotating wheel. In *Proc. of 2nd MIRA International Conference on Vehicle Aerodynamics*, Birmingham, UK, October 1998.

[31] A. F. Skea, P. R. Bullen, and J. Qiao. CFD simulations and experimental measurements of the flow over a rotating wheel in a wheel arch. Technical Paper 2000-01-0487, Society of Automotive Engineers, Warrendale, PA, 2000.

[32] B. Basara, D. Beader, and V. P. Przulj. Numerical simulation of the air flow around a rotating wheel. In *Proc. of 2nd MIRA International Conference on Vehicle Aerodynamics*, Birmingham, UK, October 1998.

[33] A. Wäschle, S. Cyr, T. Kuthada, and J. Wiedermann. Flow around an isolated wheel – Experimental and numerical comparison of two CFD codes. Technical Paper 2004-01-0445, Society of Automotive Engineers, Warrendale, PA, 2004.

[34] A. Cogotti and F. De Gregorio. Presentation of flow field investigation by PIV on a full-scale car in the Pininfarina wind tunnel. Technical Paper 2000-01-0870, Society of Automotive Engineers, Warrendale, PA, 2000.

[35] J. E. Nigbur. *Characteristics of the Wake Downstream of an Isolated Automotive Wheel*. MSc thesis, Cranfield University, 1999.

[36] W. F. Milliken and D. L. Milliken. *Racecar Vehicle Dynamics*. Society of Automotive Engineers, Warrendale, PA, 1995.

[37] W-H. Hucho, editor. *Aerodynamics of Road Vehicles*. Society of Automotive Engineers, Warrendale, PA, 4^{th} edition, 1998.

[38] J.B. Barlow, W.H. Rae, and A. Pope. *Low Speed Wind Tunnel Testing*. John Wiley and Sons, New York, NY, 1999.

[39] G. S. Taylor, I. Gursul, and D. I. Greenwell. Static hysteresis of vortex breakdown due to support interference. In *Proc. of 19th Applied Aerodynamics Conference*, Anaheim, CA, June 2001. AIAA.

[40] G. S. Taylor, I. Gursul, and D. I. Greenwell. An investigation of support interference in high angle of attack testing. *Journal of Aircraft*, 40(1):143–152, 2003.

[41] M. Page, J. Winkler, N. Roberts, T. Huschilt, D. Smyth, and B. Kane. Recent upgrades to the Swift 8ft×9ft rolling-road wind tunnel. Technical Paper 02MSEC-85, Society of Automotive Engineers, Warrendale, PA, 2002.

[42] B. Hetherington and D. B. Sims-Williams. Wind tunnel model support strut interference. Technical Paper 2004-01-0806, Society of Automotive Engineers, Warrendale, PA, 2004.

[43] R. Peikert. Linear 2D vector fields. http://graphics.ethz.ch/ peikert/personal/Linear2D.

[44] B. Cabral and L. C. Leedom. Imaging vector fields using line integral convolution. In *Proc. of SIGGRAPH '93*, Anaheim, CA, August 1993.

[45] N. J. Lawson, M. V. Finnis, J. A. Tatum, and G. M. Harrison. Combined Particle Image Velocimetry and Line Integral Convolution Methods: Application to a Sphere Sedimenting Near a Wall in a Non-Newtonian Fluid. Submitted to Journal of Visualization, 2005.

[46] R. Lewis and P. Postle. CFD validation for external aerodynamics. In *Proceedings of the 1st European Automotive CFD Conference*, Bingen, Germany, June 2003.

[47] C. Bienz, T. Larsson, T. Sato, and B. Ullbrand. In front of the grid - CFD at Sauber Petronas F1: Leading the aerodynamic development. In *Proceedings of the 1st European Automotive CFD Conference*, Bingen, Germany, June 2003.

[48] R. P. Dring. Sizing criteria for laser anemometry particles. *ASME Journal of Fluids Engineering*, 104:15–17, March 1982.

[49] P. Buchave, W. K. George Jr, and J. L. Lumley. The measurement of turbulence with the laser-Doppler anemometer. *Ann. Rev. Fluid. Mech.*, 11:443–503, 1979.

[50] L. H. Benedict and R. D. Gould. Uncertainty estimates for any turbulence statistics. In *Proc. of the 8th Int. Symp. of. Applications of Laser Techniques to Fluid Mechanics*, Instituto Superior Técnico, Lisbon, Portugal, 1996.

[51] Dantec Dynamics A/S. Statistical stop criteria in BSA flow software. Product Information 189, Denmark, 2004.

[52] H. Nobach. A global concept of autocorrelation and power spectral density estimation from LDA data sets. In *Proc. of the* 10^{th} *Int. Symp. of. Applications of Laser Techniques to Fluid Mechanics*, Instituto Superior Técnico, Lisbon, Portugal, 2000.

A Wind Tunnel Specifications

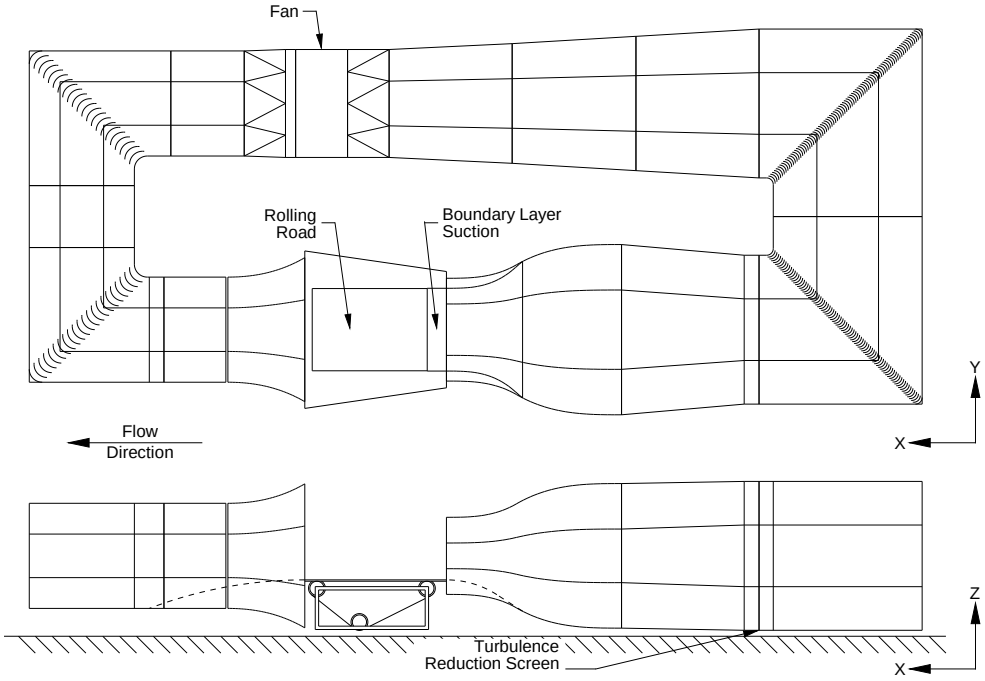

Open-Jet Wind Tunnel (OJWT)

Type	Closed Circuit, 3/4 Open-Jet with Rolling Road
Contraction Ratio	3.31:1
Nozzle Dimensions	$1.52\text{m} \times 1.14\text{m}$
Max. Flow Speed	35ms^{-1}
Boundary Layer Thickness ($\delta_{99\%}$)	5.7mm @ wheel test location
Wind Speed Error	$< 1\%$
Turbulence Intensity	$\approx 0.75\%$
Turbulence Reduction Screens	$2\times$ 55%-Open Area, Wire Mesh
Max. Rolling Road Speed	20ms^{-1}
Temperature Control	N/A
Force Balance	3 Component, Overhead Electro-Mechanical

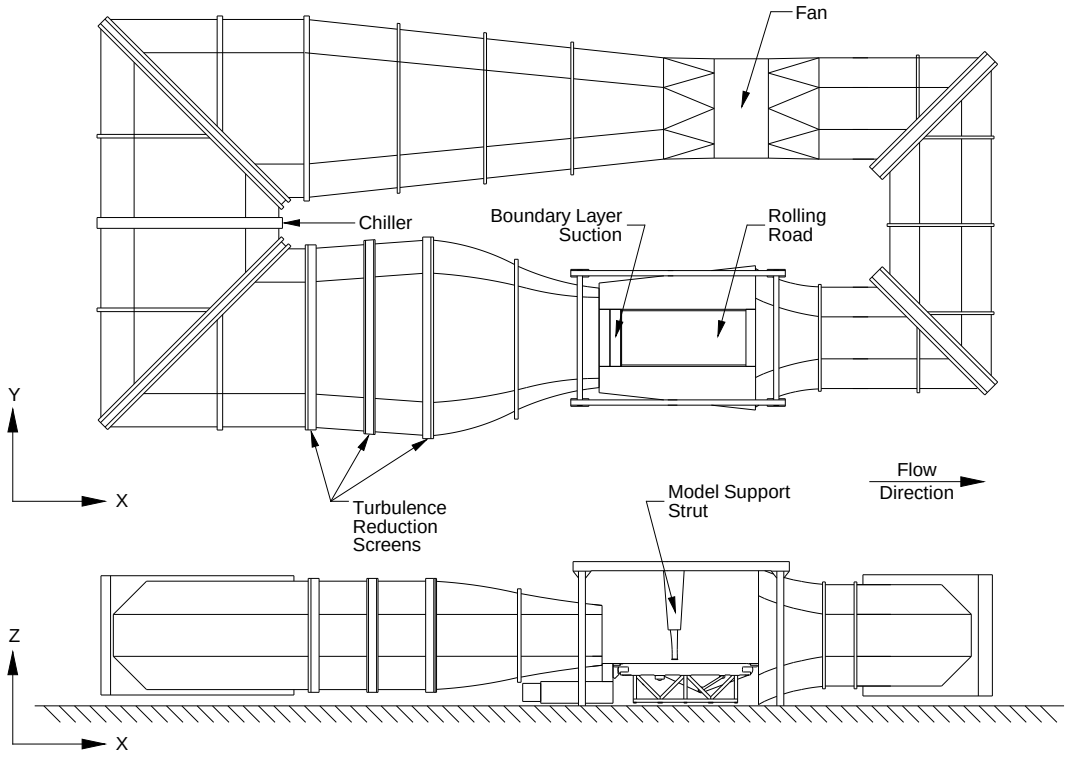

D. S. Houghton Wind Tunnel

Type		Closed Circuit, 3/4 Open-Jet with Rolling Road
Contraction Ratio		3.31:1
Nozzle Dimensions		$2.75\text{m} \times 1.4\text{m}$
Max. Flow Speed		42ms^{-1}
Boundary Layer Thickness		1.5mm @ wheel test location
Wind Speed Error		$< 0.2\%$
Turbulence Intensity		$\approx 0.25\%$
Turbulence Reduction Screens		$3\times$ 53%-Open Area, Wire Mesh
Max. Rolling Road Speed		50ms^{-1}
Temperature Control	Air	$\pm 0.5^{\circ}$C via 400kW Cooling Circuit
	Road	$\pm 0.5^{\circ}$C via 150kW Cooling Circuit
Force Balance		6-Component, Internal-to-Model

B Experimental Summary

	Phase One	Phase Two	
		Isolated	Wheel+Car
Test Components			
Wheel	Champ Car	Formula One	
Scale (%)	40	50	
Diameter (m)	0.263	0.322	
Width (m)	0.120	0.175	
Aspect Ratio	0.456	0.543	
Grooves	×	✓	
Brake Rotor	✓	✓	
Suspension Upright	×	✓	
Wheel Mounting			
Aluminium Sting	✓	✓	✓
A-Arm Sting	×	✓	✓
Carbon Sting	×	✓	✓
Car Suspension	×	×	✓
Test Configuration			
Wind Tunnel	OJWT	D.S. Houghton	
Wind & Road Speed (ms^{-1})	20	30	
Reynolds No. (based on D)	3.7×10^5	6.8×10^5	
Wheel/Nozzle Area-Blockage (%)	2.6	1.4	
Boundary Layer Suction (%)			
Primary	0	40.3	
Secondary	100	64.2	
Belt Suction	75	54.4	

	Phase One		Phase Two	
			Isolated	Wheel+Car
Laser Doppler Anemometer				
Probe Orientation				
U-Component (nm)	488		514.5	
V-Component (nm)	478.5		514.5	
W-Component (nm)	514.5		514.5	
Probe Settings	**U & W**	**V**	**U, V & W**	
Focal Length (mm)	1000	1000	2500	
Beam Diameter (mm)	2.2	2.2	2.2	
Expander Ratio	1.98	1.98	2.97	
Beam Spacing (mm)	37.4	37.4	36.5	
Meas. Vol. Major Diameter (mm)	4.1	3.8	11.6	
Off-Axis Angle (°)				
U-Component	0		0	
V-Component	34.33		45	
W-Component	4.33		14.5	
Alignment Pinhole (μm)	25		25	
Seeding				
Generator	Jem Hot2000			
Fluid	Jem Long-Lasting			
Mean Particle Diameter (μm)	1.3			
Position in Tunnel	Between 3rd & 4thCorners			
Measurement Planes				
Position Downstream (%D)	54		×	×
of Wheel Axis	60		60	×
	69		75	75
	88		100	100
No. of Points	414		613	
Max. Samples / Point	2500		5000	
Max. Time / Point (s)	15		20	

C Computational Summary

Case — Phase One			
Fluent Release:	6.0.12		
Version:	3D, Segregated, Steady		
Mesh Type:	Viscous-Hybrid		
No. of Hex. Cells:	5.4×10^5		
No. of Tet. Cells	Domain $= 6.6 \times 10^5$	Sting $= 2.4 \times 10^4$	
Solver Controls		**Options**	
Turbulence Model:	k-ω	Standard	
Material:	Air	Default	
Near-Wall Treatment:	Non-Equilibrium Wall Functions		
Discretisation:		**Order**	**Under-Relaxation**
	Pressure	PRESTO!	0.2
	Momentum	QUICK	0.6
	Pressure-Velocity Coupling	SIMPLE	
	Turbulence	QUICK	0.7
Boundary Conditions	**Type**	**Options**	
Inlet:	**Velocity Inlet**		
	Velocity (ms^{-1})	20	
	Direction Vector	(1,0,0)	
	Turbulence Intensity (%)	0.2	
	Hydraulic Diameter (m)	0.147	
Outlet:	**Pressure Outlet**	As Velocity Inlet	
Ground:	**Wall**	As Velocity Inlet	
Wheel:	**Walls & Fluids**	Origin	(0,0,0)
		Axis	(0,1,0)
		ω$(\mathrm{rad\ s}^{-1})$	152.1

Case — Phase Two			
Fluent Release:	6.0.12		
Version:	3D, Segregated, Steady		
Mesh Type:	Viscous-Hybrid		
No. of Hex. Cells:	4.5×10^5		
No. of Tet. Cells	Domain $= 1.2 \times 10^6$	Sting $= 4.8 \times 10^4$	
Solver Controls		**Options**	
Turbulence Model:	k-ω	Standard	
Material:	Air	Default	
Near-Wall Treatment:	Non-Equilibrium Wall Functions		
Discretisation:		**Order**	**Under-Relaxation**
	Pressure	PRESTO!	0.2
	Momentum	QUICK	0.6
	Pressure-Velocity Coupling	SIMPLE	
	Turbulence	QUICK	0.7
Boundary Conditions	**Type**	**Options**	
Inlet:	**Velocity Inlet**		
	Velocity (ms^{-1})	30	
	Direction Vector	(1,0,0)	
	Turbulence Intensity (%)	0.2	
	Hydraulic Diameter (m)	0.147	
Outlet:	**Pressure Outlet**	As Velocity Inlet	
Ground:	**Wall**	As Velocity Inlet	
Wheel:	**Walls & Fluids**	Origin	(0,0,1)
		Axis	(0,1,0)
		ω$(\mathrm{rad\ s}^{-1})$	190.7

D Transformation of Non-Orthogonal LDA Measurements

This appendix outlines the process of transforming non-orthogonal LDA measurements into the wind tunnel frame-of-reference. In both the Champ Car and Formula One tests the component of velocity aligned with the x-axis, U, was measured directly and therefore required no transformation. This appendix therefore deals with the transformation of the in-plane measurements to V and W components aligned with the major axes, Y and Z respectively.

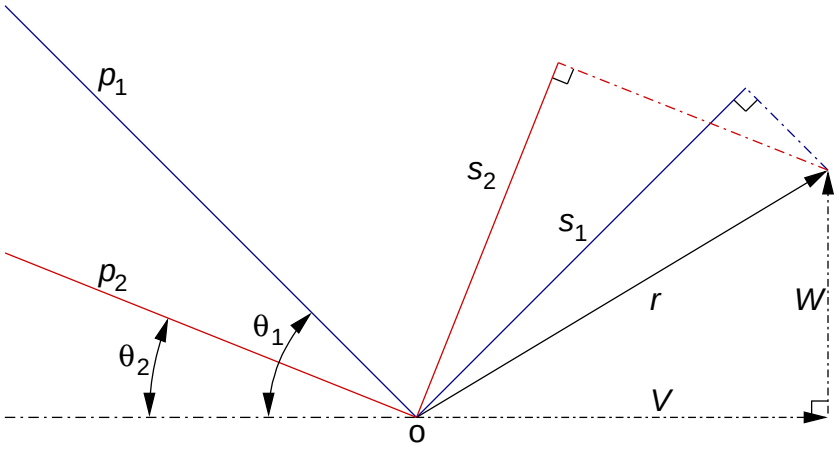

Figure D.1: Schematic of LDA Measurement

From Figure D.1, consider a probe focussed at the origin, *o*, whose beam path is represented by a line, *p*. As the probe is only senitive to flow perpendicular to itself, a seeding particle with velocity, *r*, would generate a signal, *s*, at that probe as it passed through the measurement volume at, *o*. The signal *s*, is related to the particle velocity components in the tunnel frame-of-reference, V and W by the following:

$$s = V\sin\theta + W\cos\theta \tag{D.1}$$

where θ is the angle of the probe to the horizontal plane of the wind tunnel. From Equation D.1 it can be seen that with a single probe the system is under-determined and that two probes, focussed at the same point but at different angles are required to resolve V and W. For the two probes in Figure D.1 the signals generated by the common vector *r* are:

$$\begin{bmatrix} s_1 \\ s_2 \end{bmatrix} = \begin{bmatrix} \sin\theta_1 & \cos\theta_1 \\ \sin\theta_2 & \cos\theta_2 \end{bmatrix} \begin{bmatrix} V \\ W \end{bmatrix} \tag{D.2}$$

which can be re-arranged to give:

$$\begin{bmatrix} V \\ W \end{bmatrix} = \frac{1}{\sin\theta_1\cos\theta_2 - \cos\theta_1\sin\theta_2} \begin{bmatrix} -\cos\theta_2 & -\cos\theta_1 \\ -\sin\theta_2 & \sin\theta_1 \end{bmatrix} \begin{bmatrix} s_1 \\ s_2 \end{bmatrix} \tag{D.3}$$

Therefore, from a set-up such as that shown schematically in Figure D.1, the components V and W can be found using the following transforms:

$$V = \frac{s_1\cos\theta_2 - s_2\cos\theta_1}{\sin(\theta_1 - \theta_2)} \tag{D.4}$$

$$W = \frac{s_2\sin\theta_1 - s_1\sin\theta_2}{\sin(\theta_1 - \theta_2)} \tag{D.5}$$

E Experimental Error Analysis

The systematic and random errors of the presented experimental data are summarised in this appendix.

E.1 Test Configuration

Table E.1: Summary of Errors Associated with Test Configuration

Measurement	Equipment	Systematic Error	Resultant Error
Angular			
Wheel Camber	Digital Protractor	$\pm 0.01^\circ$	$\pm 0.01^\circ$
Traverse Level	Digital Protractor	$\pm 0.01^\circ$	$\pm 0.01^\circ$
Traverse Parallel	Steel Rule	± 0.1 mm	$\pm 0.04^\circ$
Probe Inclination	Digital Protractor	$\pm 0.01^\circ$	$\pm 0.01^\circ$
Wheel Yaw	Steel Rule	± 0.1 mm	$\pm 0.04^\circ$
Velocity			
OJWT – Air	Nozzle Static Pressure	n/a	± 0.2 ms^{-1}
OJWT – Road	Optical Tachometer	± 0.1 revs^{-1}	± 0.01 ms^{-1}
Houghton – Air	Nozzle Static Pressure	n/a	± 0.06 ms^{-1}
Houghton – Road	Tachometer	± 0.1 revs^{-1}	± 0.02 ms^{-1}
F1 Wheel	Optical Tachometer	± 0.1 revs^{-1}	$+0.02$ ms^{-1}
			-0.12 ms^{-1}
Champ Car Wheel	Optical Tachometer	± 0.1 revs^{-1}	$+0.01$ ms^{-1}
			-0.09 ms^{-1}
Positional			
Wheel Location	Steel Rule	± 0.1 mm	± 0.5 mm
Laser Beam Alignment	25μm Pinhole		$\pm 12.5\mu$m
Measurement Location	Steel Rule	± 0.1 mm	see subsection

Measurement Location Uncertainty

The size of the LDA measurement volume introduced a systematic error into the measurement location. Velocity could be recorded from anywhere within that volume and therefore the maximum location error was half of the volume's major dimensions. The resultant errors have been transformed into the tunnel frame-of-reference to account for the orientation of the probes and are summarised for both phases in Table E.2.

Table E.2: Summary of Measurement Location Uncertainty

	Phase One			Phase Two		
Axis	X	Y	Z	X	Y	Z
Error (mm)	± 0.1	± 0.1	± 3.1	± 4.1	± 5.5	± 1.5

The uncertainty in the measurement location was taken into consideration during the design of the measurement grids. As such, each point was unique to the tolerances specified in Table E.2.

E.2 Laser Doppler Anemometer

E.2.1 Seeding Response

Laser measurement techniques rely on the scattering of laser light by particles seeded in the flow. The measured velocity is consequently that of the seeding and not the fluid. Selection of appropriate seeding therefore becomes a compromise between the greater amount of light scattered by a large particle and its reduced ability to track the flow accurately. The method of seeding must also be chosen so as to provide seeding particles of approximately constant diameter because the presence of a large spread of particle sizes will introduce avoidable noise into the signal. A further factor in choosing the seeding material and method, not related to errors, is the accumulation and deposition of the particles in the wind tunnel during testing. Significant testing time can be saved by choosing a fluid seeding material with appropriate volatility so that it evaporates after use leaving little residue.

The seeding used throughout this work was water-based with 15 % ethylene glycol added as an evaporation inhibitor. The particles were generated by ultrasonic atomisation which, in combination with a momentum separator, produced a large volume of uniform-diameter $(1.3\,\mu\text{m})$, ambient-temperature seeding.

The error introduced by the inability of the seeding to follow the flow was assessed using the following method, as described by Dring [48]. In this method the response of a particle to an acceleration of the surrounding fluid is related to the Stokes number, S_t, of the particle. The Stokes number is given by the following relationship:

$$S_t = \frac{\rho_p D_p^2}{18 \mu T_c} \tag{E.1}$$

where ρ_p and D_p represent the particle fluid density and diameter respectively, μ is the absolute viscosity of the surrounding fluid and T_c is referred to as the characteristic time for the acceleration. In this case a characteristic time of 8.6×10^{-3} s was used to represent the time taken for a particle to cross the shear-layer in the down-wash region. Taking air viscosity

as 1.75×10^{-5} kg m^{-1}s^{-1}, the density of the seeding fluid as 1019 kg m^{-3} and substituting 1.3×10^{-6} m for D_p, the Stokes number was estimated as:

$$S_t = \frac{1019(1.3 \times 10^{-6})^2}{18(1.75 \times 10^{-5})(8.6 \times 10^{-3})} = 6.4 \times 10^{-4} \tag{E.2}$$

Dring [48] stated that for small Stokes numbers $(S_t < 0.01)$ the maximum speed error is equal to the Stokes number. Therefore, in this work the error due to the response of the seeding was negligible.

E.2.2 Velocity Bias

As mentioned in the discussion of the seeding response, the LDA signal is generated by the seeding carried by the flow. This random sampling means that the the flow and the samples taken are linked and are not statistically independent. At a given point in a uniformly-seeded flow a velocity fluctuation above the mean value would carry more particles through the measurement volume generating more samples than a similar fluctuation below the mean. In this way the mean velocity calculated from the raw samples will be biased towards the higher velocities. The velocity bias can be completely removed by weighting the samples by a factor inversely proportional to the velocity of the sample during calculation of the mean value. Buchave, George and Lumley [49] recommended the use of the particle transit time[1], t, as the weighting factor. The following calculation was used to remove the velocity bias from the mean measured signals, S:

$$S = \frac{\Sigma_x^N s_x t_x}{\Sigma_x^N t_x} \tag{E.3}$$

where s represents the velocity component measured by the anemometer and the subscript x refers to the index of the current sample, from the population N.

E.2.3 Sampling Error

The rate at which samples of a process are acquired has an impact on the uncertainty of the subsequently-calculated statistics such as the population mean and variance. Correct estimation of such statistics requires statistically-independent samples. If two samples are less than one integral time scale, τ_i, apart they are considered to be statistically dependent or correlated. To ensure statistically-independent samples the sampling interval should be at least twice the integral time scale, τ_i, of the process. As LDA samples are acquired as and when a particle crosses the measurement volume, collection of statistically-independent samples is difficult. It

[1] **Transit Time** the time taken for the particle to cross the measurement volume as recorded by the LDA signal processor. Also referred to as residence time.

was possible to operate the LDA system in "dead-time" mode, where the minimum time between samples could be fixed, but this would require a priori knowledge of the integral time scale of the flow.

The experimental method of Chapter 3 described that in this work the maximum number of samples and the maximum time spent per location were prescribed. The probe moved to the next location when one of the targets was reached. The sampling rate varied with location and therefore so did the associated uncertainty.

This uncertainty was estimated using the method of Benedict and Gould [50] as reported by Dantec Dynamics [51]. In this method, it was proposed that the 95 % confidence limits for a mean value $\overline{U}$ would equal:

$$1.96\sqrt{\frac{\overline{u^2}}{N}} \tag{E.4}$$

This applies equally to any population distribution but assumes that $N > 50$ and that the samples u, are statistically independent. The first criterion was easily satisfied, however the second was not and was addressed in the following way. The potential number of statistically-independent samples, N_{eff}, was calculated from the sampling time, T_m, and the integral time scale:

$$N_{eff} = \frac{T_m}{2\tau_i} \tag{E.5}$$

If $N > N_{eff}$, then N_{eff} was substituted into Equation E.4 otherwise it remained unchanged. However, calculation of N_{eff} required a posteriori estimation of the integral time scale.

The estimation of τ_i was carried out following the method presented by Nobach [52] and the interested reader is referred to his work for a detailed treatise on this subject. As previously mentioned, τ_i is related to the correlation of two samples of the same population, and as such can be found from the autocorrelation function, ACF, of the population. In a dataset where all samples were equidistant the ACF could be estimated from the inverse Fourier transform of the power spectral density of the data (estimated using a Fourier transform). In the case of the randomly-sampled LDA data, Fourier analysis is not possible unless the data are re-sampled to be equidistant, a process which may introduce further error due to aliasing.

In the method described by Nobach [52] the ACF is estimated using slot correlation (see [52]) which does not involve re-sampling the signal and therefore avoids aliasing issues. The method also incorporated transit-time weighting to remove the velocity bias during estimation. Software was written by the author which estimated τ_i at each location in a measurement plane, allowing calculation of N_{eff} and subsequent calculation of the confidence limits for the mean values.

As the U-component of velocity was measured directly it was a prime target for error analysis. Figure E.1 represents the 95 % confidence limits at each point as a percentage of the unbiased $\overline{U}$ at that point. Figure E.1(a) represents the data collected during Phase One and includes data from two of the four measurement planes. Figure E.1(b) represents the data from Phase Two

and includes one plane of data from each support sting. In both cases the figure shows that to a 95 % confidence level one third of the points have an error of $< 1\%$.

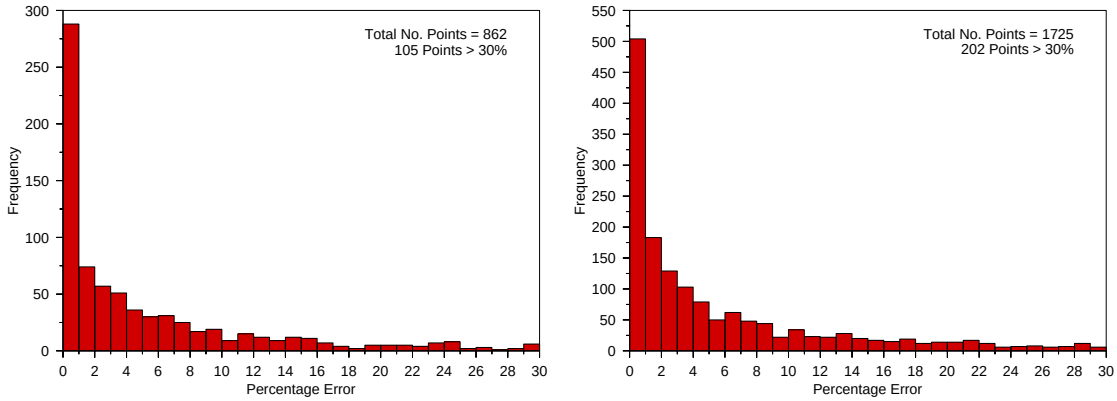

(a) Champ Car Data

(b) Formula One Data

Figure E.1: Point-wise Percentage Mean U Velocity Error – 95 % Confidence Limit

F Additional Plots

This appendix contains a complete set of velocity profiles as used in the verification and validation of the computational models from both phases.

- Figure F.1 – Phase One Data, Horizontal Profiles
- Figure F.2 – Phase One Data, Vertical Profiles
- Figure F.3 – Phase Two Data, Horizontal Profiles
- Figure F.4 – Phase Two Data, Vertical Profiles

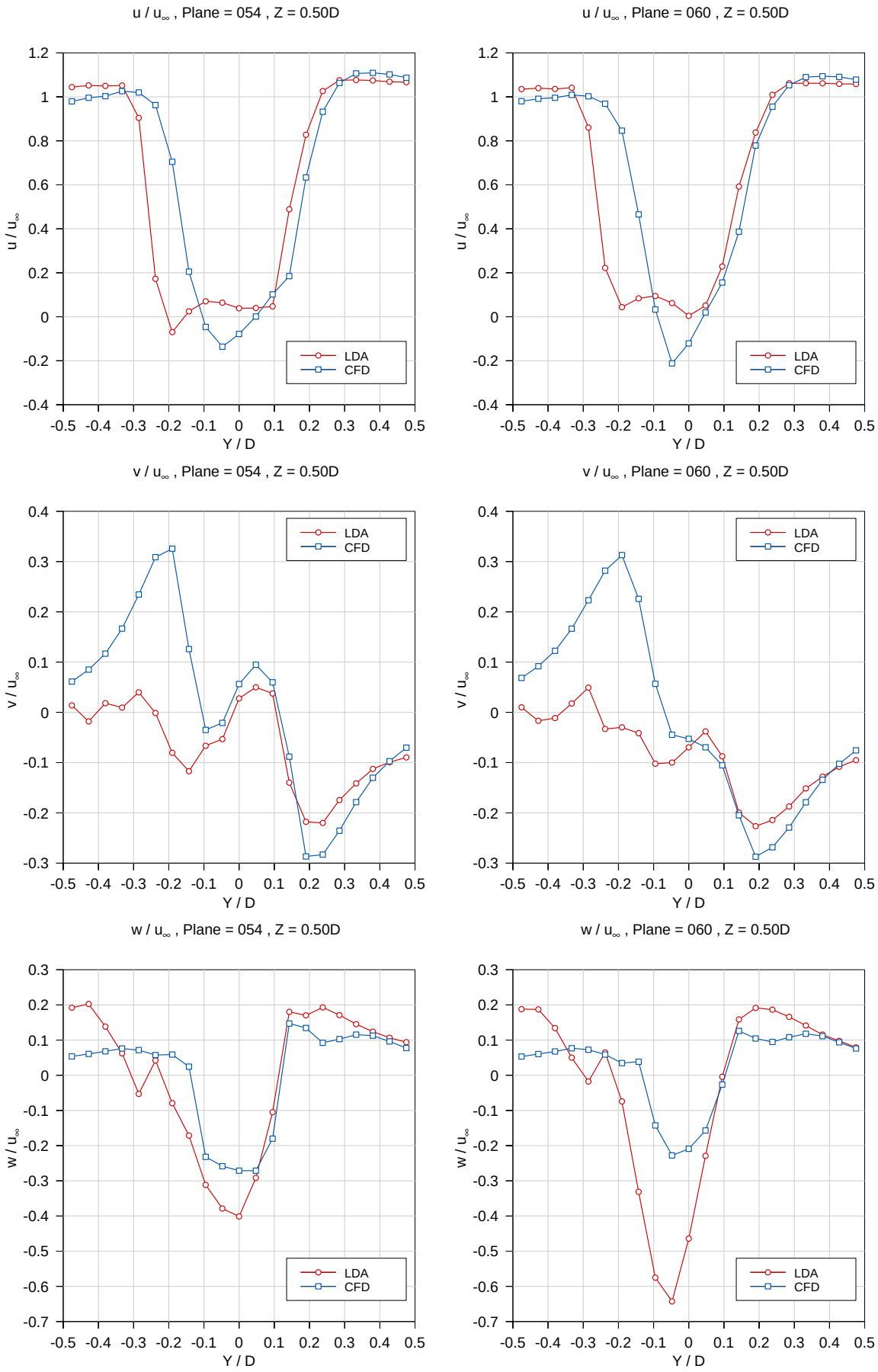

Figure F.1: Validation - Phase One Data - Horizontal Centreline ($Z/D = 0.5$)

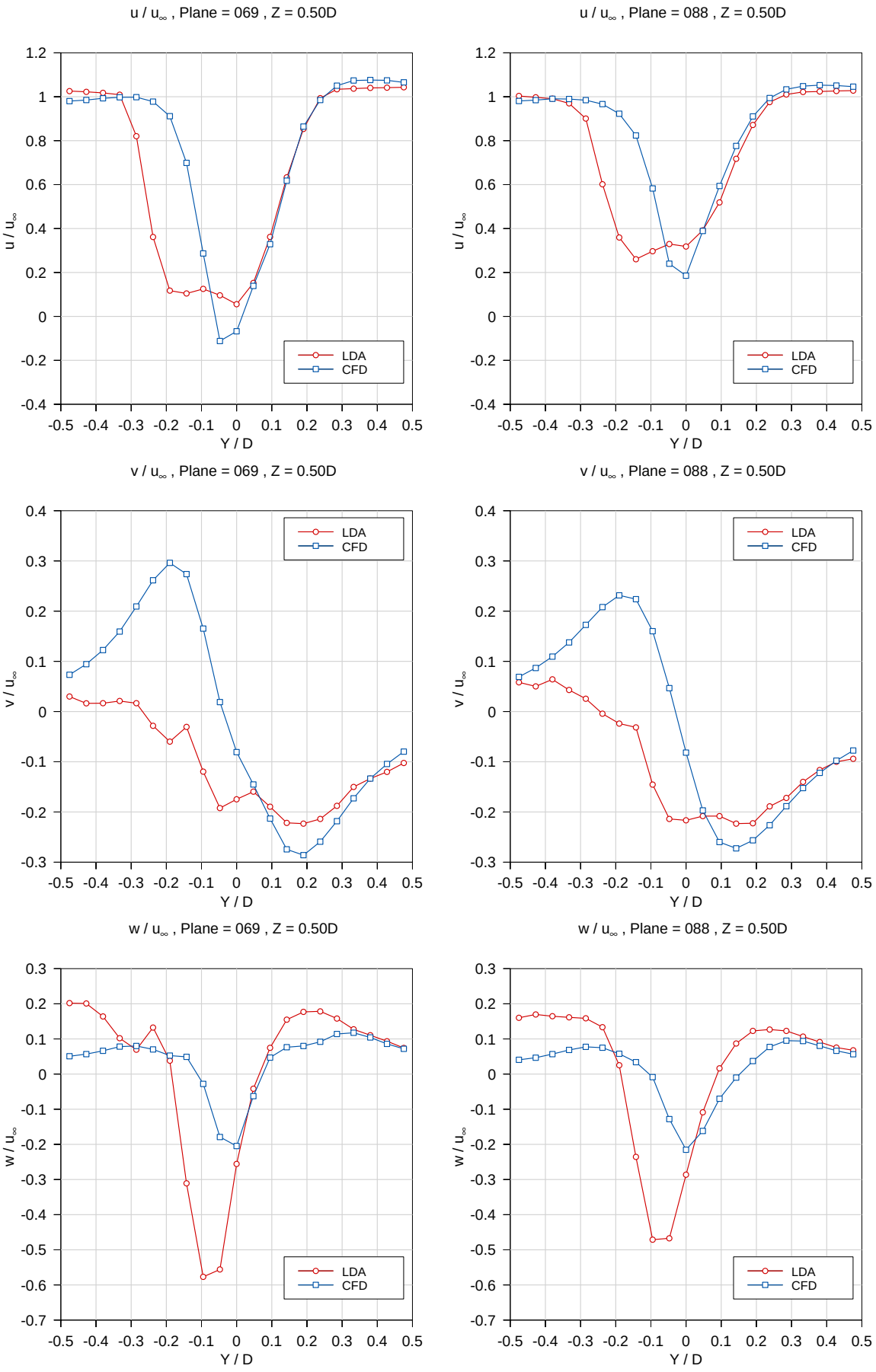

Figure F.1: (cont.) Validation - Phase One Data - Horizontal Centreline ($Z/D = 0.5$)

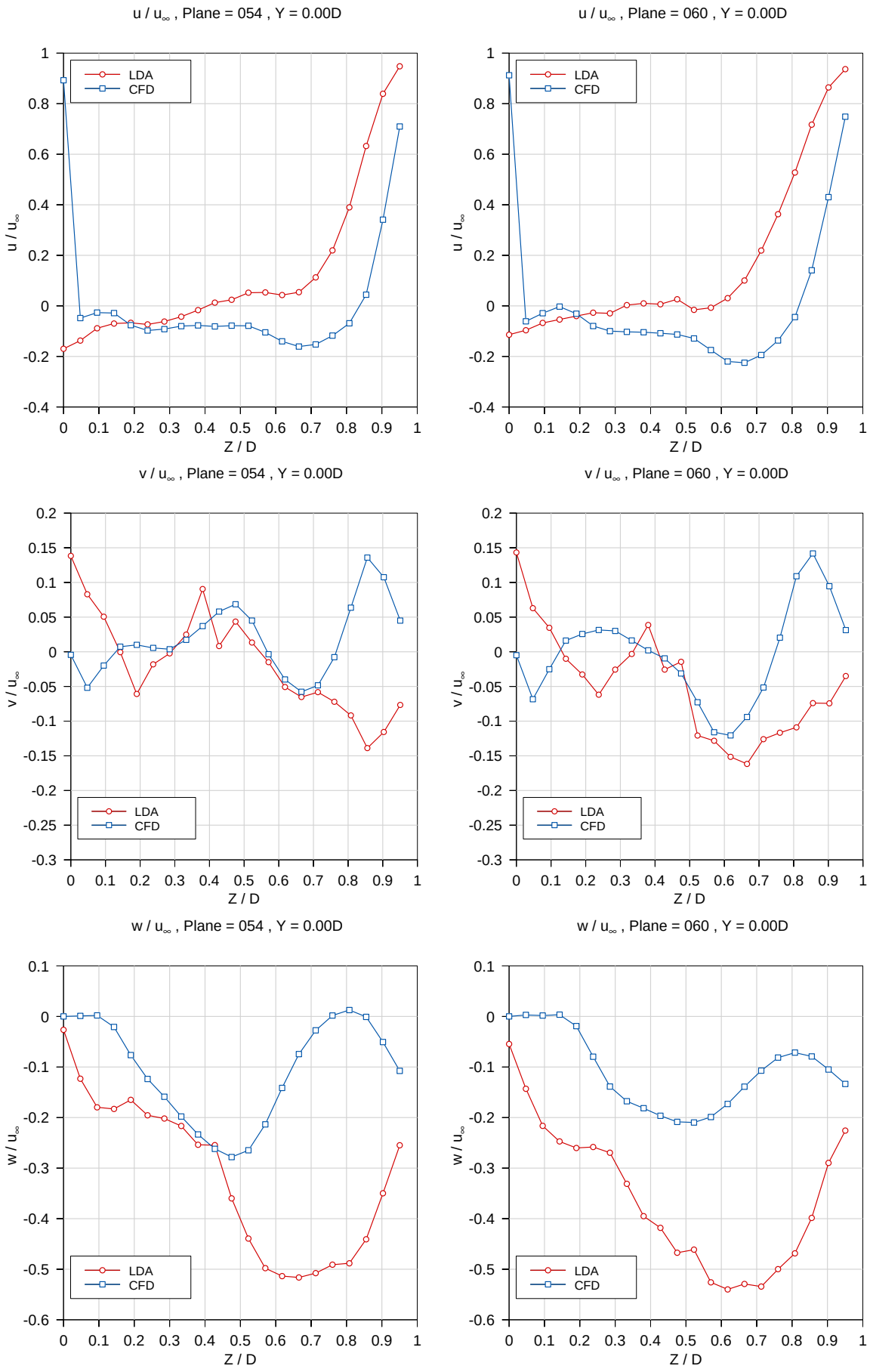

Figure F.2: Validation - Phase One Data - Vertical Centreline ($Y/D = 0.0$)

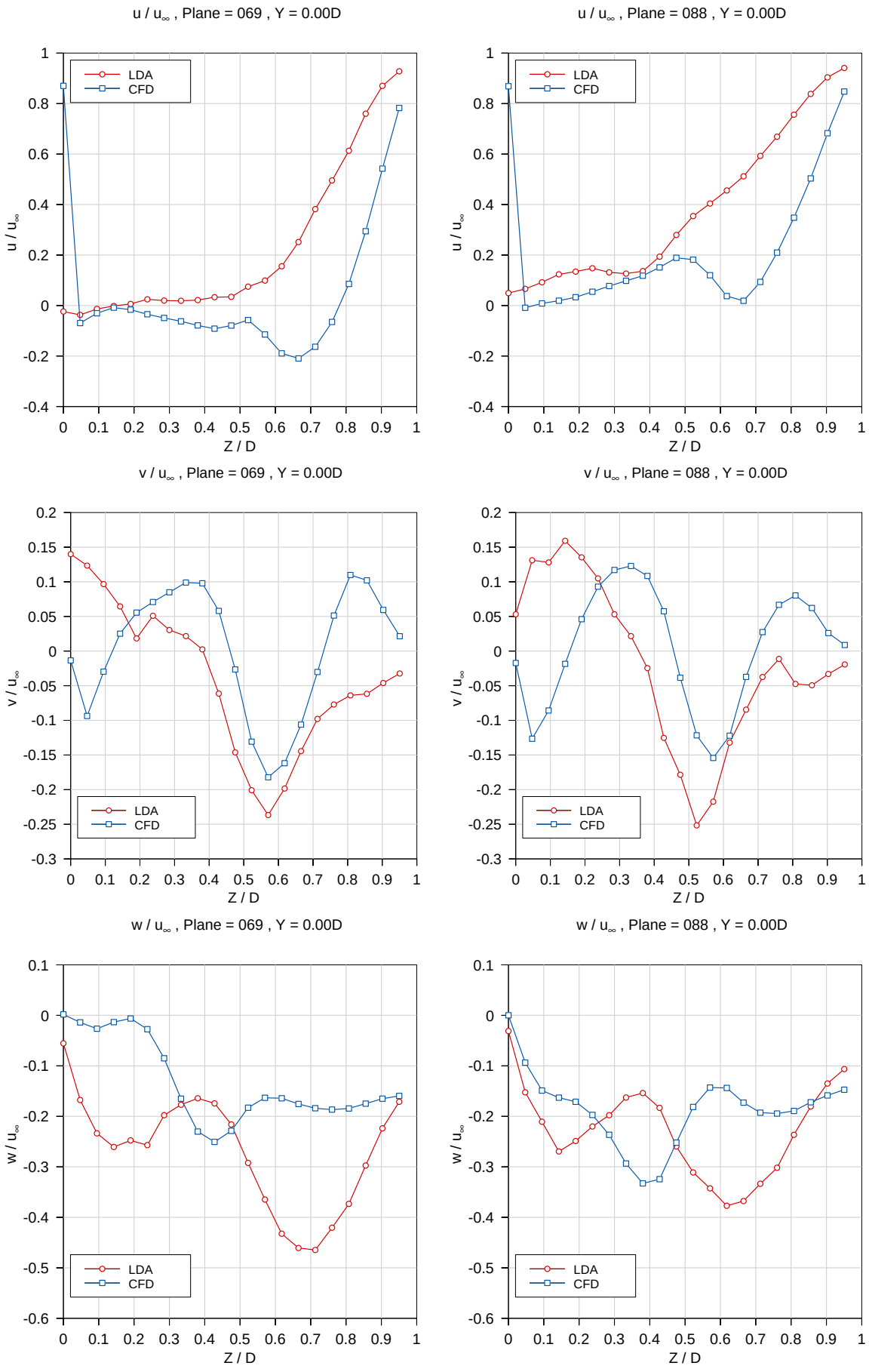

Figure F.2: (cont.) Validation - Phase One Data - Vertical Centreline ($Y/D = 0.0$)

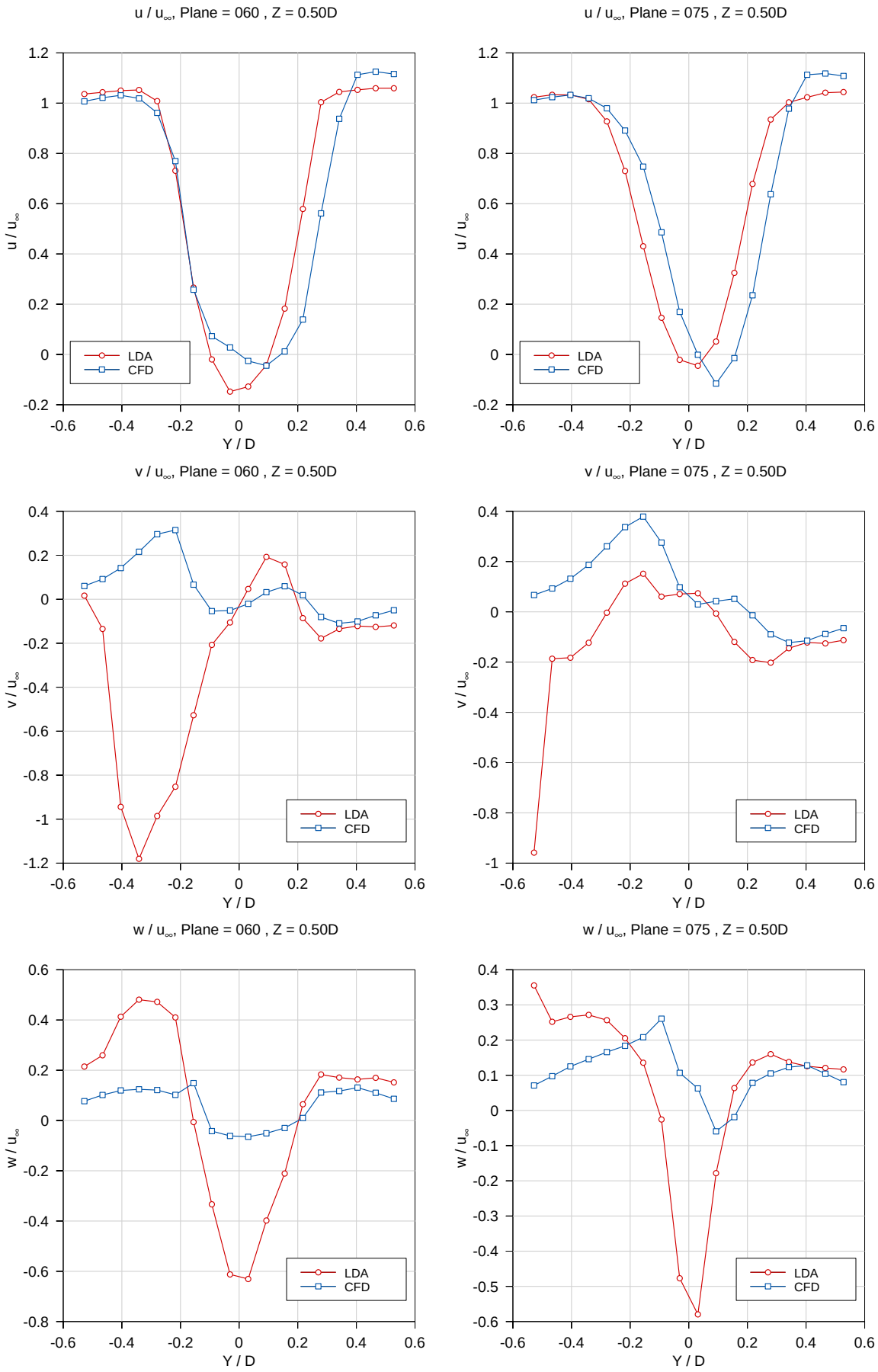

Figure F.3: Validation - Phase Two Data - Horizontal Centreline ($Z/D = 0.5$)

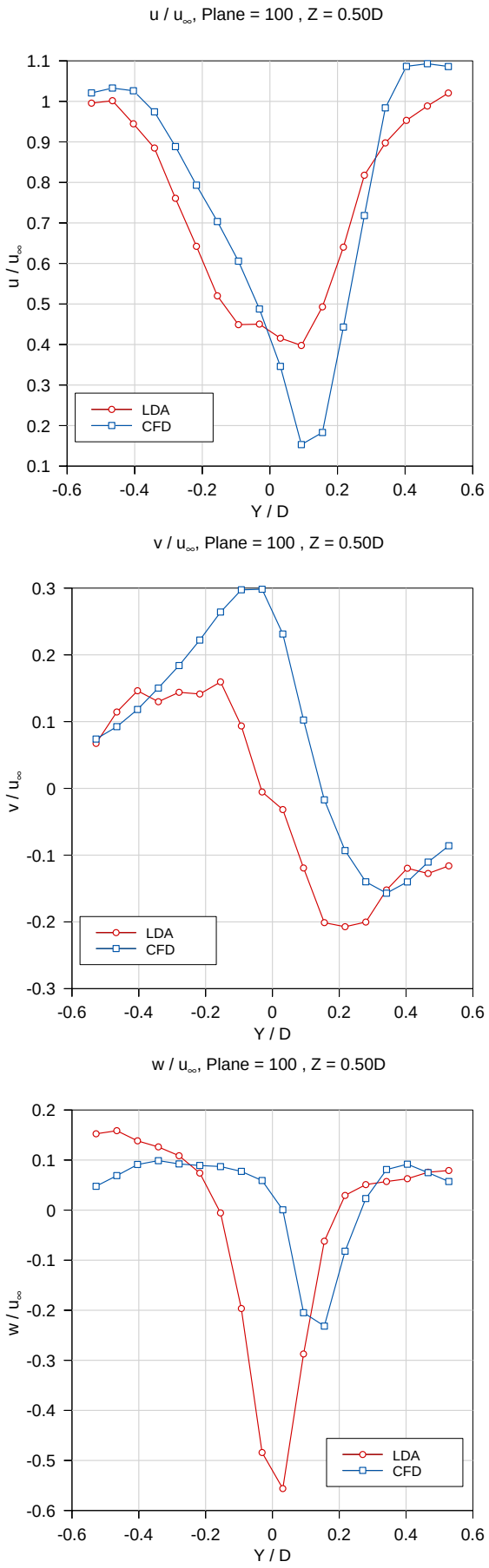

Figure F.3: (cont.) Validation - Phase Two Data - Horizontal Centreline ($Z/D = 0.5$)

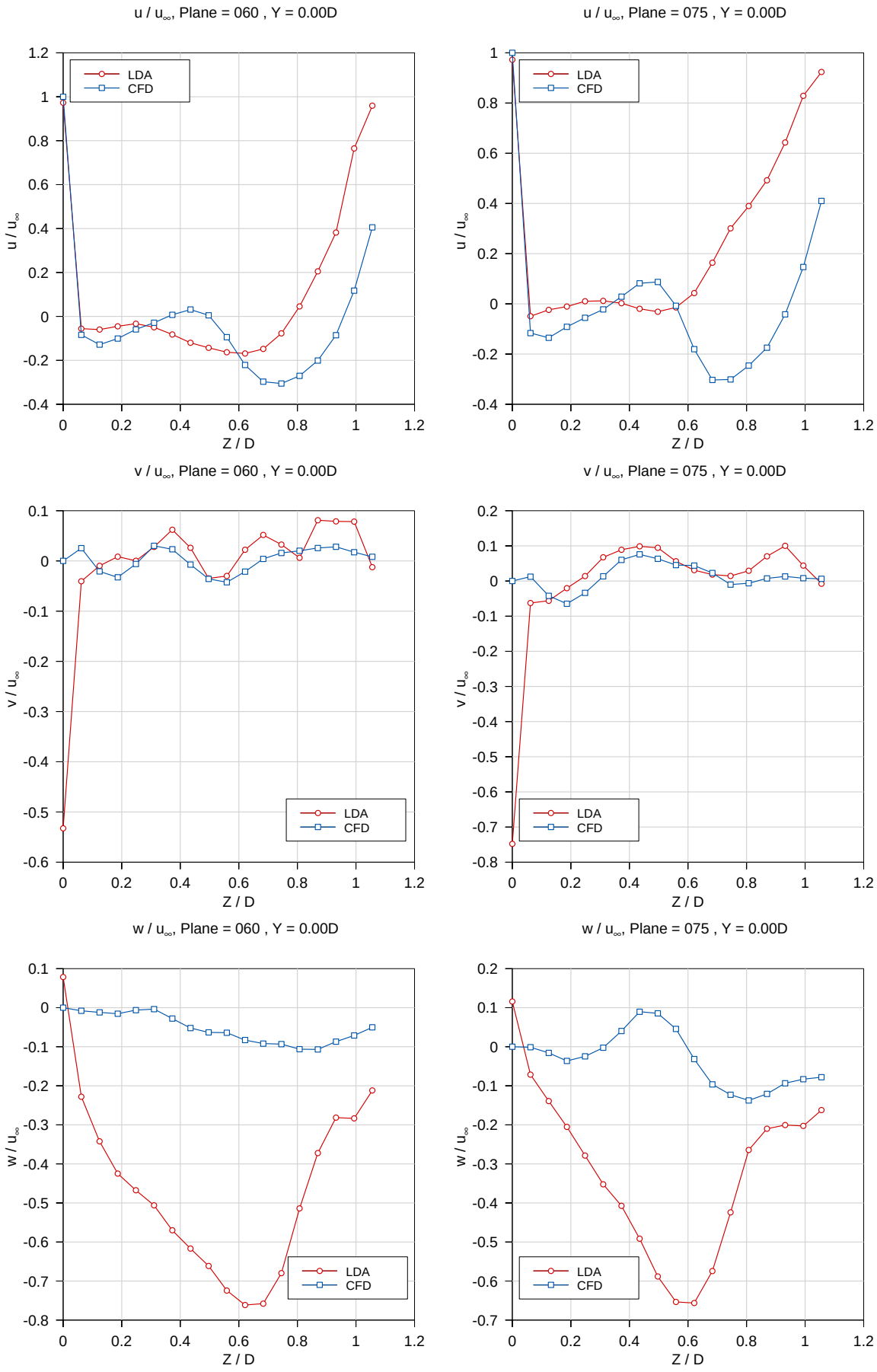

Figure F.4: Validation - Phase Two Data - Vertical Centreline ($Y/D = 0.0$)

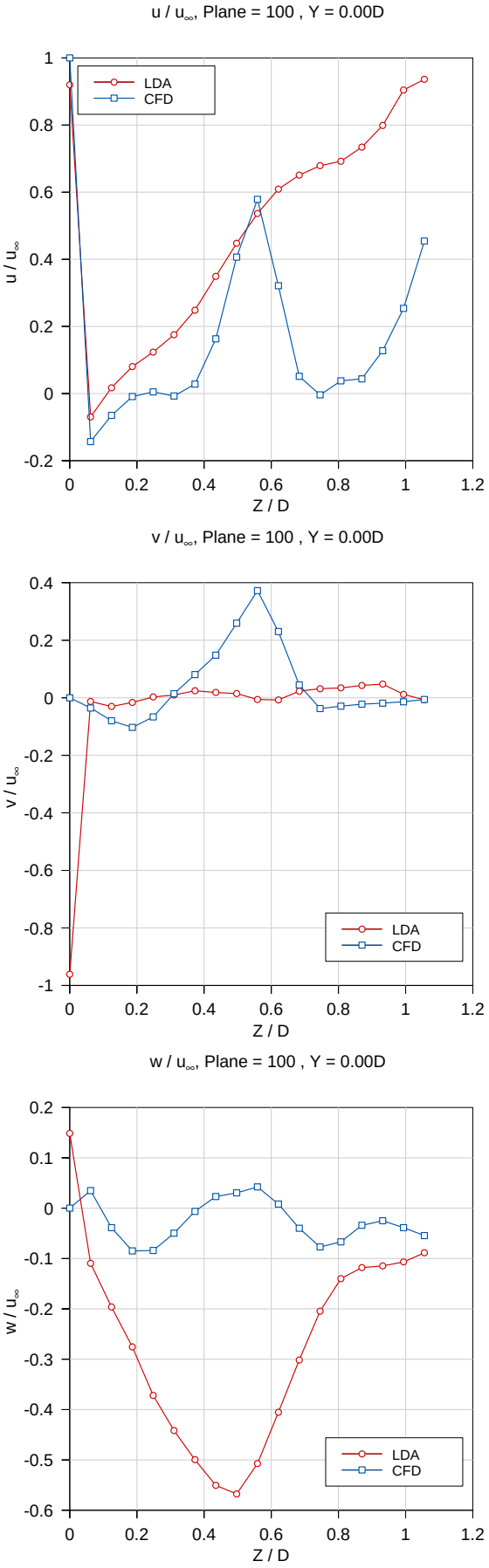

Figure F.4: (cont.) Validation - Phase Two Data - Vertical Centreline ($Y/D = 0.0$)

G Published Work

The first of the two papers listed below was written and presented in summary of Phase One of this investigation. The second paper reports an investigation carried out in parallel with Phase One which began to investigate the effect of using conical non-deformable wheels to represent camber angle. Both papers are included in this appendix for reference.

- **Knowles, R. D.**, Saddington, A. J., and Knowles, K., Simulation and Experiments on an Isolated Road Wheel Rotating in Ground Contact, In *Proc. of 4th MIRA International Vehicle Aerodynamics Conference*, Warwick, UK, 16-17 October 2002
- **Knowles, R. D.**, Saddington, A. J., and Knowles, K., On the Near Wake of Rotating, 40%-Scale Champ Car Wheels, *SAE 2002 Transactions - Journal of Passenger Cars: Mechanical Systems*, 6:2245–2253, 2003
  - Also presented at the SAE Motorsports Engineering Conference and Exhibition, Indianapolis, IN, 2-5 December 2002.

Simulation and Experiments on an Isolated Racecar Wheel Rotating in Ground Contact

Robin Knowles, Alistair Saddington and Kevin Knowles
Aeromechanical Systems Group, Cranfield University, RMCS Shrivenham

Abstract – This paper presents the results of experimental and computational (CFD) investigations into the flowfield surrounding an isolated wheel rotating in ground contact. The CFD model was validated using three-dimensional velocity data and was shown to correctly predict the position, size, rotational sense and convection of the vortical structures in the near wake of the wheel. The predicted drag coefficient was within 6% of the experiment. The effect of the support sting was investigated using CFD and was found to suppress the formation of one wake vortex, increase the flow through the wheel and reduce wheel lift by 16%.

Introduction – Current racecar aerodynamic development relies heavily on the testing of scale models in wind tunnels to gather the majority of data. As the potential performance increases that can be realised through aerodynamic optimisation are considerable so is the investment level in this area. Wind tunnels have evolved from those borrowed from the aerospace industry to purpose-built facilities with advanced ground simulation. Correspondingly, wind tunnel models have developed from generic representations of the racecar in question to faithfully-detailed scale models including such things as exhaust blowing, vented brake discs and radiator cores with accurate pressure drops. Suspension and wing incidences are computer controlled and can be varied during a test run without the need to stop the tunnel. The models contain a multitude of sensors and yield an enormous amount of data for the aerodynamicist to evaluate. Advanced flow visualisation and measurement techniques such as Laser Doppler Anemometry (LDA) and Particle Image Velocimetry (PIV), and traditional techniques such as oilflow yield further information on the aerodynamic performance of the racecar.

In recent years another tool, Computational Fluid Dynamics (CFD), has filtered down from the aerospace industry and become available to the automotive aerodynamicist.

The technology associated with CFD has evolved quickly over recent years in much the same way as both wind tunnels and their models. Simulations that were computed for a generic body shape with highly simplified boundary conditions using inviscid vortex panel methods can now be replaced by computational representations of the actual racecar with realistic boundary conditions solved using robust, Reynolds Averaged Navier-Stokes (RANS) codes.

One of the great strengths of CFD is that once a model is verified and validated using data from wind tunnel tests, parametric design studies can be conducted relatively quickly and easily. The data from such studies can be used to predict the performance of new components or configurations and determine which are worthy of model-scale manufacture for wind tunnel testing. Providing the computational facilities and expertise are available, CFD can provide unparalleled insight into aerodynamic phenomena and save money and time in the manufacture and testing of wind tunnel models.

As previously mentioned, the wind tunnels used in racecar aerodynamic development are generally equipped with ground simulation. This often takes the form of a continuous belt rolling road, synchronised with the tunnel freestream, and coupled with a boundary layer control device such as suction or tangential blowing. Ground simulation and the associated wheel rotation is known to be essential for accurate automotive testing [1], and is of considerable importance in the development of open-wheel racecars such as Champ Cars or Formula One. With this type of vehicle, ground effects and large unfaired wheels dominate their aerodynamic characteristics. As in experimental testing, every care must be taken to ensure that the wheels are modelled correctly in computational simulation. Verification and validation of a computational model requires high quality experimental data. Previous evaluations of the capability of CFD to model wheel flows [2, 3, 4] used the surface pressure and force data published by Fackrell [5, 6] as their main validation criteria.

This paper presents an overview of an experimental investigation into the flowfield surrounding an isolated racecar front wheel rotating in ground contact, supported by a sting. Non-intrusive measurements were made in the near wake of the wheel using Laser Doppler Anemometry (LDA), yielding three-dimensional, time-averaged, pointwise velocity data. Wheel drag force measurements are also presented.

The experiment was subsequently modelled using CFD techniques. The paper verifies and validates the model through direct comparison with the experimental data. The data provide an insight into the wake structure of an isolated wheel rotating in ground contact but this was not explicitly evaluated.

Once validated the model was used to predict qualitatively the performance of the wheel rotating without the support sting. The influence of such supports, commonly used in automotive testing, is often overlooked, as it is experimentally challenging to determine. All computational work was carried out using the Version 6 release of the FLUENT®CFD software suite.

Experimental Set-up – This work attempts to reflect the current state-of-the-art in both experimental and computational techniques. Therefore, it was deemed important to test model components currently employed in racecar development. A 40% scale (263mm diameter), non-deformable Champ Car front wheel assembly was chosen along with its associated support sting. Two factors worthy of note are the non-deformable nature of the wheel and the presence of the support sting.

Wheel Assembly – Excepting the expensive steel and multi-belt systems most wind tunnel rolling roads do not allow testing of a pneumatic tyre deformed by application of a vertical load. The contact force required to deform the tyre results in excessive belt wear, whilst failure of either the tyre or belt can result in tunnel and model damage. The profile of a pneumatic tyre in operation is transient and also non-axisymetric about its rotational axis. It is common practice in model-scale automotive aerodynamic development to use non-deformable tyres. Such a tyre can be generated by 'blending' undeformed and deformed tyre profiles and revolving the result about the rotational axis. Therefore, a non-deformable tyre can only be considered to be an approximation of 'real world' conditions.

The tyre used in this study was manufactured from carbon fibre with a smooth, lacquered surface finish. It was mounted on a machined aluminium hub, an exact replica of the BBS multi-spoke alloy hubs currently in use in Champ Car racing. The assembly also featured a radially-vented brake disc with mounting bell and free-running bearings to allow rotation.

Support Sting – The frictional forces between the wheels and the rolling road belt bring about the need for the wheel support sting. Wheel forces, both aerodynamic and mechanical, are significant and can account for between 35% to 50% of the total drag of an open-wheeled racecar [7]. In aerodynamic development the frictional contact forces are of little interest and must be accounted for in order to determine accurately the aerodynamic performance. One solution is to mount the wheels on individual support stings, as opposed to the model car suspension, de-coupling the wheel forces from those of the car. All forces can then be resolved independently using force balances. The car balance will measure only the aerodynamic forces exerted on the car and the wheel balances can be used to determine the effect of body changes on wheel drag. It is very difficult to resolve accurately the often significant wheel lift forces using balances due to the fluctuating nature of the wheel-to-belt contact.

The experimentally tested sting was of aluminium beam section with a symmetrical aerofoil profile. It supported a 50N load cell, oriented to measure drag force, to which the wheel was attached. The aerofoil profile was extended to the wheel by shrouding the load cell with carbon fibre. The instrumentation cabling was shielded from the freestream air by routing it inside the sting. No vertical force, other than that due to the weight of the components, was applied during testing and no problems were encountered with wheel lift. The experimental set-up is shown in Figure 1.

Tunnel & Road – The wheel was tested in the Shrivenham 1.52m by 1.14m closed-return, open-jet wind tunnel. A continuous-belt rolling road, 1.2m by 1.7m, provided

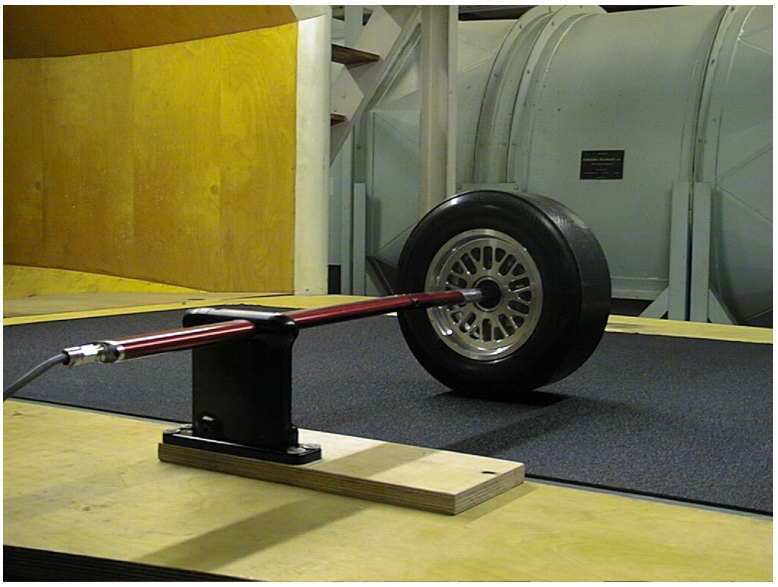

Figure 1: Experimental Set-up

ground simulation and wheel rotation. The rolling road was synchronised with the tunnel freestream velocity and boundary layer control was provided by upstream suction and a knife-edge transition. This system achieved a boundary layer thickness of 5.7mm (99% freestream dynamic pressure), at 410mm downstream of the knife-edge, corresponding to the wheel position during testing.

LDA System – The LDA measurements were made using a two-component and a single-component, 1m focal length, Dantec FibreFlow probes mounted to a three-component traverse. Data management was carried out by three BSA enhanced signal processors, with all equipment centrally controlled by Dantec Burstware software. A JEM Hydrosonic 2000 fog generator, placed inside the tunnel upstream of the turbulence screens, was used to seed the tunnel flow. The generator ran continuously throughout testing and no problems were encountered with seeding density or particle size using this arrangement.

Access to the test section by the traverse was restricted by the tunnel's overhead balance gantry. This required off-axis measurement of the horizontal, transverse velocity component, V. It also became necessary to measure the vertical component, W, off-axis to allow measurements to be made at the road surface. The probe set-up was optimised to minimise off-axis measurement errors, whilst maximising the measurement area. The U-component (with the freestream flow) was directly measured, with V and W components resolved during post-processing, using the measured inclination angles of the probes. The set-up allowed the probes to remain outside the wind tunnel jet throughout testing, thus minimising flow disturbance.

CFD Set-up – The set-up of computational fluid dynamic simulations is dominated by the spatial discretisation or mesh generation phase. The type of mesh chosen is in turn dictated by the geometry of the problem and the time available for this phase. As

seen in Figure 1, the geometry of the problem is reasonably complex, especially in the region of the spokes and (unseen in the picture) the vented brake disc assembly. It was deemed important that the CFD model should remain as faithful to the tested configuration as possible, thus allowing direct comparison between them. The geometry of the tested components was not simplified but at this initial stage the wind tunnel was not explicitly modelled. The manufacturing CAD data of the wheel assembly and sting formed the basis for mesh generation.

A viscous-hybrid approach was taken whereby regions of hexahedral or prismatic cells are used to resolve areas where viscous effects dominate, such as boundary layers. The remainder of the solution domain is resolved using tetrahedral cells. The approach exploits the ability of prismatic and hexahedral cells to resolve better the normal gradients in boundary layers whilst using fewer cells than the tetrahedral equivalent.

The wheel and sting assembly was placed in a rectangular domain with the inlet 5 wheel diameters upstream, outlet 16 wheel diameters downstream, a width of 10 and a height of 5 wheel diameters. The tyre was embedded within a block of hexahedral cells, which was extended into the wake region to discretise the area investigated experimentally. The domain boundaries and all components except the tyre were covered with a triangular surface mesh and the remaining volume filled with tetrahedral cells. The hexahedral and tetrahedral fluid zones were linked using non-conformal grid interfaces. The interior of the sting was also meshed to allow it to be removed from the solution domain by allowing fluid to flow through it, thus eliminating the need to generate an entirely new mesh for that section of the study.

The only significant deviation from the experimental geometry was made at the tyre contact patch. Difficulty was encountered in maintaining high cell quality when modelling the near line-contact between the rolling road and non-deformable tyre. Therefore, the wheel was slightly truncated by raising the ground plane by 0.8mm. This increased the size of the contact patch and greatly improved the cell skewness in this area. The final mesh was of the order of 0.93 million cells. Figure 2 shows the surface mesh on the wheel and sting assembly.

Experimental Procedure – The experimental set-up was tested at 20ms^{-1}, the safe working limit of the rolling road, corresponding to a Reynolds number (based on wheel diameter) of 3.69 x 10^5. LDA measurements were made in four vertical planes oriented perpendicular to the freestream flow. Traverse access confined each plane to being a 250mm square, centered about the longitudinal centreline of the wheel. The planes were located at 10, 25, 50 and 100mm downstream of the rearmost part of the wheel and contained identical grids of 441 equally-spaced data points. All three velocity components were simultaneously sampled over a 15 second period yielding 2500 samples for each component at each point. When processed, these data subsequently provided time-averaged three-dimensional velocity results.

The frictional contact forces were determined by testing the wheel rotating without wind and were used to correct the mean drag force measured under full test conditions. The accuracy of this correction was undetermined, but corrected forces were found to be

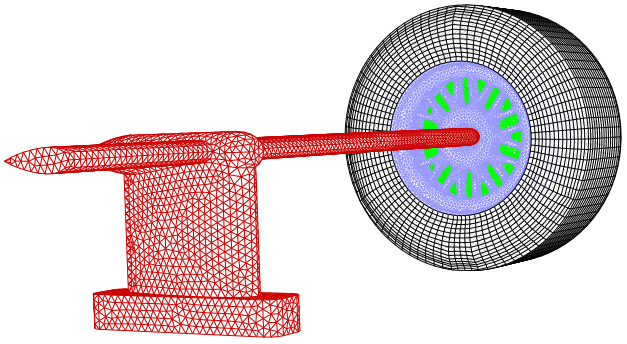

Figure 2: CFD Surface Mesh of Wheel Assembly and Support Sting

repeatable within 0.5%.

Simulation Procedure – The boundary conditions of the CFD simulation were chosen to be representative of those of the experiment. A uniform flow with a velocity of 20ms^{-1} was specified at the inlet and standard atmospheric pressure specified at the outlet. The rolling road and wheel components were modelled as translating and rotating walls respectively, all with a linear velocity of 20ms^{-1}. When simulating the wheel and sting, the sting surface was specified as a wall with the no-slip condition applied. In this configuration the mesh inside the sting was regarded as a solid and not solved. When testing the wheel without the sting, its surface was represented by an interior condition, which did not impede flow. The mesh inside the sting was solved as a fluid, effectively removing the sting from the domain. Symmetry planes, (walls where slip is permitted), represented the remaining domain boundaries.

Several turbulence models were tested in the initial stages of this study, but this paper will only present the results of the standard k-ω model as it was considered by the authors to offer the best results of those tested. These included the RNG k-ϵ, Realisable k-ϵ, Spalart-Allmaras, Shear Stress Transport (SST) k-ω and Reynolds Stress Transport Models. Non-equilibrium wall functions, sensitised to pressure gradients, provided near-wall treatment in all cases. Appropriate first cell heights were used in the mesh generation phase to ensure wall y^+ values suitable for this type of treatment.

Wheel drag and lift coefficients (based on projected frontal area) were monitored throughout simulation along with the mass-flow-rate through the wheel. These monitors were used as convergence criteria, with the simulation deemed to be converged when all three values were steady to at least three significant figures over 100 iterations. Convergence was aided by solving the initial period of simulation using first order differencing schemes before switching the pressure interpolation scheme to the Pressure Staggering Option (PRESTO!) and the remaining terms to second-order accurate schemes. Convergence was achieved within three thousand iterations, requiring approximately 30 CPU hours on a Compaq Alpha DEC-based Beowulf cluster.

At this initial stage, solution-adaptive mesh refinement was not practised, and therefore, grid convergence was undetermined.

The U, V and W velocity components from four planes equivalent to those measured experimentally were exported for verification and validation. The surface pressure coefficients on the tyre circumferential centreline and force coefficients were also used for this purpose.

Results & Analysis – The three-dimensional results of the LDA and CFD investigations are presented as in-plane velocity vectors (Figure 3) and contours of U velocity (Figure 4).

In-plane velocity vectors – The representation of the V and W components of velocity as in-plane vectors highlights the vortical structures present in the wake of the wheel. The biggest difference between the numerical and experimental results is in their magnitudes. Looking beyond that, the vortical structures captured are very similar. All results clearly show the presence of a pair of counter-rotating ground vortices and an upper right vortex.

Merker and Berneburg [8] termed the ground vortices, “jetting” vortices in reference to their origins in the viscous actions at the tyre contact patch. This term will be adopted in this study with the remaining structure simply designated the upper vortex. All references to left and right are with respect to the figures, where the wheel sting was to the right and a car would be to the left.

10mm downstream – CFD has predicted the upper vortex in the correct position and of approximately the correct size. The jetting vortices are higher, less defined and appear smaller than measured experimentally. Correspondingly there is less entrainment from upper left to lower right and the central region has a greater negative W component.

25mm downstream – The LDA upper vortex reduces in height at this station, a trend captured by CFD but to a slightly lesser extent. With regard to the jetting vortices, the left structure is more defined than seen in the experimental data, with the right one more central than expected. Jetting vortex size and position is poorly predicted at this distance downstream.

50mm downstream – The strong prediction of upper vortex size and position continues in this measurement plane. The calculated location and extent of the left jetting vortex is now in much better agreement with the experimental data. The right structure has reduced in size and increased in definition although its location is still poorly predicted.

100mm downstream – The size, shape and position of all three vortex structures are now in strong agreement with the LDA data. However this is somewhat masked by the over prediction of the magnitudes of both V and W components.

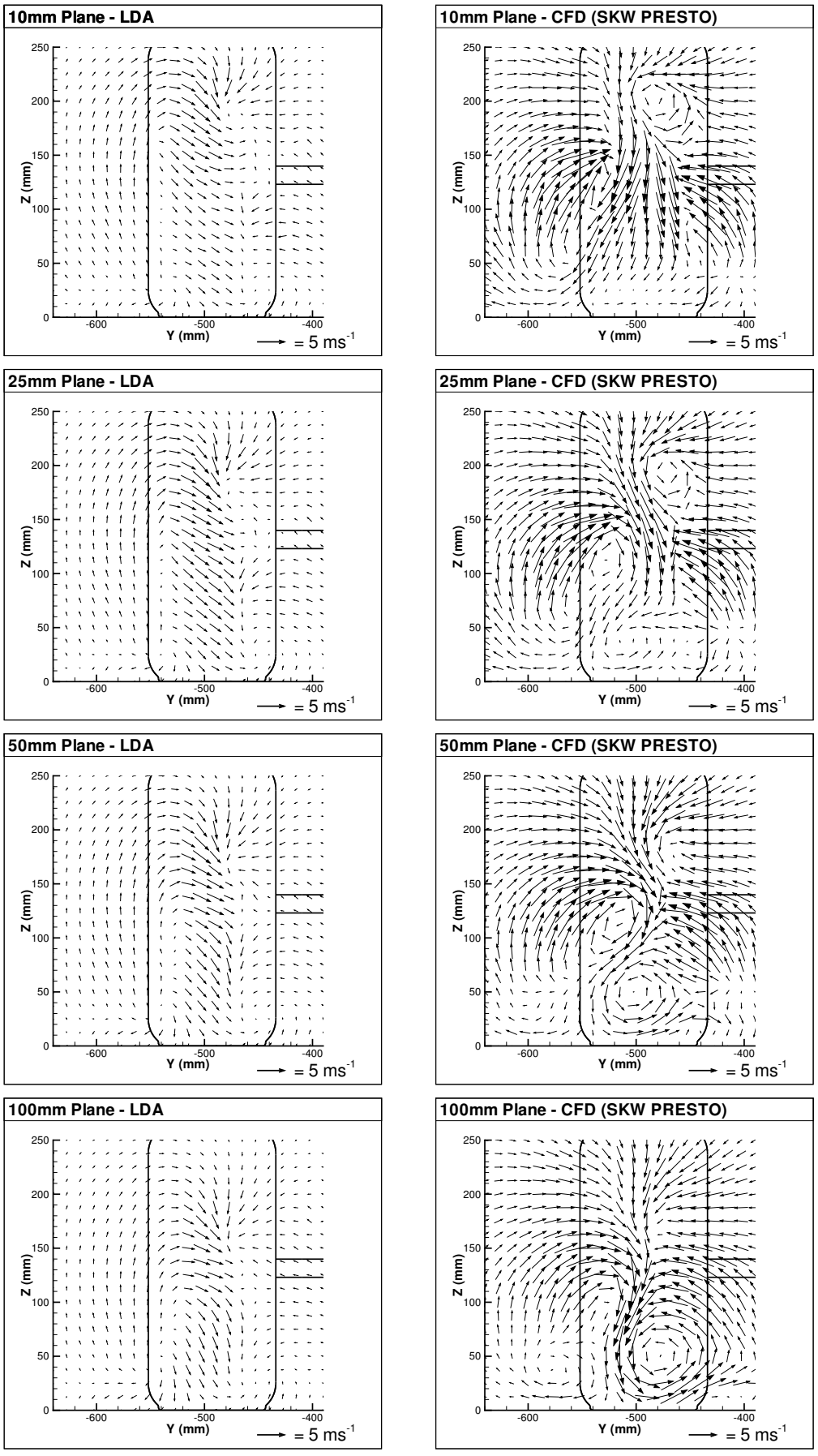

Figure 3: In-Plane Velocity Vectors (LDA - CFD Comparison)

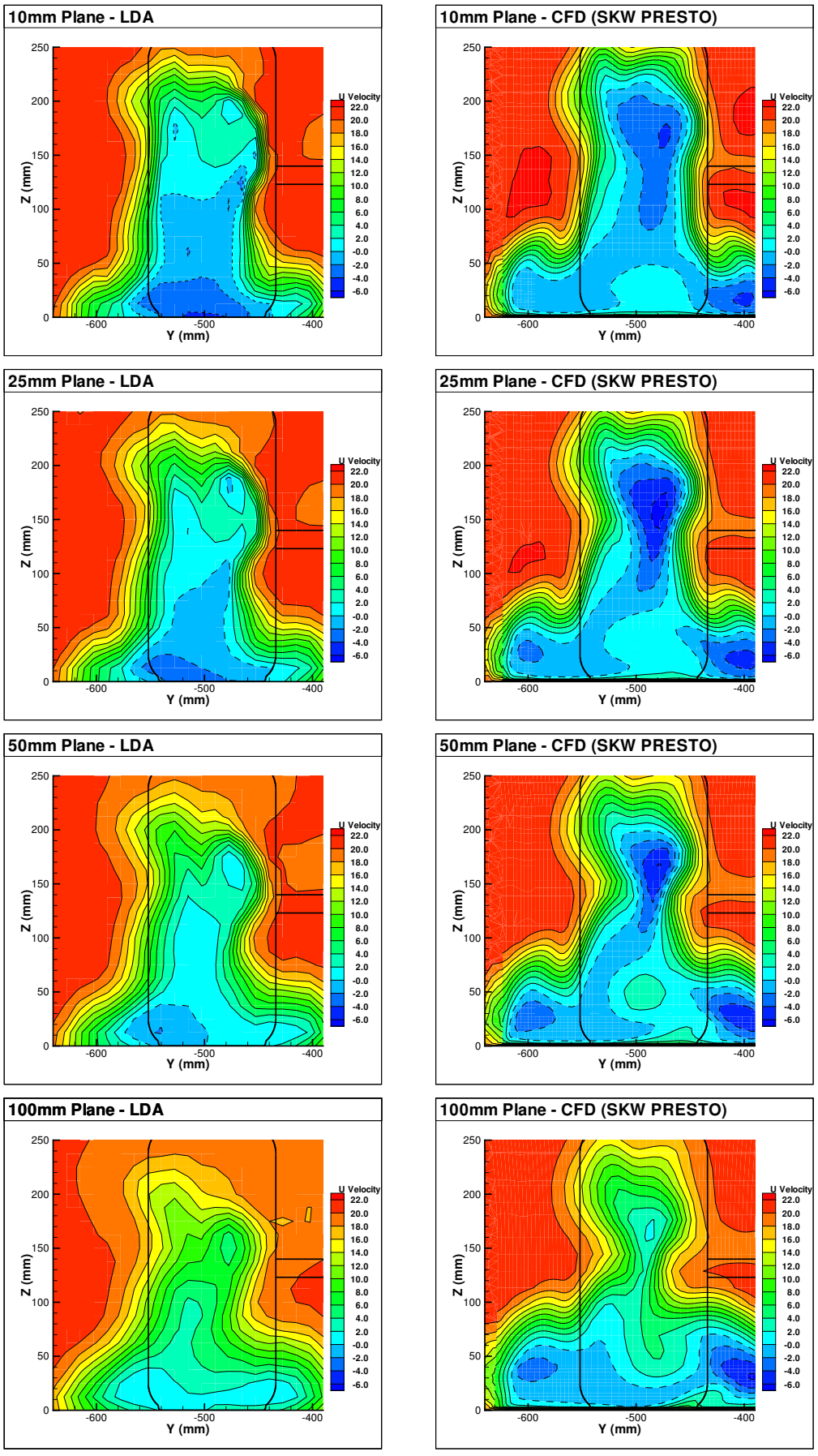

Figure 4: Contours of U Velocity (LDA - CFD Comparison) - Negative values indicated by dashed lines

U velocity contours – In general the LDA and CFD data shown in Figure 4 appear to agree well. The overall shape and extent of the velocity deficit is good, capturing most of the salient features of the experimental results. These include the basic asymmetry of the wake, the presence of the sting and the several regions of reversed flow.

It is in this area that the largest differences occur. One point of note is the over-prediction of reversed flow in the upper, central region of the wheel profile. The peak in this area appears to coincide with the centre of the upper vortex and could possibly be linked with the increased vorticity of the predicted structure over that measured. Further, the experimental results exhibit no reversed flow at the 100mm plane, whilst one large region of reversed flow is predicted by the CFD at this station. The final point of note is that the measured reversed flow was contained within the projected wheel profile, whilst the predicted lower region extended outside the profile for all the transverse planes. The peak values do not appear to coincide with the lower vortical structures and their existence is as yet unexplained. Similar regions, occurring outside the projected wheel profile, have been measured in a subsequent test using a different wheel profile.

Drag Force – The mean drag force calculated from the experimental data was non-dimensionalised by the frontal area of the wheel. The drag coefficient (C_D) predicted by the CFD simulation was 0.638, which was 6.2% lower than the measured value of 0.680.

Care should be exercised when using force data as the sole accuracy measure [9] but the good experimental velocity correlation supports the validity of this prediction. This is further re-enforced by inspection of the circumferential static pressure coefficient (C_p) on the centreline of the tyre surface, Figure 5. Angular sign convention is also shown in this figure. Although surface C_p was not measured experimentally, comparison can be made with the work of Hinson [10]. This presented the pressure coefficients on the surface of a Formula One wheel, measured using transducers mounted within. Comparison was made with results taken from tests at the same Reynolds number as, and using a geometrically similar wheel to, this investigation. The results show good correlation and illustrate several important features. CFD predicted the separation 22° late at 244° as opposed to 266° measured by Hinson. Also, the base pressure was under-predicted just downstream of separation. Both factors would lead to an under-prediction of drag coefficient and are believed to be responsible, along with experimental errors, for the discrepancy seen in this study.

The predicted lift coefficient was 0.369 and is assumed to be over-predicted with the same causes as the drag under-prediction.

Support Sting Effects – Figure 6 shows velocity vector plots from the CFD investigations with and without the support sting. The model used throughout the study enabled the sting to be removed without modification to the mesh. The solver settings could ideally remain constant, thus improving comparison. However, it was not possible to convergence the ‘no-sting’ model using the solver settings detailed in the simulation procedure section. Convergence was reached by using a second-order accurate

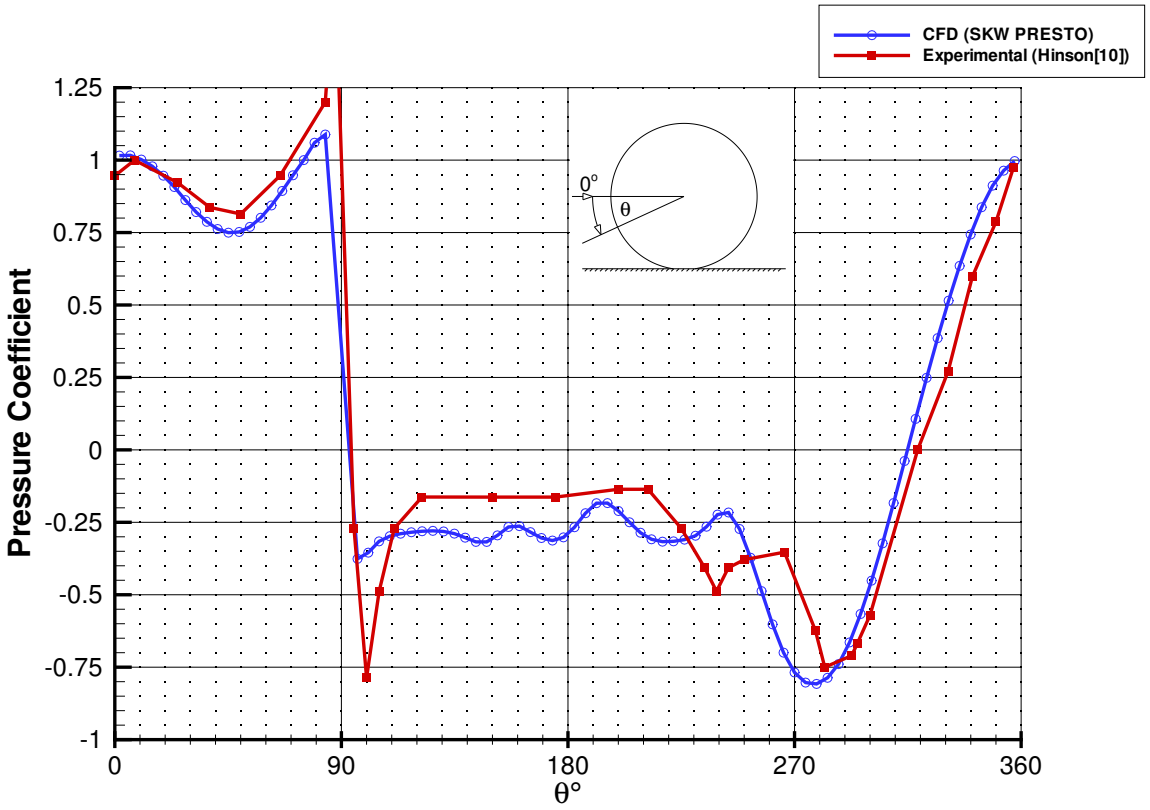

Figure 5: Circumferential Pressure Distribution on the Tyre Centreline

pressure-interpolation scheme as opposed to PRESTO! To allow direct comparison all the results presented in Figure 6 were calculated using second-order accurate differencing schemes for all terms. Therefore, the sting-present results differ slightly from those analysed in previous sections but exhibit all the main points previously highlighted.

The main difference (seen in the 10mm and 25mm planes) is the presence of a contra-rotating upper vortex pair in the no-sting results, as opposed to the single structure noted previously. This would suggest that the presence of the sting suppresses the formation of the upper left vortex. The upper structures appear to breakdown quicker when the sting is not present and are absent in the 100mm plane.

With regard to the jetting vortices, the left structure is the larger of the two and is located closer to the wheel centreline. This is in direct contrast to the results noted in the presence of the sting.

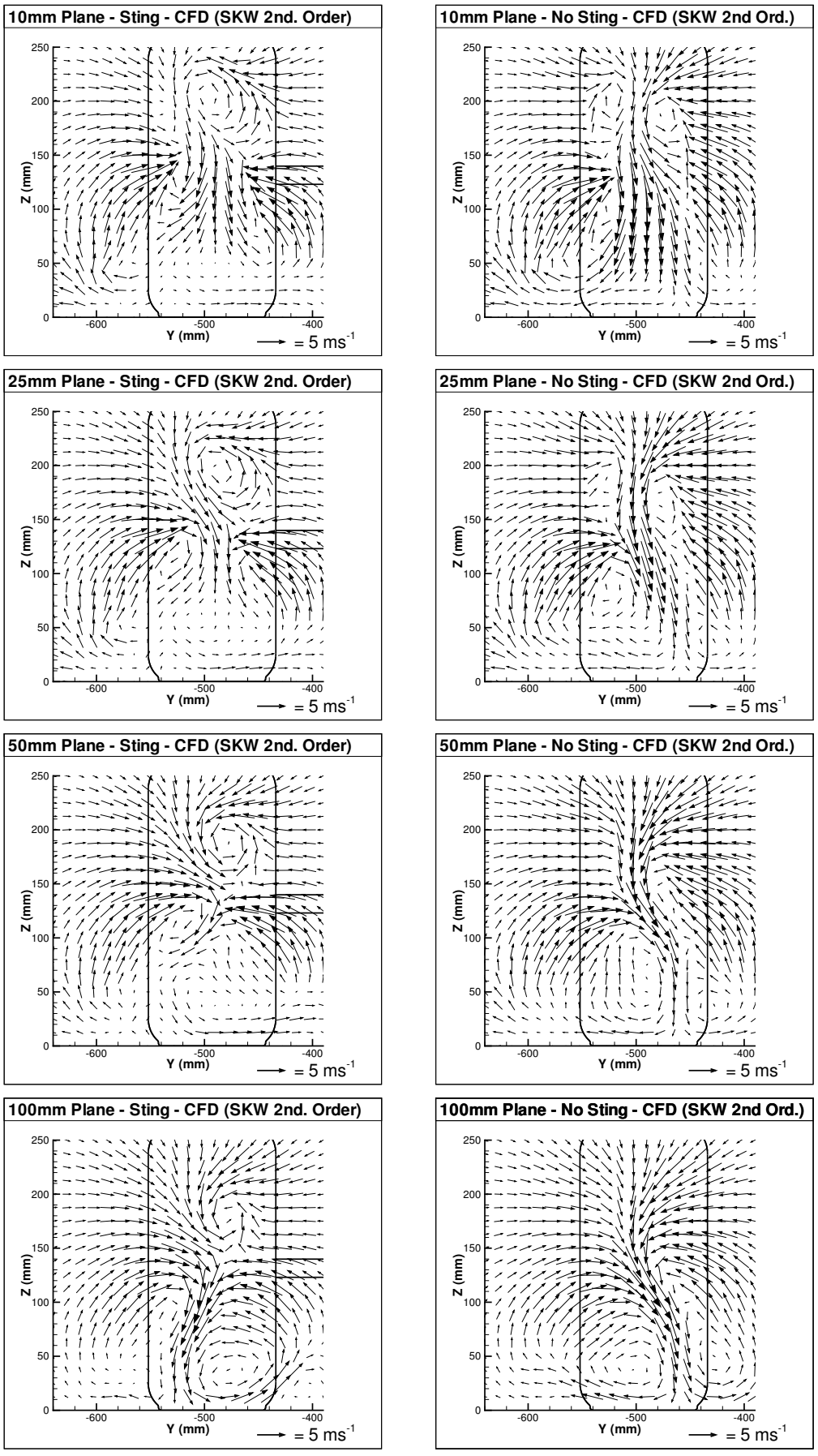

Figure 6: In-Plane Velocity Vectors (Sting - No Sting CFD Comparison)

Inspection of the remaining data showed that removal of the support sting resulted in:

- A wheel drag reduction of 2%;
- An increase in wheel lift of 16%;
- A reduction in mass flow-rate through the wheel of 83%;
- A delay of separation by 4°, on the wheel centreline.

The slight drag reduction appears to correlate with the later separation, whilst the additional upper vortex agrees with the increase in lift. Flow through the wheel is from right to left, therefore the results suggest that the sting forces more flow to pass through the wheel than would otherwise occur.

Conclusions – A computational fluid dynamic model of an isolated wheel rotating in ground contact, has been validated using data collected in a parallel experimental investigation. The following points were noted during validation:

- Strong prediction of the position, size, rotational sense and convection of the vortical structures present in the near wake of the wheel;
- Strong prediction of U velocity profile and deficit, including wake asymmetry and the presence of reversed flow;
- Under-prediction of wheel drag coefficient by 6% of the measured value;
- Flow separation from the centreline of the tyre appears to have been delayed by 22°;
- Slight over-prediction of V and W velocity components;
- Poor prediction of the location of areas of reversed flow and their convection downstream.

The validated model was subsequently used to predict the interference effect of the wheel support sting. This section of the study found that removal of the sting corresponded to:

- A reduction in wheel drag coefficient of 2%;
- An increase in wheel lift coefficient of 16%;
- Separation from the wheel centreline occurring 4° later.

Further evaluation suggests that the presence of the sting suppresses the formation of the upper trailing vortex on the opposite side of the wheel. It also appears to result in a considerable increase (in the region of five times) in mass flow-rate through the wheel.

Future Work – The exact mechanisms and origins behind the flow phenomena observed in this study will be investigated. Of interest are the vortical structures in the near wake and the regions of reversed flow. A study of the unsteady nature of the wake of the wheel, using instantaneous velocity measurement techniques such as PIV, and time-accurate CFD simulation will also be carried out. The effect of geometry, both of the wheel and sting, on the conclusions made here will be studied.

Acknowledgements – The first named author wishes to acknowledge the Engineering and Physical Sciences Research Council (EPSRC) for their funding of this research through their CASE award scheme.

Contact – The Aeromechanical Systems Group of the Department of Aerospace, Power and Sensors, Cranfield University, RMCS Shrivenham can be contacted via:
http://www.rmcs.cranfield.ac.uk/daps/

Definitions, Abreviations & Acronyms

- CFD – Computational Fluid Dynamics
- LDA – Laser Doppler Anemometry
- PIV – Particle Image Velocimetry
- PRESTO! – PREssure STaggering Option
- RANS – Reynolds Averaged Navier-Stokes
- U Component – Aligned with freestream
- V Component – Horizontal, perpendicular to freestream
- W Component – Vertical, perpendicular to freestream

References

[1] J. E. Hackett, J. B. Baker, J. E. Williams, and S. B. Wallis. On the influence of ground movement and wheel rotation in tests on modern car shapes. Paper 870245, Society of Automotive Engineers, 1987.

[2] A. F. Skea, P. R. Bullen, and J. Qiao. The use of CFD to predict the air flow around a rotating wheel. In *2nd MIRA Int. Vehicle Aerodynamics Conf*, UK, 1998.

[3] B. Basara, D. Beader, and V. P. Przulj. Numerical simulation of the airflow around a rotating wheel. In *3rd MIRA Int. Vehicle Aerodynamics Conf*, UK, 2000.

[4] L. Axon, K. Garry, and J. Howell. An evaluation of CFD for modelling the flow around stationary and rotating isolated wheels. Paper 980032, Society of Automotive Engineers, 1998.

[5] Fackrell J. E. *The Aerodynamic Characteristics of an Isolated Wheel Rotating in Contact with the Ground*. PhD thesis, Imperial College of Science and Technology, London, 1972.

[6] Fackrell J. E. and J. K. Harvey. The flow field and pressure distribution of an isolated road wheel. In *Advances in Road Vehicle Aerodynamics*, Paper 10, pages 155–165. BHRA, London, 1973.

[7] R. G. Dominy. Aerodynamics of Grand Prix cars. *Proc. of the Institute of Mechanical Engineers, Part D - Journal of Automobile Engineering*, 206, 1992.

[8] E. Merker and H. Berneburg. On the simulation of road driving of a passenger car in a wind tunnel using a moving belt and rotating wheels. In *3rd Int. Conf. Innovation and Reliability*, Florence, April 1992.

[9] F. T. Makowski and S-E. Kim. Advances in external-aero simulation of ground vehicles using the steady RANS equations. In *Vehicle Aerodynamics SP-1524*, Paper 2000-01-0484. Society of Automotive Engineers, 2000.

[10] Hinson M. *Measurement of the Lift Produced by an Isolated, Rotating Formula One Wheel Using a New Pressure Measurement System*. MSc thesis, Cranfield University, 1999.

2002-01-3293

On the Near Wake of Rotating, 40%-Scale Champ Car Wheels

Robin Knowles, Alistair Saddington and Kevin Knowles
Aeromechanical Systems Group, Cranfield University, RMCS Shrivenham

ABSTRACT

This paper presents the results of an investigation of the near wake of isolated, cambered and un-cambered, 40%-scale, non-deformable Champ Car wheels rotating in ground contact. Three-dimensional velocity measurements were made in their near wakes using Laser Doppler Anemometry. Inspection of the derived velocity contours, vectors and vorticity contours, suggested that several of the theoretical vortical structures are suppressed by 'real' wheel geometry and the presence of a support sting. Drag force measurements were made, revealing the cambered wheel to have 12% higher drag coefficient than the un-cambered equivalent.

INTRODUCTION

Previous studies highlighting the importance of ground simulation in automotive aerodynamics have led to the widespread use of rolling road ground simulation, especially in the model-scale testing of racecars. Nowhere is ground motion and wheel rotation more important than in the development of single-seater racecars such as Champ Cars and Formula One. Ground effects dominate the aerodynamic characteristics of such cars and the presence of unfaired, open wheels makes effective simulation imperative.

Many wind tunnels involved in racecar development use a continuous-belt rolling road system for ground simulation. When coupled with an effective tunnel boundary layer control system, such as suction or tangential blowing, ground effects can be simulated with reasonable ease. The belt can also provide the driving force for wheel rotation if freely rotating wheels are rested upon it. The model car can then be held in position by an overhead or rear-mounted support sting that, if suitably instrumented, can be used to measure the forces acting on the model. In this configuration, however, these forces will also include the frictional forces due to mechanical contact between the wheels and the belt. In aerodynamic terms these forces are considerable and must be taken into consideration.

One of the most common ways of overcoming this problem, whilst retaining wheel rotation, is to test the model car in what is known as a 'wheels-off' configuration. Here the wheels are not supported by the suspension of the model, but by individual, externally-mounted stings. This arrangement mechanically de-couples the car body from the ground whilst still allowing the wheels to be rotated by direct contact with the rolling-road belt. Measurements of the aerodynamic forces exerted on the body no longer require correction to account for the mechanical contact between ground and wheels. Inclusion of further force balances in the wheel stings allows the effect of the body on the wheel drag to be determined.

It has proved difficult to accurately determine the lift of rotating wheels by force balance inclusion due to the varying nature of reaction forces at the contact patch. Several studies have been carried out in an attempt to develop a procedure to resolve wheel forces from surface pressure measurements made by transducers housed within the wheel [Fackrell (1972) and Hinson (1999)]. Other studies carried out on wheel flows were concerned with determining the effect of ground simulation and focused on surface pressure and force measurements [Morelli (1969), Stapleford and Carr (1969), Cogotti (1983)]. There is, however, a relative paucity of published research on the complex flow field surrounding rotating wheels.

To the best of the authors' knowledge there are only two published studies of the flowfield surrounding (as opposed to surface pressures on) wheels rotating in ground contact. Fackrell (1972) made measurements of total pressure at several transverse planes (orientated perpendicular to the main flow direction). The data were used to delineate the effective 'edge' of the wake at these stations by means of contours of 90% total pressure. Further work by Nigbur (1999) includes three-dimensional velocity and turbulence measurements made in similar planes using a hot-wire anemometer. Using measured surface pressures, bluff body knowledge and vortex theory the theoretical flow structure surrounding a wheel rotating in ground contact

was proposed by Cogotti (1983), amended by Merker and Berneburg (1992) and is illustrated in Figure 1.

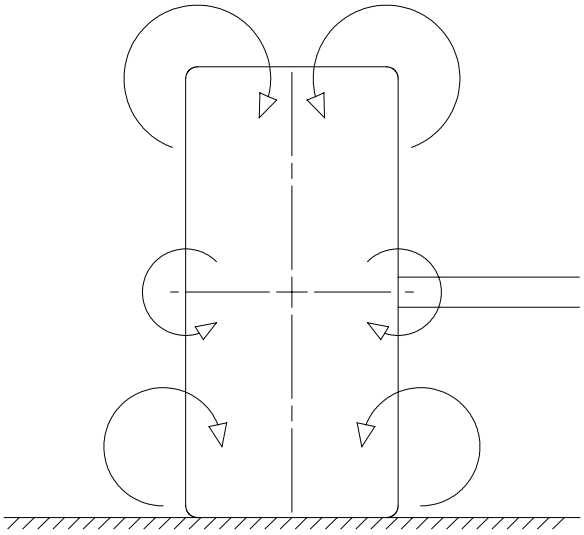

Figure 1: Proposed Wake Structure. After Merker and Berneburg (1992)

In motorsport terms, knowledge of these flow structures could lead to improvements in the performance of components in the immediate vicinity of the wheels, such as the increasingly complex front wing endplates of current formula one cars. It could also be applied to passenger and commercial vehicles, for example in improving the control of spray in wet conditions.

This paper presents the results of an experimental investigation into the structure of the near-wake (within half a wheel diameter downstream of the 'trailing edge') of an isolated racecar wheel rotating in ground contact. Three-dimensional velocity measurements were made in four transverse planes using Laser Doppler Anemometry (LDA). In addition wheel drag forces were also recorded. Further, the effect of wheel geometry on this region will be presented.

TEST EQUIPMENT AND PROCEDURE

WHEEL MODELS - Reynard Motorsport supplied all models used in this study and as such they represent the technology and level of detail currently employed in racecar aerodynamic development.

One of the main features of interest in wind tunnel wheel modelling is the use of non-deformable tyres. With the exception of the new steel-belt and multi-belt systems, the majority of rolling roads do not allow the use of a pneumatic tyre that can be deformed to the correct shape by the application of a load through its support strut. The frictional loads induced by such force application dramatically shorten belt life and can result in severe wind tunnel damage should the tyre fail. To this end non-deformable wheels are commonplace in automotive aerodynamic development. However, as Fackrell (1972) showed, the flow surrounding a wheel is extremely sensitive to tyre profile, especially shoulder profile. A deformed tyre is not axisymmetric about its rotational axis. Therefore, any cross-section rotated about this axis to generate a non-deformable tyre profile will be inaccurate over some of its circumference. An approximation to the deformed tyre profile must, therefore, be used.

A further complication arises when racecar configurations include cambered wheels. Here the suspension geometry is altered such that the axis of wheel rotation is at an angle above the horizontal (top of the wheel leans towards the car when viewed from in front). Taking an approximate profile of such a tyre and sweeping it about its rotational axis produces a tyre that is not only inaccurate over some of its circumference but is also conic. The use of a non-deformable wheel with an approximate tyre profile is clearly not a faithful representation of the real situation but is unavoidable with current testing techniques.

Two 40%-scale (263mm diameter) non-deformable tyre and hub assemblies (one with 4° camber) were investigated in this study. The tyre part of the assembly was manufactured from carbon fibre with a smooth, lacquered surface finish. The actual tyre profiles of both cambered and parallel (0° camber) wheels can be seen in Figure 2. The machined aluminium wheel hubs were exact scale models of the BBS multi-spoke alloy hubs used on Reynard Champ Cars. The hubs were identical for both wheels and each featured an integrated, radially-vented brake disc and mounting bell. Rotation was permitted by free-running bearings housed within the hub.

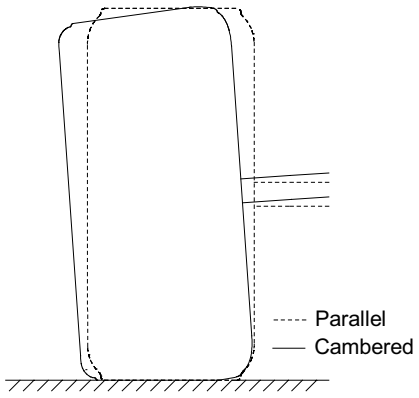

Figure 2: Comparison of Parallel & Cambered Profiles

The wheels were held in position by one of the support stings used in model car testing. The sting was essentially an aluminium beam of symmetrical aerofoil section that ran in line with the rotation axis from the outboard side of the wheel to a mounting pylon beside the rolling road (Figure 3). The sting comprised two

parts, the balance mount (nearest the wheel and approximately ¼ of the total length), and the main support (the remaining ¾). The joint between these two parts was hinged, such that the balance mount remained co-linear with the rotation axis of whichever wheel was tested. The reaction force between the belt and wheel was that due to the weight of the components. The sting applied no additional force to the wheel and no problems were encountered with wheel lift during testing.

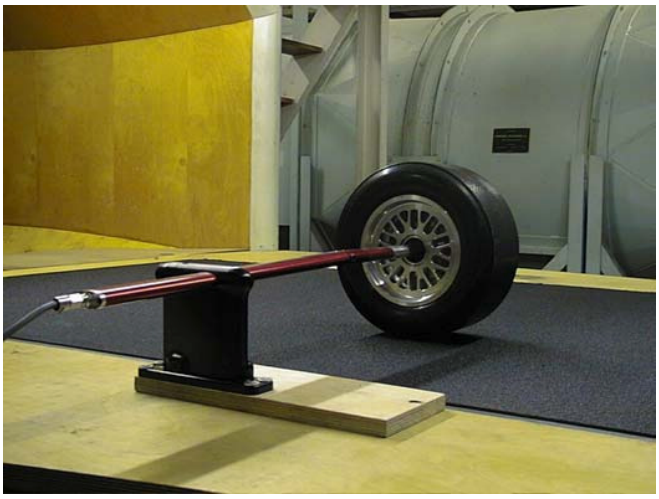

Figure 3: Experimental Set-up showing Parallel Wheel and Support Sting

The drag force was resolved by directly attaching the wheel to a 50N load cell, which was in turn supported by the balance mount. The load cell was shrouded by carbon fibre thus maintaining the sting aerofoil profile to the wheel face. The cabling for the load cell was recessed into the surface of the sting and was not in contact with the freestream air.

TUNNEL & ROAD - Testing was carried out in the Shrivenham 1.52m by 1.14m closed-return open-jet wind tunnel. The wind speed was consistent throughout the tests at 20 ms^{-1}. Ground simulation was by continuous-belt rolling road, manually synchronised with the tunnel freestream velocity using an optical tachometer. The tunnel boundary layer was removed upstream of the rolling road by suction through two porous plates. The division of suction between these two plates could be altered to improve the boundary layer profile. Transition from the suction boxes to the rolling road was via a knife-edge. Re-commissioning of the tunnel one month prior to testing showed that in the configuration used in this study, the boundary layer at the wheel location reaches 99% of freestream dynamic pressure at 5.7mm from the belt surface.

LDA SET-UP - The three-dimensional LDA measurements were taken using a Dantec system based on FibreFlow optics with two 1000mm focal length probes rigidly mounted to a three-component traverse. Data collection was carried out by three BSA enhanced signal processors, with all equipment controlled using Dantec Burstware software.

The gantry for the tunnel's overhead balance limited access to the test section, and therefore, the probes could not be arranged to directly measure V and W components of velocity. Great care was taken to optimise the set-up so that the available measurement area was maximised whilst maintaining as large an angle as possible between the probes. U velocity was measured directly, whilst V and W were resolved from the remaining two measured components and the angles of the probes to the horizontal. The system was set-up such that the probes remained outside the tunnel jet thus maximising the non-intrusive nature of the technique. Seeding of the wind tunnel flow was by a JEM Hydrosonic fog generator using JEM Hydrosonic fluid, which ran continuously throughout each test. To maximise the seeding density the generator was placed inside the tunnel, upstream of the test section, turbulence screens and one set of cascades.

TEST PROCEDURE - As stated, all testing was carried out at 20ms^{-1} yielding a Reynolds number (based on wheel diameter) of the order of 3.69×10^5 for both wheels. Three-dimensional LDA measurements were made in transverse planes perpendicular to the main flow direction whilst the wheel was rotating in ground contact. Due to the access constraints previously mentioned, each plane was restricted to a 250mm square with the wheel placed at the approximate longitudinal centreline of the planes and 410mm downstream of the knife-edge.

The planes were located at 10, 25, 50 and 100 mm downstream of the 'trailing edge' of the wheel. All planes were identical, containing 441 equally spaced data points. All points were sampled for 15 seconds to allow collection of 2500 samples for each component. These data were subsequently used to yield mean velocity and rms values.

Each plane of measurement took 2 hours. Testing was paused after completion of a plane to avoid overheating the rolling road bearings and to replenish the seeding fluid. It is worthy of note that the tunnel air temperature did not rise by more than 3°C over any test. The LDA tests took place over two days with one wheel tested per day.

Force data were collected for the wheel rotating at 20ms^{-1} with and without wind to allow correction for frictional contact forces. Again, this was carried out for both wheels and the corrected forces were non-dimensionalised by the relevant frontal area. The measured forces were repeatable to within 0.5%.

RESULTS & ANALYSIS

PARALLEL WHEEL VS. VORTEX THEORY - Inspection of the velocity vectors (Figure 4) and vorticity contours (Figure 5) for the parallel wheel show that the structure of its near wake broadly resembles that predicted by

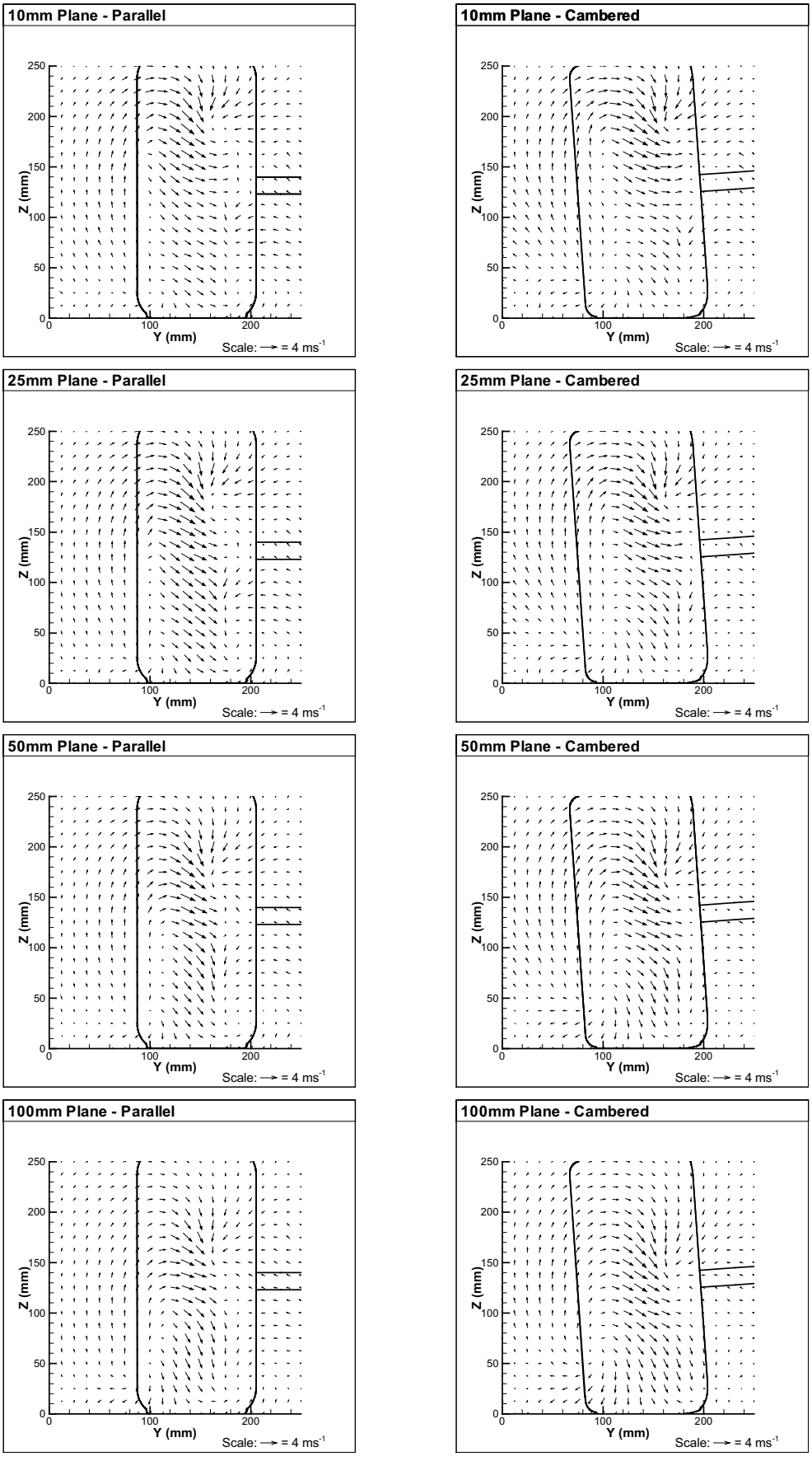

Figure 4: In-Plane Velocity Vectors

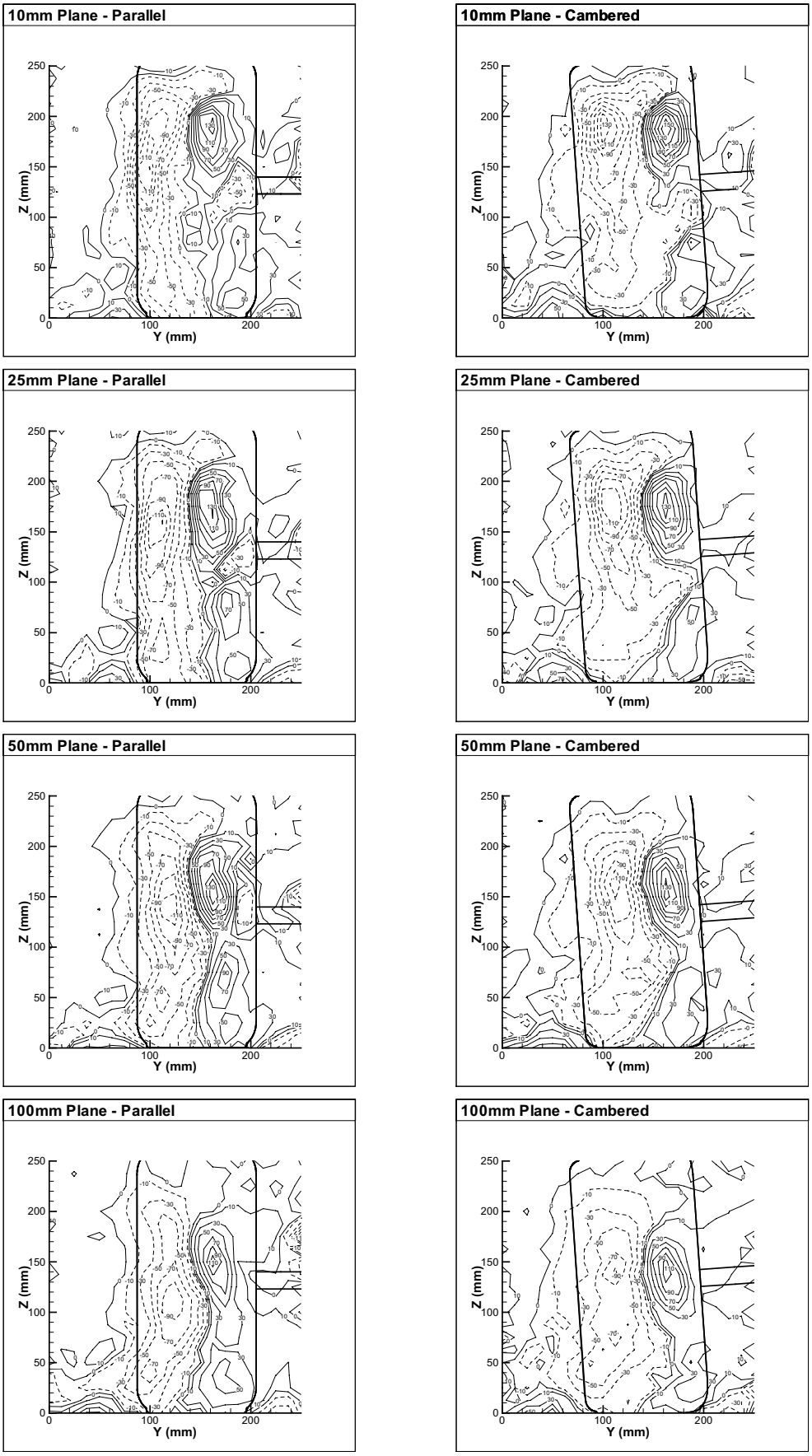

Figure 5: Contours of Vorticity about the Streamwise Axis (s^{-1}), (negative values indicated by dashed lines).

vortex theory (Figure 1). From here on, the three pairs of vortices from this theory will be referred to, from top to bottom, as the upper vortex, hub vortex and jetting vortex. One of each occurs on the left and right sides of the wheel and in this study positive vorticity indicates anticlockwise rotation. References to left and right are with respect to the plots, where the car would be to the left and wheel sting to the right. The upper vortex is a conventional trailing vortex associated with lifting bodies. The hub vortex appears to be formed by flow leaving the hub with rotation along the wheel axis and being turned by the main flow to a streamwise orientation. The term "jetting vortex" was used by Merker and Berneburg (1992) to refer to a trailing vortex originating from the strong viscous actions in front of the tyre contact patch.

Inspection of the vorticity contours (Figure 5) shows that of the six predicted vortices, at least the left hub vortex appears to be absent. However the velocity vector plot (Figure 4) shows that only the right upper vortex and both jetting vortices are present. The rotation of the vortices is consistent with those produced by a lifting body and are as expected.

The observed discrepancy between prediction and experiment could be due to differences in the geometry considered. Theory is based on the flow around a low aspect ratio, circular cylinder, whilst the experiment includes factors such as rotating cavities, through-flow and support sting interference.

It appears that it is interference from the sting combined with right-to-left flow through the wheel that suppresses the right hub vortex. The region of negative vorticity shown in this position is probably not due to hub rotation but driven by the right upper and jetting vortices.

Although the vorticity plot shows a large region of negative vorticity on the left side of the wheel, inspection of the velocity vector plots reveals a weak vortex structure with a large core radius. This seems to be the area in which the experimental results deviate most from theory.

As the wheel is a lifting body, one would expect a net downwash in its near wake. However the flow entrained from inside the wheel hub, essentially a deep rotating cavity in cross-flow, will have a positive vertical velocity due to the upward motion of the rear of the wheel. This region of upward flow is immediately subjected to the downwash resulting in the band of high vorticity. The rapid change of direction suppresses the formation of the left upper vortex and flow is entrained into the developed right upper vortex, further strengthening it.

It was presumed that the jetting vortices would be strongest [Morelli, (2000)] but this has not been observed in this study. These vortices are approximately half the peak vorticity and both lie within the projected wheel profile.

PROGRESSION DOWNSTREAM

@10mm - The flow is as described above with a fairly symmetrical structure. The region of negative vorticity extends almost the height of the wheel and a large region of reversed flow exists in the lower half of the projected wheel profile (Figure 6).

@25mm - The location of the upper vorticity peaks has dropped by approximately 20mm. The right jetting vortex has risen slightly and intensified, entraining flow from the upper left region and increasing the vorticity of the left jetting vortex. The region of reversed flow has reduced, with a peak occurring at the lower left shoulder of the projected wheel profile.

@50mm - The location of the upper vorticity peaks has dropped a further 25mm with the left region moving closer to the right region. The upper left region of high vorticity is beginning to form a more distinct vortex although flow is still being heavily entrained into the other three established vortices. The intensification and motion of the jetting vortices seen over the first 25mm continues here although the right jetting vortex is now stronger than that on the left. Reversed flow only remains in a small area at the lower left shoulder of the projected wheel profile.

@100mm - The upper left structure has continued to move down and to the right increasing the asymmetry of the vortices. The right jetting vortex has greatly reduced in intensity and is now weaker than the left jetting vortex, reversing the situation at the previous station. Also, the region of negative vorticity corresponding to the right hub vortex has been lost. The two regions of high vorticity on the left side of the wheel appear to be coalescing to form a single vortical structure of negative sense. The peak vorticity still occurs in the upper structures and not in the jetting vortices as presumed. No regions of reversed flow persist at this station.

CAMBERED VS. PARALLEL WHEELS - The structure of the near wake of the cambered wheel and its propagation downstream is broadly similar to that of the parallel wheel with some notable differences.

@10mm - Both upper vortices are higher intensity, tighter and better defined than those of the parallel wheel. The jetting vortices are however of slightly lower vorticity than seen with the parallel wheel. The net effect of this is significantly lower entrainment into the jetting vortices from the upper structures. The region of reversed flow is of similar magnitude to that of the parallel wheel but more extensive. The region is again skewed towards the lower left shoulder of the projected profile but now extends outside this area (Figure 6).

@25mm - The decrease in vorticity and reduction in height of the upper vortex structures noted in the parallel wheel at this station are also present here. Similarly, the increase in vorticity of the right jetting vortex and the associated increased entrainment is observed.

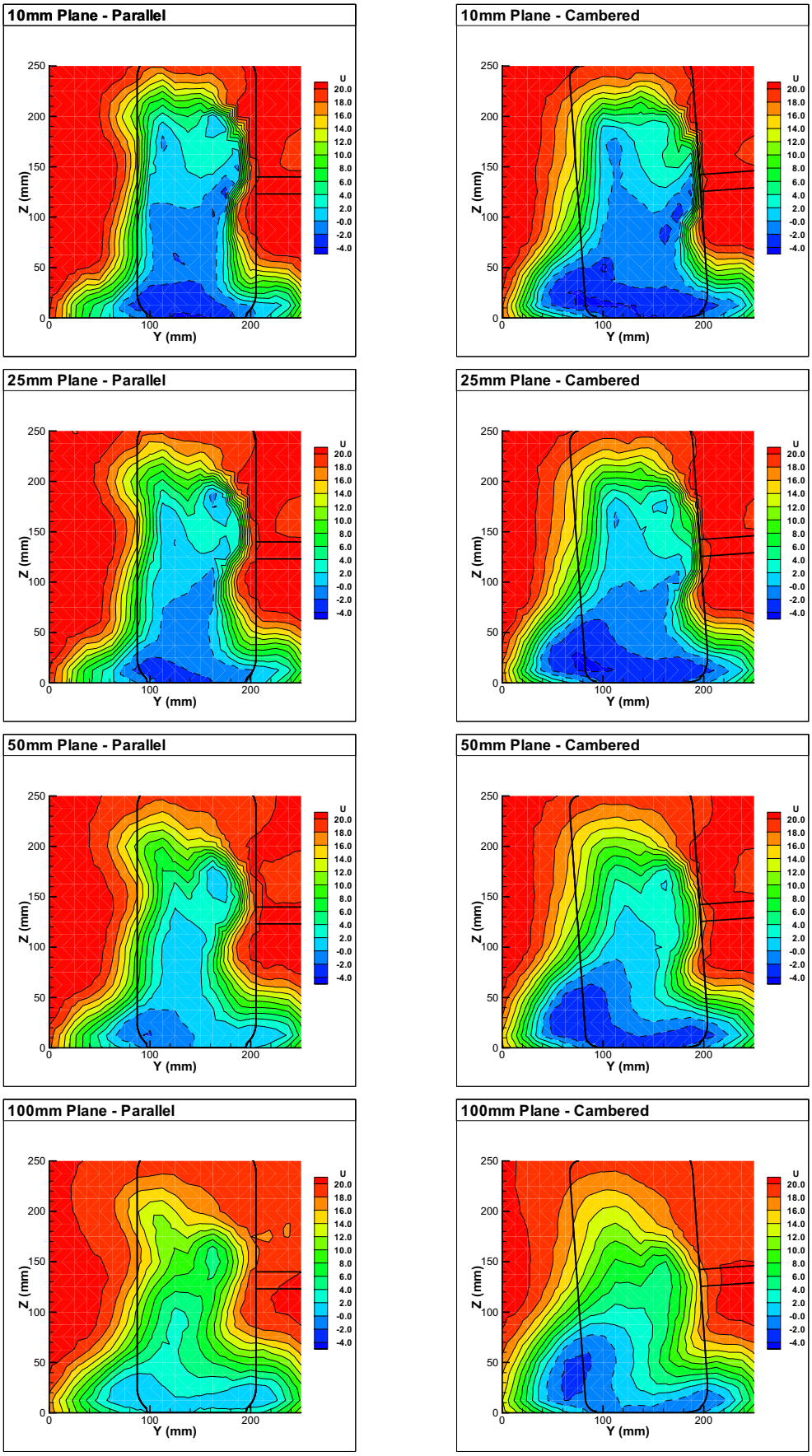

Figure 6: Contours of U Velocity (ms^{-1}) – (negative values indicated by dashed lines).

The region of reversed flow is reduced in size but is now stronger and larger than seen with the parallel wheel, remaining heavily skewed outside the lower left shoulder.

@50mm - The upper vortical structures have dropped further with little change in peak vorticity. The indication that the left structures are beginning to coalesce is present here whereas this does not occur until 100mm downstream of the parallel wheel. Reversed flow is still skewed outside the lower left shoulder of the wheel with the region extending across the whole width of the projected wheel. The region at the lower right shoulder does not extend much beyond the projected profile.

@100mm - The vorticity of the left jetting and upper vortices is tending towards equalisation and the structures are coalescing further. The equivalent right vortices do not appear to be coalescing, but are decreasing in magnitude. The initial influence of the suppressed hub vortex could be responsible for delaying the joining of these two structures. No reversed flow was present at this distance downstream of the parallel wheel. The wake of the cambered wheel does, however, still exhibit negative U velocities in the regions previously noted.

The existence of regions of reversed flow in the wake of both wheels was not unexpected. Such regions are one of the features associated with bluff body wakes. Neither was it totally unexpected that the wake would be asymmetric. The presence of a wheel support sting, a real wheel hub and the associated flow through the wheel make the assembly highly asymmetric. However it was not expected that these two factors would be as closely linked as they appear to be, illustrated by the contour plots of U velocity (Figure 6). The data collected for both wheels shows a bias of the lower part of the wake towards the left side of the wheel. This is also the region in which the highest values of reversed flow are noted. Initially this was thought to be due to misalignment (yaw) of the wheels in the test section, but subsequently found not to be the case. This was re-enforced when similar structures were noted in a CFD simulation of the experimental set-up, Knowles et al (2002) and in the mean U velocity plots of Nigbur (1999). No regions of reversed flow were noted by Nigbur (1999) as data were collected using a hot-wire anemometer, which was insensitive to U velocity direction.

The wake survey carried out by Fackrell (1973) yields little other than a similar overall shape. However, an indication of asymmetry is given by the statement that "only the half of the flow field opposite to the supporting rods is shown as their wakes would only confuse the picture."

It was not possible to determine the cause of the regions of reversed flow from the data collected nor why the effect is more pronounced for the cambered wheel. The reversed flow region and the mechanisms behind it are of interest in motorsport terms as it is inboard of the wheel and may impact upon the flow into, around and under the sidepods.

All of the flow structures noted in this study could be further understood by examining their unsteady nature using a planar, instantaneous velocity measurement technique such as particle image velocimetry (PIV). It is possible that the region of reversed flow is a time-averaged representation of a highly unsteady flow feature such as turbulent vortex shedding.

FORCES - The higher vorticity and higher velocity deficit noted in the cambered wheel results would suggest that this wheel has higher drag. This is confirmed by the force measurement experiments, the results of which are presented in the Table 1. Coefficients are based on the respective projected areas.

Table 1: Wheel Drag Forces and Coefficients

Wheel	Area (m^2)	Drag (N)	Drag Coefficient
Parallel	0.0306	5.08	0.68
Cambered	0.0313	5.81	0.76

CONCLUSIONS

The results of this study suggest that the vortex structure surrounding an isolated wheel rotating in ground contact differs from the theoretical proposal in that:

1. The vortex shed from the hub, on the side of the support strut, is suppressed;
2. The vortices shed from the hub on the opposite side to the support strut, and from the upper tyre shoulder of that side are suppressed by entrainment of flow from inside the wheel hub;
3. The jetting vortices emanating from in front of the tyre contact patch have lower vorticity than those from the upper tyre shoulders.

The above points apply to both the parallel and cambered wheels. However the results of the cambered wheels generally showed more defined, higher intensity vortex structures. Correspondingly, the cambered wheel was found to have approximately a 12% higher drag coefficient than a parallel wheel, based on respective frontal areas. The vortices persisted to 100mm downstream of the wheel. By this downstream station, however, the vortical structures on the side opposite to the support sting were beginning to coalesce.

A region of reversed flow was noted at every measurement station except 100mm downstream of the parallel wheel. In every case this area was concentrated, or skewed towards, the lower left shoulder of the projected wheel profile. The region was more pronounced in the cambered wheel results and extended

outside the projected area of the wheel into the freestream. The cause of the reversed flow could not be determined from the experimental data but also appears to be present in other published research. Further work using alternative, instantaneous velocity measurement techniques will be required to resolve the causes of this interesting flow feature.

ACKNOWLEDGMENTS

The first named author wishes to acknowledge the Engineering and Physical Sciences Research Council (EPSRC) for their funding of this project through a CASE award scheme.

CONTACT

The Aeromechanical Systems Group of the Department of Aerospace, Power and Sensors, Cranfield University, RMCS can be contacted via:
http://www.rmcs.cranfield.ac.uk/departments/daps/

DEFINITIONS, ACRONYMS, ABBREVIATIONS

CFD: Computational Fluid Dynamics

LDA: Laser Doppler Anemometry

PIV: Particle Image Velocimetry

U Velocity Component: Aligned with freestream

V Velocity Component: Horizontal, perpendicular to freestream

W Velocity Component: Vertical, perpendicular to freestream

REFERENCES

1. Cogotti, A. (1982). *Aerodynamic Characteristics of Car Wheels.* Intl J. of Vehicle Design, Technological Advances in Vehicle Design Series, SP3, Impact of Aerodynamics on Vehicle Design, pp. 173-196
2. Fackrell, J. E. (1972). *The Aerodynamic Characteristics of an Isolated Wheel Rotating in Contact with the Ground.* PhD Thesis, Imperial College, London, UK.
3. Fackrell, J. E. and Harvey, J. K. (1973). *The Flow Field and Pressure Distribution of an Isolated Road Wheel. Advances in Road Vehicle Aerodynamics*, Paper 10, pp. 155-165, BHRA.
4. Hinson, M. (1999). *Measurement of the Lift Produced by an Isolated, Rotating Formula One Wheel Using a New Pressure Measurement System.* MSc Thesis, Cranfield University, UK.
5. Knowles, R. D., Saddington, A. J., Knowles, K. (2002). *Simulation and Experiments on an Isolated Racecar Wheel Rotating in Ground Contact.* 4th MIRA Intl. Vehicle Aerodynamics Conference, Gaydon, UK.
6. Merker, E., Berneburg, H., (1992). *On the Simulation of Road Driving of a Passenger Car in a Wind Tunnel Using a Moving Belt and Rotating Wheels.* 3rd Int. Conf. Innovation and Reliability, Florence, April 8-10.
7. Morelli, A. (1969). *Aerodynamic Actions on an Automobile Wheel.* Proc. of the 1st Symp. On Road Vehicle Aerodynamics, The City University, London, UK.
8. Morelli, A. (2000) *A New Approach to Advanced Automobile Basic Shapes*. Vehicle Aerodynamics, SAE SP-1524, ISBN 0-7680-0574-4, pp173-182.
9. Nigbur, J. E. (1999). *Characteristics of the Wake Downstream of an Isolated Automotive Wheel.* MSc Thesis, Cranfield University, UK.
10. Stapleford, W. R. and Carr, G. W.(1969) *Aerodynamic Characteristics of Exposed Rotating Wheels.* Report 1970/2, MIRA, Nuneaton, UK.